

Quantitative MR Imaging: Applications to Chronic Liver Disease and Hepatocellular Carcinoma

by

Eric M. Bultman

A dissertation submitted in partial fulfillment of the requirements for the degree of

Doctor of Philosophy
(Biomedical Engineering)

at the

UNIVERSITY OF WISCONSIN – MADISON

2012

Date of final oral examination: 10/10/12

This dissertation is approved by the following members of the Final Oral Committee:

Walter F. Block, Associate Professor, Biomedical Engineering
Scott B. Reeder, Associate Professor, Biomedical Engineering
Oliver Wieben, Assistant Professor, Medical Physics
Adnan X. Said, Associate Professor, Medicine (Hepatology)
Robert Blank, Associate Professor, Medicine (Endocrinology)

Abstract

Chronic liver disease (CLD), cirrhosis and hepatocellular carcinoma (HCC) remain major health problems in the US and other developed countries. Currently, CLD is diagnosed using a variety of qualitative methods, ranging from physical exam to MR and CT imaging. However, accurate staging of CLD requires liver biopsy, which is expensive, invasive and imposes significant risk of complications such as infection and bleeding. Meanwhile, treatment of HCC – a serious complication of CLD – is often performed through arterial chemoembolization, in which an intravascular catheter is advanced near the tumor and chemoembolic therapy is administered. Upon completion of therapy, patients undergo several follow-up CTs to verify treatment localization and efficacy. Although chemoembolization can be curative for small HCCs, patients are exposed to considerable amounts of ionizing radiation during treatment and follow-up, which increases risk for future tumor development – especially in the background of a cirrhotic liver.

In this dissertation, the use of dynamic contrast-enhanced MRI combined with quantitative perfusion modeling for detection of CLD and assessment of disease severity is investigated. A robust means of hepatic motion compensation (sequential breath holds) is utilized, and a method for fitting a quantitative perfusion model using only motion-compensated data is developed. This method is applied to DCE-MR data from a cohort of 12 volunteers and 10 patients with HCC; differences in perfusion parameters between normal liver, diseased liver and tumor are investigated.

The potential application of fat-water MRI for detection of chemoembolization treatment region and quantification of treatment dose is also investigated. In a small cohort of patients, the feasibility of using IDEAL MRI in place of CT for post-embolization detection of ethiodol distribution is explored. The feasibility of using IDEAL to image ethiodol immediately after intrahepatic injection is also studied in a porcine model.

Finally, because hepatorenal syndrome is often associated with CLD – and may necessitate both liver and kidney transplantation – the use of non-contrast MR angiography to image the transplant renal vessels is studied. Two MRA methods based on Cartesian and radial pulse sequences are compared in a pilot study of 21 renal transplant patients; performance is assessed according to four image quality criteria.

Acknowledgements

I would first like to acknowledge one of my co-workers, Ethan Brodsky, for his assistance in performing perfusion MR exams of liver patients and his help with post-processing the data. It would have been a pain to figure out how to do all of this on my own!

I'd like to acknowledge Sam Hurley for some helpful discussions regarding T_1 mapping in the abdomen, as well as his assistance in performing an experiment to determine the contrast sensitivity of the RT-VIPR sequence.

I'd also like to acknowledge Kevin Johnson for his work on the iterative SENSE-based reconstruction used for the liver perfusion data; as well as Deb Horng for her help with implementing a mutual information registration method for the perfusion data.

Finally, I'd like to acknowledge Sara John, Jan Yakey and Kelli Hellenbrand for their assistance with liver patient recruitment and scanning. Thanks for all the help getting patients set up at the scanner (also for the phone call when I'd completely spaced and forgotten to show up at one of the exams)!

Of course, none of this work would have been possible without the guidance of my advisors, Scott Reeder and Wally Block. Thanks for all the helpful discussions and scientific advice you've provided me over the years, guys!

Table of Contents

1. Background.....	1
1.1 Natural History and Etiology of Chronic Liver Disease	1
1.2 Chronic Liver Disease: Renal Effects	4
1.3 Natural History and Diagnosis of HCC	5
1.4 Treatment of HCC	6
1.5 Role of MR Imaging in CLD.....	10
2. Detection of Ethiodized Oil after TACE Treatment with IDEAL Imaging	14
2.1 Background: Visualization of TACE Treatment Region using MRI	14
2.2 MR Imaging of Ethiodol Distribution at TACE Follow-Up.....	17
2.2.1 Methods.....	17
2.2.3 Results.....	19
2.2.4 Conclusions	22
2.3 <i>In vivo</i> injection of ethiodol into liver of swine model	23
2.3.1 Background	23
2.3.2 Methods.....	24
2.3.3 Results.....	26
2.3.4 Conclusions	26
2.4 Future Work.....	28
3. Visualization of renal transplant vessels using VIPR-SSFP and Cartesian SSFP (IFIR).....	29
3.1 Background	29
3.2 Methods.....	32
3.3 Results	36
3.4 Discussion and Conclusions.....	40

4. Dynamic Contrast-Enhanced MRI and Quantitative Perfusion Modeling in the Liver	45
4.1 Background I: Imaging-based measurement of tissue perfusion	45
4.1.1 Measurement of blood flow to the liver	45
4.1.2 Hepatic flow measurement using Doppler ultrasound	46
4.1.3 Hepatic perfusion measurement using contrast-enhanced CT	47
4.1.4 Quantitative versus semiquantitative perfusion parameters	48
4.2 Background II: Pharmacokinetic modeling of hepatic contrast enhancement using indicator-dilution theory	49
4.2.1 The dual-input single-compartment model	49
4.2.2 Determination of the tissue residue function	56
4.3 Background III: Hepatic perfusion measurement using contrast-enhanced MR imaging	59
4.3.1 Quantitative perfusion modeling using DCE-MRI: Challenges ...	59
4.3.2 Semiquantitative perfusion modeling using DCE-MRI	64
4.3.3 Modern MR methods for measuring hepatic perfusion	65
4.4 Quantitative and semiquantitative perfusion MRI in healthy volunteers and HCC patients	66
4.4.1 Background	66
4.4.2 Methods	69
4.4.3 Results	78
4.4.4 Discussion and Conclusions	84

5. Summary and Future Work.....	102
5.1 Summary	102
5.2 Future Work.....	104
References.....	108

Summary of Work

MRI has become an essential component of the medical evaluation of chronic liver disease (CLD) and cirrhosis. Dynamic contrast-enhanced MRI is used to clinically diagnose focal liver lesions; its high sensitivity and specificity for detection of these lesions have caused it to supplant the use of DCE-CT in many centers. MRI also holds the potential to improve liver-directed therapies for hepatocellular carcinoma, such as chemoembolization, by allowing real-time visualization of catheter placement and localization of treatment distribution without exposing patients to ionizing radiation. Finally, MRI has significant utility in the clinical evaluation of patients with CLD-associated hepatorenal syndrome, as it enables non-contrast angiographic imaging of the native and transplant renal vessels.

Chapter 1 (*Background*) provides an introduction to the natural history and etiology of chronic liver disease. CLD is becoming increasingly common in the US due to the obesity epidemic, as fatty liver disease has been associated with non-alcoholic steatohepatitis. Several other causes of CLD, such as alcoholism and viral hepatitis, also result in considerable disease burden. This chapter also reviews the natural history and etiology of hepatocellular carcinoma (HCC), a common complication of CLD and cirrhosis. Several methods for treating focal HCC lesions are reviewed.

Chapter 2 (*Detection of Ethiodized Oil after TACE Treatment with IDEAL Imaging*) discusses the application of chemical shift-based fat-water MRI for detection of

treatment region and quantification of treatment amount after completion of TACE therapy. Currently, patients who undergo TACE receive several follow-up CT scans after the procedure to track treatment distribution as well as possible tumor re-growth. In this chapter, the potential of replacing follow-up CTs with IDEAL MRI is investigated both in a porcine model as well as a population of TACE-treated patients.

Chapter 3 (*Visualization of renal transplant vessels using VIPR-SSFP and Cartesian SSFP*) compares the efficacy of Cartesian and radial-based non-contrast MR angiographic methods in depicting the arterial and venous vessels of the transplanted kidney. Hepatorenal syndrome is highly associated with CLD, and many patients who suffer from this poorly-understood condition must undergo both liver and kidney transplantation. Because use of gadolinium-based contrast agents is dangerous in patients with impaired kidney function, development of effective non-contrast MR methods to image the hepatic and renal vasculature is of immense clinical importance. This chapter investigates the performance of two NCE-MR sequences – VIPR-SSFP and IFIR – according to several image quality criteria. The ability of these sequences to detect non-vascular pathology is also explored.

Chapter 4 (*Dynamic Contrast-Enhanced MRI and Quantitative Perfusion Modeling in the Liver*) describes an approach to quantitative perfusion modeling in the liver using DCE-MRI data that are discontinuous due to breath hold-based motion compensation. Quantitative perfusion MRI holds the potential to enhance clinical diagnosis of CLD as well as focal liver lesions; however, a means of accurately measuring hepatic perfusion

parameters that is robust to liver motion must be developed. In this chapter, an approach based on sequential breath holds combined with weighted nonlinear regression of the raw data to a quantitative perfusion model is described. This model is applied to a cohort of 12 healthy volunteers and 10 patients with HCC; differences in perfusion parameters between normal liver, diseased liver and tumor are investigated.

Chapter 5 (*Summary and Future Work*) reviews the contributions of this dissertation and suggests future directions for expanding upon work outlined in previous chapters. In particular, several avenues of advancement for quantitative perfusion MRI are discussed.

Chapter 1: Background

1.1 Natural History and Etiology of Chronic Liver Disease

Chronic liver disease (CLD), cirrhosis and hepatocellular carcinoma (HCC) remain major health problems in the United States and other developed countries[1]. CLD is generally defined as a disease process that causes inflammation and cell death within the liver, eventually leading to liver scarring (fibrosis) and cirrhosis (permanent damage to the hepatic parenchyma). In 2002, CLD was the 12th leading cause of death in the general US population[2], and the 7th leading cause of death among persons 25-64 years of age. Outside the US, over 700,000 people die each year from cirrhosis[3], which by 2020 is projected to be the 12th leading cause of death worldwide[4]. Besides cirrhosis, the other major sequel of CLD is hepatocellular carcinoma (HCC), of which over 600,000 cases occur each year worldwide. HCC has a 5-year survival rate of just 8.9%[5], making it the second-most lethal primary cancer after pancreatic adenocarcinoma.

In the United States, chronic alcoholism, hepatitis C virus (HCV) infection[6] and non-alcoholic fatty liver disease (NAFLD)[7] are the primary causes of CLD and cirrhosis. Unfortunately, many patients who present with CLD do so in the late stages of disease, having experienced either an unknown infection with HCV or having suffered from NAFLD for several years or longer. Because HCV infection and NAFLD tend to be asymptomatic until liver fibrosis has become significant enough to cause hepatic

dysfunction, these forms of liver disease afford few opportunities for early diagnosis – though this may be improved with the advent of non-invasive imaging of hepatic fibrosis[8, 9]. Additionally, while new molecular targets for anti-fibrotic agents are being investigated, most drug candidates investigated thus far remain in the pre-clinical trial stage of development[10, 11]; and currently available anti-fibrotic agents are typically too toxic for long-term use[12]. The number of medical interventions available to treat CLD, even when detected early in its course, is thus limited.

Unfortunately, the biological and clinical manifestations of chronic liver disease are numerous. As CLD progresses, many of the liver's biosynthetic and degradative functions become impaired. This can result in several extrahepatic pathologies, including ascites due to reduced plasma albumin concentration; increased prothrombin time due to reduced synthesis of clotting factors; and splanchnic vasodilation / hyperdynamic circulation due to impaired breakdown of circulating vasoactive neurotransmitters[13, 14]. The alterations in splanchnic blood flow caused by CLD are particularly significant due to the fact that they often occur in the setting of severe hepatic fibrosis, which increases resistance to blood flow through the liver considerably[15]. The net effect of these disturbances is that blood flow through the portal vein will be reduced in late-stage CLD. To compensate for this loss of portal venous flow, the hepatic artery – which usually supplies about 20% of the blood flow to the liver – will dilate to such a degree that the perfusion required by the liver to continue functioning is maintained[16]. Over time and with worsening liver disease, the restriction of flow through the portal vein will become more severe, resulting in an

increase in portal venous pressure (portal venous hypertension). In some patients, the portal venous pressure can become so high that it causes retrograde flow through adjacent venous collaterals – portal venous hypertension thus manifests with specific clinical symptoms, including splenomegaly, esophageal varices and caput medusae[15]. Esophageal varices are a particularly dangerous complication of CLD, as patients with extant varices and a portal venous pressure over 12 mm Hg are at significant risk for variceal rupture and catastrophic blood loss[14].

Additionally, because of ongoing inflammation in the liver, hepatocyte death and turnover occurs at a much higher rate than in normal liver tissue, predisposing the liver's parenchymal cells to accumulated genetic errors and carcinogenesis. Dysplastic nodules and HCC lesions are the eventual result of this pathophysiological process. The presence of HCC lesions within the liver significantly worsens the prognosis of patients with CLD, especially if the number or size of lesions exceeds the limits set by the Milan criteria[17] and excludes them from potentially curative liver transplant.

1.2 Chronic Liver Disease: Renal Effects

The splanchnic vasodilation that occurs in late-stage chronic liver disease causes an effective decrease in circulating blood volume due to the increased caliber of vessels in the gut. If this vasodilation becomes chronic, the renin-angiotensin-aldosterone system will be activated to effect volume repletion; further, the renal arteries will constrict to directly reduce the glomerular filtration rate. These changes, though normal physiologic responses to volume depletion, are pathologic in the context of CLD. Chronic activation of the renin-angiotensin-aldosterone system and excess constriction of the renal arteries has been shown to result in deleterious effects on the kidneys[18]. Additionally, for as-yet-unknown reasons, in some cases CLD-related renal arterial constriction can lead to a clinical condition known as the hepatorenal syndrome (HRS), in which renal function rapidly declines despite normal histological appearance of the kidney on biopsy. Although poorly understood, the pathophysiology of HRS is directly related to the systemic vascular derangements caused by CLD; thus, the only definitive treatment is liver transplantation[18]. Many patients who are treated for HRS with a liver transplant will nevertheless experience acute renal failure, and in some cases will require a kidney transplant as well[19]. It is unknown whether this post-transplant renal disease is related to HRS or whether it is simply a complication of hepatic allograft placement.

1.3 Natural History and Diagnosis of HCC

HCCs are highly vascularized tumors which draw most of their blood supply from the hepatic artery[20]. HCC lesions occur quite commonly in the setting of CLD and cirrhosis; in fact, the risk of a new HCC lesion in a cirrhotic patient is approximately 1.5% per year[21], and in certain patients the 5-year risk of developing HCC is as high as 30%[20]. As mentioned previously, HCCs are thought to develop due to the chronic inflammation and increased cell turnover that occur within the liver in patients with CLD. Although HCCs may be diagnosed as solitary lesions, small HCCs (less than 5 cm) are usually asymptomatic, making clinical detection unlikely. Large HCCs and multifocal disease tend to deleteriously affect liver function, leading patients to seek clinical care which results in diagnosis of the tumor. HCCs may occur in non-cirrhotic livers, but this is relatively uncommon. Most HCCs occur in the setting of cirrhosis; unless these HCCs are detected at an early stage (less than 2 cm), there is typically local spread of tumor cells beyond the margin of the lesion. Once HCCs have grown beyond 5 cm, the likelihood of local spread and vascular invasion increases significantly. The most common sites of HCC metastasis are the lung, bone, and abdominal lymph nodes[22], although only approximately ten percent of patients presenting with HCC have extrahepatic disease.

Because HCCs often occur without any specific symptoms, identification of patients who are at high risk for HCC is extremely important. The American Association for the Study of Liver Diseases has released guidelines regarding which patients should

be monitored for development of HCC; the guidelines primarily focus on patients with cirrhosis and patients with diseases that place them at significant risk for cirrhosis[23]. Although the serum alpha-fetoprotein level was previously used to screen these patients for development of HCC, the low sensitivity and specificity of this test have caused it to be replaced by serial ultrasound surveillance. Current guidelines require high-risk patients to undergo a screening ultrasound exam every six months. If a liver nodule less than 1 cm is noted, the exam is repeated in another six months; nodules greater than 1 cm necessitate further imaging with either multiphase CT or contrast-enhanced MRI. CT and MR imaging are both very sensitive and specific for HCC if certain imaging criteria are used for lesion identification. MRI has been shown to provide somewhat higher sensitivity for HCC diagnosis than CT (81% versus 68%) using pathologic examination of explanted or resected liver as the reference standard[24], but this increased sensitivity may be offset by the high cost of the MRI exam. Definitive diagnosis of HCC is typically made using medical imaging results alone; only in unusual or inconclusive cases is liver biopsy required[23].

1.4 Treatment of HCC

Hepatocellular carcinoma is a notoriously difficult tumor to treat due to its location in the liver, one of the most highly vascularized organs in the body. This enhances the lesions' ability to metastasize either to secondary sites within the liver or to other locations in the body. Additionally, as HCC almost always occurs in the background of a cirrhotic liver, multiple independent lesions often exist simultaneously. Although one

or more lesions may be clinically apparent in a given patient, other lesions may escape detection or fall below imaging criteria for definitive diagnosis. Due to these complicating factors, the Milan criteria were devised in order to provide guidelines on patient eligibility for liver transplantation in the context of existing HCC lesions. The Milan criteria state that in order to be transplant-eligible, patients must have one lesion less than 5 cm in size, or up to three lesions less than 3 cm in size; additionally, the patient's tumor(s) must show no signs of vascular invasion (which would increase the risk of metastasis) and there must be no signs of extrahepatic disease (e.g. hypervascular lesions in the lung)[22]. If a patient's disease burden falls within the Milan criteria, he or she is typically eligible for liver transplant, which in many cases is a curative treatment. However, due to the low availability of hepatic allografts, patients typically must have severely compromised liver function before they become candidates for transplantation. In the United States, the Model for End-Stage Liver Disease (MELD) score[25] is used as the key criterion for patient rank on the transplant list; this model incorporates only serum bilirubin, serum creatinine and INR as measures of overall hepatic function. As a result, patients with solitary HCC lesions and good hepatic function are poor candidates for organ allocation. However, several other potentially curative treatments for HCC are available for individuals with low disease burden and intact liver function.

In the setting of small, solitary HCC lesions, several curative treatment options besides liver transplant are available. Among the most common used in modern clinical practice are radiofrequency ablation (RFA) and surgical resection of the HCC lesion.

RFA is rapidly becoming the de-facto standard for treatment of HCC lesions in patients with cirrhosis or patients with impaired liver function (Child-Pugh Class A or B)[26]. RFA has been shown to be extremely effective in controlling lesions less than 2 cm in size, with a reported 5-year survival rate of nearly 70% in patients from this group treated with RFA alone[27]. RFA is also effective in controlling larger lesions, though its efficacy diminishes rapidly with increasing lesion size. However, RFA's ability to treat lesions near the periphery of the liver is limited by the possibility of heat-induced damage to other organs (e.g., kidneys); additionally, RFA is less effective when used to treat lesions near major vessels due to the "heat sink" effect. It is likely that the high survival rate associated with RFA stems in part from its ability to induce rapid necrosis not only in the tumor itself, but also within an arbitrary margin of normal liver tissue surrounding the lesion where tumor cells have likely migrated.

Direct resection of HCC lesions is sometimes performed, but only if the lesions are small and confined to an individual Couinaud segment of the liver[26]. This usually requires the lesion to be noted incidentally on imaging, as lesions of this size are typically asymptomatic[20]. However, resection of solitary HCCs less than 2 cm in size in non-cirrhotic livers is associated with a cure rate as high as 90%. Compared to RFA, resection is almost never undertaken in the setting of cirrhosis due to the reduction in liver function that occurs after this procedure. Resection is rapidly falling out of favor in patients with cirrhosis due to the fact that RFA has been shown to be equivalently effective in treating small HCCs while minimizing post-procedure damage to liver function. RFA also results in considerably fewer complications and side effects versus

surgical removal of HCC via resection due to the relatively non-invasive nature of the RFA procedure.

Unfortunately, by the time HCC is diagnosed, many patients have sufficient disease burden to place them outside of the Milan criteria. Other patients may have lesions that fall inside of the Milan criteria, but are sufficiently large (3-5 cm) that the cure rate of RFA is significantly reduced; meanwhile, these individuals' liver function is not sufficiently poor to qualify them for liver transplant. In these cases, other treatment options are available, though these treatments will either serve as a bridge to transplant or are viewed as palliative in nature. One of the most commonly used treatments for locally advanced disease is transcatheter arterial chemoembolization (TACE)[28]. In TACE, an intra-arterial catheter is advanced into the vessels feeding an HCC lesion, or into the vessels feeding the segment of liver in which multifocal disease exists. A combination of chemotherapeutic drugs and embolic agent are then administered; this causes rapid tumor necrosis as well as significant hepatic necrosis depending on the particular vessels chosen for treatment. TACE has been shown to significantly increase survival in patients with unresectable (non-ablatable) HCC[29]. However, TACE must be performed with caution in patients who have diminished liver function, as the procedure may induce liver failure if too large a portion of the hepatic parenchyma is treated.

In patients whose disease has spread throughout the liver or outside of the liver, systemic chemotherapy is typically the only treatment option available. Until recently,

no chemotherapeutic agents had been shown to provide a definitive survival benefit to patients with advanced HCC. However, a randomized controlled trial in 2008 demonstrated that the multikinase inhibitor sorafenib extends life in these patients[30], though it does not induce a radiological response (e.g. tumor shrinkage by RECIST criteria) in most HCC lesions. Sorafenib acts to disrupt the signal transduction pathway of the vascular endothelial growth factor (VEGF) receptor in addition to inhibiting many other cell growth-related kinases; it would thus seem well suited to treat HCC, a hypervascular tumor that requires significant perfusion. However, compared to placebo sorafenib only increases life expectancy by about three months in patients with advanced HCC (7.9 months in the placebo group versus 10.7 months in the treatment group)[26]. Despite the modest nature of this survival benefit, it has been reported in the literature that some patients survive significantly longer than 10 months after undergoing sorafenib therapy[31]. This raises the question of whether there are certain HCC subtypes with specific genetic or physiological characteristics that render them more susceptible to the cytostatic/cytotoxic effects of sorafenib, as well as how it may be possible to detect those individuals who would receive maximum benefit from sorafenib therapy.

1.5 Role of MR Imaging in CLD

Undoubtedly, CLD and its long-term complications – cirrhosis, HCC and hepatorenal syndrome – impose a considerable burden both on patients and on the modern health care system. Improvement in diagnosis of and refinement in treatment

methods for these conditions would provide significant benefit to the patients who suffer from them. Modern imaging methods, such as magnetic resonance (MR) imaging, hold great promise to enhance the detection of CLD[8, 9], as well as to improve the targeting of medical interventions for this disease. Although MRI is already highly utilized in the clinical management of CLD patients[32, 33], its current implementations have several shortcomings that can diminish its diagnostic and interventional efficacy. This thesis will focus on investigating potential improvements to three implementations of MR imaging in particular: the use of fat-water MRI to guide treatment placement in TACE[34]; the use of non-contrast MR angiography to visualize the renal vessels in patients who have undergone kidney transplant; and the use of dynamic contrast-enhanced (DCE)-MRI for diagnosis of hepatocellular carcinoma and detection of treatment response to anti-angiogenic agents such as sorafenib.

First, with the advent of real-time interventional imaging, MRI is poised to make a significant impact on the treatment of HCCs. Because these tumors are often treated using transcatheter arterial chemoembolization (TACE), the ability to track the arterial catheter in real-time and to monitor the administration of contrast agent would greatly improve the targeting and dosing of chemoembolic agent. This thesis will investigate the potential of ethiodized oil – an emulsifying agent used to deliver chemotherapeutic drugs and to provide contrast on x-ray DSA and CT imaging – to serve as a contrast agent on fat-water MR imaging. The use of MRI instead of x-ray DSA and CT for administration TACE therapy and verification of treatment distribution would significantly reduce the radiation dose to which patients are exposed.

Next, with the recent realization that nephrogenic systemic fibrosis (NSF[35]) is linked to administration of gadolinium contrast agents, clinicians are unable to use these agents to image persons with low kidney function. This often complicates the management of CLD patients, many of who suffer from coexisting hepatic and renal pathologies. The development of effective non-contrast enhanced MR angiographic (NCE-MRA) methods for imaging the renal vasculature would restore clinicians' ability to visualize important renal pathologies associated with CLD, such as renal artery stenosis and renal vein thrombosis, that can often not be detected using ultrasound[36]. In this thesis, a novel NCE-MR sequence – VIPR-SSFP[37] – is compared to a Cartesian SSFP-based method (IFIR) that currently serves as a clinical gold standard for non-contrast renal angiography. Because IFIR utilizes an inversion pulse before its SSFP readout, it nulls signal from veins as well as static tissues in the imaging volume, which prevents several important vascular pathologies from being visualized. The diagnostic abilities of the sequences are compared in a group of renal transplant patients, in whom rapid diagnosis of vascular pathologies is of considerable clinical importance.

Finally, while DCE-MRI is often used to monitor for development of HCCs in patients with long-standing liver disease, current DCE-MR sequences are limited by several technical shortcomings. The most significant of these is the poor temporal resolution of commercial CE-MRI implementations (roughly 12-20 seconds/frame[38]). This can sometimes result in mis-timed acquisition of the important arterial phase of contrast enhancement in the hepatic parenchyma, significantly impairing detection of

HCC. In this thesis, the utility of a 3D radial sequence with low temporal footprint based on the VIPR trajectory[39] to perform DCE-MR imaging of the liver is investigated. Data acquired using this method is also used to perform quantitative and semiquantitative modeling of hepatic perfusion parameters, and the utility of these parameters in differentiating normal liver from diseased liver and tumor is explored.

MR imaging is uniquely suited to address the clinical challenges described above, and thus to improve several aspects of CLD diagnosis and treatment. The development of novel MR-based methods to address these challenges – HCC detection with DCE-MRI, visualization of treatment localization during TACE with fat-water MRI, and vascular imaging in the presence of kidney disease with non-contrast MRI – has the potential to simplify the identification and treatment of these CLD-related complications, and to therefore improve the clinical management of chronic liver disease as a whole.

Chapter 2: Detection of Ethiodized Oil after TACE Treatment with IDEAL Imaging

2.1 Background: Visualization of TACE Treatment Region using MRI

Transcatheter arterial chemoembolization (TACE) has significant utility in the treatment of malignant neoplasms of the liver, particularly HCC, that are not amenable to surgical resection or cure with transplantation[34]. Traditionally, TACE delivers a bolus of chemotherapeutic agents suspended in ethiodized oil (ethiodol) through a hepatic arterial catheter placed under fluoroscopic guidance. A follow-up CT scan is then used to verify correspondence between the tumor and treatment sites. Fluoroscopy typically provides limited visualization of the tumor; therefore, interventional radiologists often treat large, extended volumes of the liver, which can deleteriously affect hepatic function. Real-time MR guidance of TACE, which can visualize both tumor and its supplying hepatic arterial vasculature, may thus be useful for targeting chemoembolic treatment and sparing normal liver[40]. However, in order for real-time MR imaging to become feasible, an MR-active contrast agent equivalent to the iodine-based agents used in traditional fluoroscopy must be developed and validated. The purpose of this work is to demonstrate that ethiodol, the substance used to emulsify the chemotherapeutic drugs administered during TACE, can serve as contrast material not only under fluoroscopy/CT but also under MRI.

Because ethiodol is principally composed of iodinated ethyl esters of the fatty acids of poppy seed oil, and has NMR behavior similar to that of common oils, it can be visualized with chemical shift based water-fat separation methods such as iterative decomposition of water and fat with echo asymmetry and least-squares estimation (IDEAL[41]). IDEAL exploits the differences in resonance frequency between fat and water protons to separate the MR signals generated by each of these species. By fitting the MR signal using a least-squares algorithm, IDEAL can resolve the signal into components arising from an arbitrary number of chemical species while simultaneously providing an estimate of the local field map. Moreover, IDEAL is robust in that it corrects for both T_2^* [42] and T_1 bias[43] due to the short T_1 of fat versus that of water, which allows it to provide accurate estimates of hepatic fat fraction at both low (<10%) and high (>50%) fat fractions as well as in the presence of iron. For the simple problem of three unknowns: water signal, fat signal and local field strength Ψ_0 : the IDEAL algorithm is optimized when data are acquired from three echoes whose phase (i.e., the phase difference between the water and fat signal) is equally spaced around the unit circle. In situations where T_2^* correction is required, six or more echoes must be acquired to allow for the MR data to be fit to the IDEAL model. Because of its correction for T_1 bias and T_2^* , its SNR-optimized multi-echo acquisition and its ability to acquire images of the entire abdomen in a single breath hold, IDEAL has proven itself considerably superior to standard Dixon fat-water techniques, and should serve as an excellent platform for visualizing fat-based contrast agents under MRI.

When injected into the hepatic artery, ethiodol embolizes within tumors such as HCC[44] and remains localized within the lesion for a significant duration of time (up to one year). Ethiodol contains a high concentration of iodine (475 mg/mL) for visualization during injection under fluoroscopic guidance, and for follow-up with CT. The oil component of ethiodol, however, can also serve as a contrast agent when imaged with IDEAL. In this work, the ability of IDEAL to visualize the ethiodol distribution in the liver will be investigated in two different contexts: first, in a small cohort of patients who have undergone a TACE procedure and have returned for follow-up approximately one month after chemoembolization; and second, in a swine model with ethiodol injection into a branch of the hepatic artery performed immediately before imaging. Because ethiodol disperses into small droplets upon injection into the vasculature, it is embolic even when not mixed with ancillary substances such as cyanoacrylate or microspheres[45]. However, while ethiodol is known to embolize within HCCs, its long-term behavior in normal liver tissue remains to be investigated. Thus, for the swine experiments described below, the ethiodol was mixed with microspheres before injection in order to ensure that it did not simply flow through the hepatic vasculature.

2.2 MR Imaging of Ethiodol Distribution at TACE Follow-Up

2.2.1 Methods

Patients who undergo TACE typically remain hospitalized for some time after their procedure in order to ensure that the chemoembolic treatment has not deleteriously affected their liver function[34]. During the 1-2 day post-procedure period, patients receive a CT scan in order to verify that the location of treatment matches the location of the tumor. In addition, patients are asked to return to the hospital after 4-6 weeks for a follow-up CT scan to determine what effects the TACE procedure has had on the size of the treated lesions. Due to the fact that HCCs selectively retain ethiodol[44], treated lesions almost always exhibit substantial contrast on CT imaging at follow-up. Because patients who have undergone TACE are usually not ambulatory for some time after the procedure, and because the concentration of ethiodol in HCCs remains high at the time of TACE follow-up, the optimal time obtain MR images of the post-TACE ethiodol distribution is when patients return to the hospital for follow-up CT scanning. This allows for MR and CT images to be acquired on the same day, which enables direct comparison of these two imaging modalities and should assist with determination of their relative sensitivity for ethiodol-based contrast.

Patient Recruitment

After obtaining IRB approval, 5 patients scheduled to undergo TACE were recruited through the Department of Interventional Radiology at the UW Hospital and Clinics (UWHC). Nurses in this Department identified patients scheduled for procedures in the near future; these patients were subsequently asked if they would like to participate in a research MR examination. Patients were told that the imaging session would take about 30 minutes and that the entire study visit would last about 45 minutes. Patients who agreed to be scanned signed an IRB-approved consent form for imaging with the IDEAL sequence.

Imaging Procedure and Data Analysis

Patients were imaged using a multi-echo 3D spoiled gradient echo (SPGR) implementation of IDEAL (3D-IDEAL-SPGR[46]) with correction for T_2^* decay[42]. After obtaining informed consent, imaging was performed on a 1.5 T scanner (Signa HDx TwinSpeed, GE Healthcare, Waukesha, WI) with an 8-channel phased array cardiac coil. Imaging parameters included: 6 echoes per TR with flyback readout gradients, TR = 13.5 ms, $TE_{\min} = 1.3$, $\Delta TE = 2.0$ ms, 256x160 matrix, 22 slices, 10 mm slice thickness, BW = ± 142 kHz, 35x27cm FOV, 5° flip angle to minimize T_1 related bias[43], and parallel imaging acceleration with 2D-ARC[47] (R=2.2), for a total scan time of 21 seconds. All scans were performed within a single breath-hold. Separate water, fat and

fat fraction images were calculated with an on-line reconstruction algorithm that uses a region growing algorithm to prevent water-fat swapping[48].

The presence of fat in the liver was assessed both qualitatively and quantitatively using the IDEAL fat-only and fat-fraction images. The intensity and distribution of ethiodol signal on MR was qualitatively compared with its distribution as seen on CT, which is the current clinical gold standard for ethiodol imaging. Any significant discrepancies between the regions of treatment on the CT and MR exams were noted.

2.2.2 Results

Figure 2.1A shows an immediate post-TACE CT image of the liver obtained from the first patient (Patient 1) who was scanned as a part of this study. The circular, high-contrast region of the image (white arrow) represents an HCC that was treated with TACE; the contrast in this case is generated from the iodine component of the ethiodol administered during the procedure. Figures 2.1B, 2.1C and 2.1D show IDEAL water-only, fat-only and fat-fraction images of the same patient obtained approximately one month after TACE. Although the signal in the treated region is not significantly different

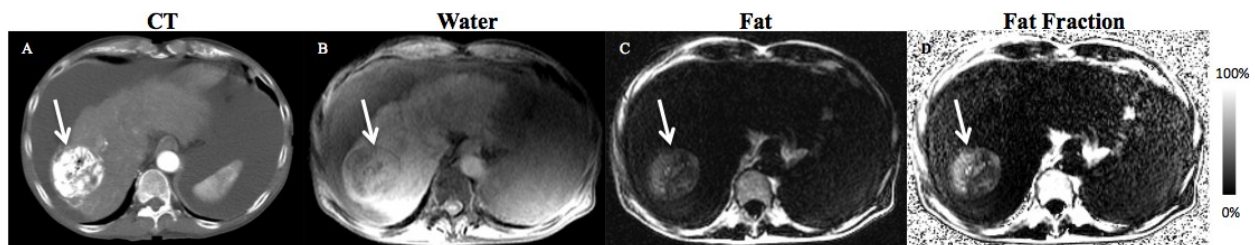
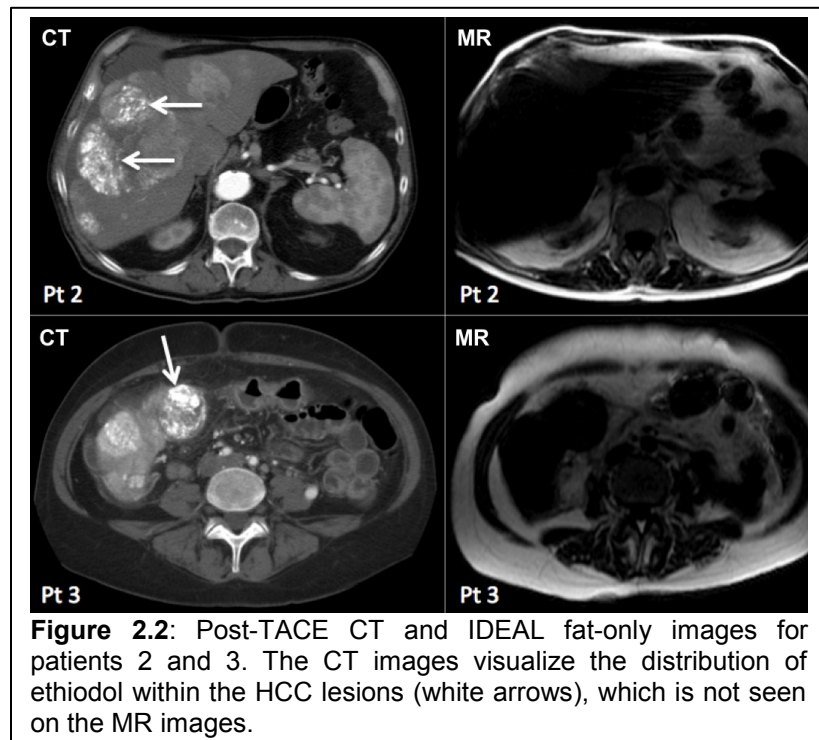


Figure 2.1: Images from a 71-year-old male with cirrhosis and a known HCC in the right lobe of the liver treated with ethiodol-based TACE. An arrow shows the tumor location in each image. (A) CT demonstrates a hyperdense region corresponding to the ethiodol distribution. Separated (B) water, (C) fat, and (D) calculated fat fraction images are also shown.

from background liver tissue in the water image, the treated region is immediately apparent in the fat image. Additionally, the treated region is easily visualized in the fat-fraction image, where the amount of fat in the treatment ROI is measured to be 17.5%. Evidently, ethiodol is serving as an effective contrast material using fat-water MR imaging based on this data.

Figure 2.2 shows CT and MR images from two additional patients (Patients 2 and 3) who were treated with TACE. In this case, both CT and MR images were obtained at the time of follow-up, approximately one month after the TACE procedure. Compared to the images in Figure 2.1, it is apparent that in these patients, the ethiodol is not providing adequate contrast to make the treatment regions visualizable in the MR images. Although it is possible that the amount of ethiodol present in these patients' HCCs at one month is sufficient to provide contrast on CT but not on MR, this seems unlikely, as the

attenuation in the treatment ROI for Patient 2 on an immediate post-TACE CT scan is not substantially higher than that in the one-month follow-up scan (data not shown). There are, however, several alternative explanations



for these results. First, it is possible that the initial patient who was scanned in Fig. 2.1 had fat *within his HCC lesion*, and that it was this fat which provided contrast on IDEAL. However, only one-third of HCC lesions contain histologically-detectable amounts of fat[49], with a smaller fraction containing an amount sufficient to be detected on MR imaging. Additionally, the distribution of signal enhancement on the IDEAL fat-only image (Figure 2.1C) is very similar to the distribution of attenuation within the lesion on CT (Figure 2.1A), which corresponds to ethiodol – thus, it seems unlikely that the fat signal seen on IDEAL imaging arises from intracellular fat within the HCC.

A second and more plausible hypothesis is that the physiologic and metabolic fate of ethiodol within HCC plays some role in explaining the difference between the CT and MR results seen in these patients. In normal liver, where ethiodol is eliminated with a half-life of about 4 days[50], it has been shown that particles of ethiodol are taken up by Kupffer cells and fat-containing stellate cells in the sinusoids and the space of Disse, respectively[51]. Several previous studies have postulated that the longevity of ethiodol within HCC is simply due to a lack of reticuloendothelial function and lymphatic flow within the tumor[52], which would be consistent with the known mechanism of ethiodol elimination from the liver. Thus, the temporal dynamics of the fat signal provided by ethiodol on MR should follow a similar pattern as those of its X-ray attenuation on CT – the fact that ethiodol's fat signal seemingly disappears more quickly than its CT attenuation implies that it is being chemically decomposed within the HCC. Breakdown of the fatty components of ethiodol could reduce or eliminate the MR signal from fatty

proton resonances despite the fact that the iodine component remains; this would explain why contrast from the ethiodol is still seen on CT, but not on MR.

2.2.3 Conclusions

It is apparent from the above data that ethiodol is not a reliable contrast agent under MRI at the time of TACE follow-up (approximately one month after the procedure). Due to the mixed results seen in the first five patients enrolled in this study, further enrollment has been postponed. However, a substantial ethiodol signal was seen in one patient's HCC on the IDEAL fat-only image. Given this result, as well as the possible metabolic fate of ethiodol within HCC, it seems plausible that imaging ethiodol with IDEAL immediately after its injection should allow for substantially more contrast to be generated by the fat component of this material.

2.3 *In vivo* injection of ethiodol into liver of swine model

2.3.1 Background

Although it was not possible to consistently visualize ethiodol on IDEAL imaging one month after its injection under TACE, the ethiodol's ability to provide contrast may have been curtailed by metabolic degradation of its fatty component. Therefore, to investigate the hypothesis that ethiodol provides contrast under MR in the short term (1-2 days), a swine model was used to perform injection of ethiodol directly into the hepatic parenchyma while the animal was in the MR scanner. In addition to providing the ability to image ethiodol immediately after its administration, this "real-time" injection of ethiodol serves to mimic the injections of chemoembolic agent that would take place during an MR-guided TACE procedure.

As noted above, ethiodol disperses into small droplets upon injection into the hepatic artery and should be embolic without any additives. However, in order to ensure that the ethiodol does not pass through the liver, it was mixed separately with glue and microspheres to enhance its embolic potential. Two injections (ethiodol / microspheres and ethiodol / glue) were performed in different lobes of the swine liver, as described below.

2.3.2 Methods

A female swine was placed under general anesthesia with isoflurane (4% induction, 1.5-3% maintenance) and intubated, with breathing controlled by a mechanical respirator. A 5-French catheter was inserted into the right femoral artery and positioned under X-ray DSA guidance into a branch of the right hepatic artery. A 10mL mixture of ethiodol and glue (N-butyl cyanoacrylate) was subsequently injected into this artery. After the injection, the catheter was repositioned to a branch of the left hepatic artery. The animal was then relocated to the MR scanner so that IDEAL imaging could take place.

Once in the MR scanner, the animal was first imaged using IDEAL in

order to detect ethiodol from the original injection (ethiodol / glue) that was performed under X-ray DSA. Next, 10 mL of ethiodol mixed with 700-900 μm PVA microspheres

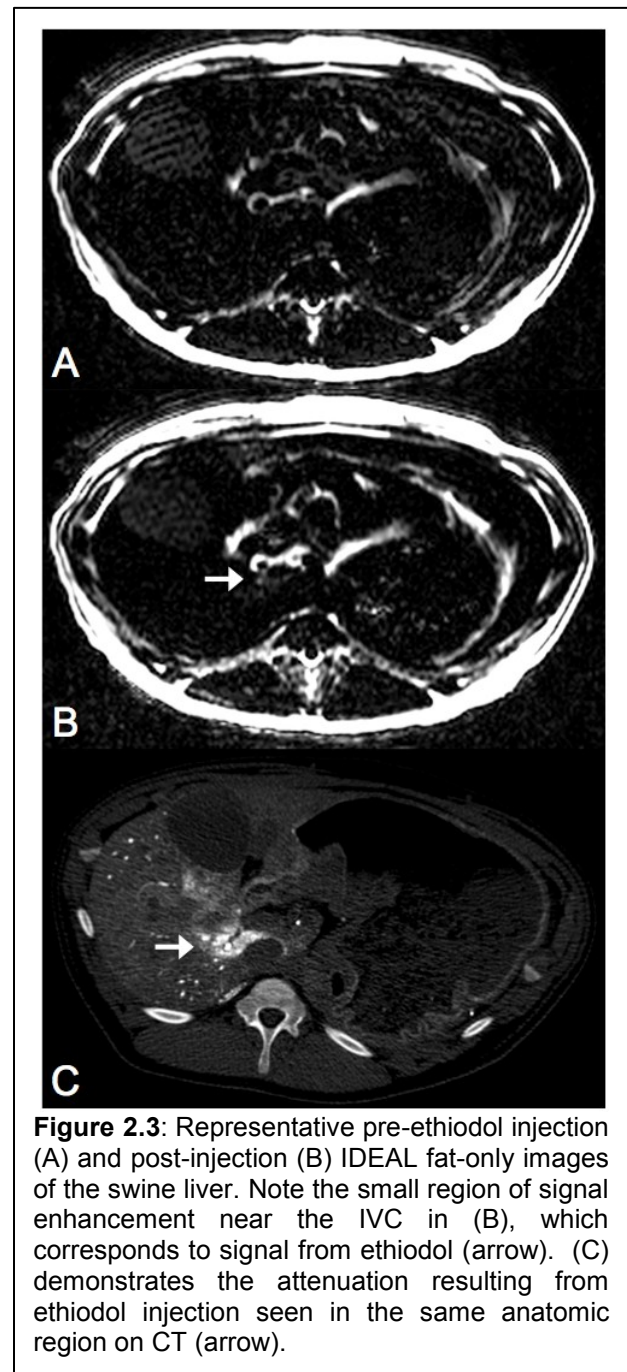


Figure 2.3: Representative pre-ethiodol injection (A) and post-injection (B) IDEAL fat-only images of the swine liver. Note the small region of signal enhancement near the IVC in (B), which corresponds to signal from ethiodol (arrow). (C) demonstrates the attenuation resulting from ethiodol injection seen in the same anatomic region on CT (arrow).

was injected into the femoral catheter. Within 10 seconds of this injection, a second IDEAL scan was acquired; once this scan had completed and images were reconstructed, a third IDEAL scan was performed in order to determine whether the short-term distribution of ethiodol after injection into the liver could be visualized.

The animal was imaged using a multi-echo 3D spoiled gradient echo (SPGR) implementation of IDEAL (3D-IDEAL-SPGR[46]) with correction for T_2^* decay[42]. Imaging was performed on a 1.5 T scanner (Signa HDx TwinSpeed, GE Healthcare, Waukesha, WI) with an 8-channel phased array cardiac coil. Image parameters included: 6 echoes per TR with flyback readout gradients, TR = 26.7 ms, $TE_{\min} = 1.54$ ms, $\Delta TE = 2.3$ ms, 256x256 matrix, 31 slices, 6 mm slice thickness, BW = ± 125 kHz, 36x36 cm FOV, 12° flip angle to enhance fat signal, and parallel imaging acceleration with 2D-ARC[47] for a total scan time of approximately 40 seconds. All scans were performed within a single breath-hold, which was generated by suspending mechanical respiration for the duration of imaging.

After MR imaging was completed and the animal was euthanized, the animal was moved to an adjacent CT scanner (Discovery CT 750, GE Healthcare, Waukesha, WI) where the abdomen was scanned with 1.25 mm slice thickness in order to generate control images of the ethiodol distribution within the liver.

2.3.3 Results

Figures 2.3A and 2.3B show representative pre- and post-injection IDEAL fat-only images of the swine liver. Although the pre-injection image volume should contain substantial signal from the ethiodol / glue mixture that was administered before the animal was moved to the MR scanner, this signal is not strong enough to rise above the noise floor of the normal liver tissue. The post-injection image volume also fails to show a significant amount of ethiodol signal with one exception: in a small region of liver near the IVC, signal enhancement can be seen in the IDEAL fat-only images, which measures about 6.5% fat fraction in the FF images. The anatomic location of this signal correlates with a region of high attenuation seen on CT (Fig. 2.3C). The CT images demonstrate a significant amount of ethiodol distributed throughout the liver; however, for the most part this signal is not evident on the IDEAL fat-only or fat fraction images.

2.3.4 Conclusions

Although it was possible to visualize ethiodol immediately post-injection using IDEAL imaging, the extent of ethiodol seen on the MR images did not match that of the ethiodol visualized on CT imaging. There are several reasons why this might be the case. First, it is likely that CT is inherently more sensitive to ethiodol than is IDEAL; this hypothesis is supported by the data from Section 2.2.4, where the ethiodol distribution in some HCCs could be visualized under CT but not MR. Additionally, the CT slices were 1.25 mm in thickness, while the MR slices were 6 mm; the image slices under MR

must necessarily be thicker in order to obtain full liver coverage within the time constraint of a single breath-hold. Because of the greater MR slice thickness, the ethiodol signal is averaged with signal from a significantly larger volume of normal liver tissue than it is under CT, reducing the signal intensity of ethiodol on IDEAL imaging. Finally, it is interesting that the only ethiodol signal visualized arose from the ethiodol / microsphere injection rather than the ethiodol / glue injection. When the ethiodol / glue mixture was administered, it was impossible to inject the entire 10 mL volume due to vascular resistance; however, the entire ethiodol / microsphere mixture was administered without issue. It is therefore possible that ethiodol signal from the latter injection was detected on MR simply by virtue of the volume of ethiodol that was injected, which increased the local fat fraction to a greater value. Because TACE procedures typically involve injections of 15-20 mL of ethiodol (plus chemotherapeutic agents), increasing the volume of ethiodol administered to this level in the experiments may thus increase the fat signal from the substance seen on IDEAL imaging.

Interestingly, work by Larson et al.[53] has demonstrated the feasibility of detecting lipiodol using chemical shift-based fat-water imaging in rodents. This work was based on measurement of the ^1H NMR spectrum of lipiodol, followed by use of a multippeak model of lipiodol's NMR spectrum for chemical shift-based imaging of lipiodol concentration. It is therefore possible that the standard multippeak model used by the IDEAL reconstruction is sub-optimal for detecting the fat proton resonances of ethiodol. However, because manufacturing of ethiodol has been discontinued as of March 2010,

measurement of its proton NMR spectrum would be difficult at this time due to supply shortage.

2.4 Future Work

Future work on this subject should focus on improving the MR contrast provided by ethiodol under IDEAL by enhancing similarity between the volume of the ethiodol injection in the swine model and that of the injection that occurs during the TACE procedure. By administering a larger volume of ethiodol (20 mL) into the liver, MR detectability will improve simply due to the increase in local fat fraction at the site of injection. Additionally, the ethiodol will be administered *before* the microsphere injection, in order to ensure that it reaches hepatic parenchyma before the sinusoids are embolized by microspheres. The microspheres will then serve to prevent the ethiodol from being flushed away by incoming blood. This procedure (injection of ethiodol followed by microspheres) is similar to that performed clinically on a significant fraction of TACE patients at UWHC, and will likely serve to enhance detectability of ethiodol within the liver using IDEAL.

Chapter 3: Visualization of renal transplant vessels using VIPR-SSFP and Cartesian SSFP (IFIR)

3.1 Background

Since its development in the late 1980s, contrast-enhanced magnetic resonance angiography (CE-MRA)[54] has served as a clinical gold standard for post-operative assessment of the renal transplant arterial and venous vessels[55]. CE-MRA has enabled diagnosis of a variety of post-transplant complications from a single imaging exam, including incomplete vessel anastomosis and pseudoaneurysm formation, donor/recipient renal arterial stenosis (RAS), peritransplant fluid collections, and renal vein thrombosis. Compared with Doppler ultrasound, CE-MRA provides significantly improved sensitivity for detection of RAS by enabling direct visualization of the vessel[56]. CE-MRA has also been shown to provide high sensitivity and specificity for detection of renal vein thrombosis in native kidneys[36].

Unfortunately, the implication of gadolinium-based contrast agents in the development of nephrogenic systemic fibrosis[57] has necessitated avoidance of CE-MRA exams in renal transplant patients. As a result, the clinical demand for robust non-contrast enhanced (NCE) MR angiographic (MRA) methods to image the transplant renal vessels has increased significantly. Recent work, beginning with the development of Time-SLIP[58], has produced several promising methods that are members of a

broader class of inflow-weighted balanced steady state free precession (bSSFP) sequences. These NCE-MRA sequences are designed to create bright signal only from renal arteries, as suspicion of arterial stenosis is the most common indication for renal MRA exams[59]. However, in transplant patients it is essential to visualize both venous and arterial anatomy, due to the substantial likelihood of pathologies involving the renal vein – such as anastomotic stricture or thrombus formation. Inflow-weighted bSSFP imaging methods, which cannot visualize these potentially catastrophic complications, are thus inadequate for comprehensive vascular evaluation of the renal allograft.

In this work, we utilize a bSSFP sequence based on a 3D radial trajectory – VIPR-SSFP[60] – and investigate its ability to image the vessels of the transplanted kidney. Like Cartesian SSFP methods (TrueFISP, FIETSA, bFFE), VIPR-SSFP generates images with T_2/T_1 contrast, enabling visualization of arteries and veins without administration of contrast material. However, VIPR-SSFP's radial acquisition gives it three distinct advantages over Cartesian SSFP sequences. First, VIPR-SSFP is less sensitive to motion than Cartesian methods, where motion manifests as coherent ghosting artifacts in the phase-encode and depth-encoding directions. Second, VIPR-SSFP's out-and-back trajectory permits very short TRs, enabling robust fat suppression using linear combination methods[61] and reducing banding artifacts known to impact SSFP acquisitions in the presence of inhomogeneous magnetic fields. Finally, the sequence's radial trajectory provides 3D volumetric coverage with a large FOV and true isotropic resolution, which allows data from a single scan to be reformatted along any desired orientation without compromising image quality.

The performance of VIPR-SSFP has previously been investigated in the context of breast lesion detection[62] and articular cartilage assessment[60, 63] with encouraging results. Here, we investigate the sequence's ability to visualize the renal transplant vessels, which are typically difficult to image using SSFP methods due to their location in the abdomen. The purpose of this study was to evaluate the performance of VIPR-SSFP in renal NCE-MRA when compared to Inflow IR (IFIR[64]), a commercially-available method within the family of inflow-sensitive SSFP sequences. IFIR, which is currently part of the routine clinical protocol for renal NCE-MRA at our institution, differs from VIPR-SSFP in several significant ways: it is based on a Cartesian bSSFP trajectory, it exploits an inversion slab to null venous signal and produce images with bright arteries, and it uses a frequency selective chemical saturation pulse for fat suppression. Our hypothesis is that VIPR-SSFP will provide arterial visualization quality similar to IFIR, while affording improved fat saturation in regions of B_0 inhomogeneity. Most important, however, is the fact that VIPR-SSFP will allow for simultaneous evaluation of renal vein pathology, an essential component of any comprehensive angiographic exam for renal transplant patients.

3.2 Materials and Methods

Patient Identification

After obtaining IRB approval for this retrospective study, we identified renal transplant patients who were scanned with both the VIPR-SSFP and IFIR sequences over a 30-month interval ending in November 2010. In total, twenty-one renal transplant patients were identified who received NCE-MRA exams using both sequences during the study period. Of these patients, 13 were male and 8 were female with ages ranging from 20 to 72 years. In each patient, kidney transplantation was performed as a result of chronic renal failure. Nineteen of the allografts were placed in the right iliac fossa, which is standard surgical practice at our institution; two were placed in the left iliac fossa. The duration of time from kidney transplantation to MR imaging ranged from 2 months to 11 years. The clinical indication for MR imaging in these patients was typically to rule out transplant renal artery stenosis as the primary cause of a significant increase in blood pressure or serum creatinine.

To investigate the image quality of the IFIR sequence with the inversion pulse disabled, one healthy volunteer was scanned using the IFIR sequence as well as a variant of the IFIR sequence with the inversion pulse disabled. This volunteer was scanned under an institutional IRB protocol that covers non-contrast enhanced research MR sequences.

Data Acquisition

The VIPR-SSFP k-space trajectory acquires two radial half-echoes per TR, which serve as the basis for its bSSFP readout[60]. Additionally, by selecting a center frequency halfway between the fat and water resonances and acquiring data from two complete passes of k-space – one without RF phase cycling and one with π -0- π -0 cycling – a linear combination of k-space data can be generated in which the stopband of the SSFP spectral response is centered over the fat resonance. This technique is termed LC-SSFP[61], and allows for robust fat suppression in anatomic regions where B_0 inhomogeneity is a concern.

Both IFIR and VIPR-SSFP scans were prescribed after obtaining scout images in the pelvis to locate the transplanted kidney. For VIPR-SSFP, a 3D spherical FOV was centered over the abdomen. For IFIR, an imaging slab was placed over the transplanted kidney and renal artery; the position of the inversion slab was determined automatically based on the imaging slab's location. Because IFIR utilizes parallel imaging acceleration, a calibration scan[65] was obtained before imaging commenced. The same localized shim volume was placed over the transplanted kidney for both scans.

For both sequences, tracking of the respiratory waveform was provided via respiratory bellows. During VIPR-SSFP scans, respiratory position was recorded for all TRs (radial projections), and only data from those falling in a certain range of the

respiratory waveform – the 50% nearest end-expiration – were used for image reconstruction[66]. The IFIR sequence used a respiratory trigger to initiate an inversion pulse during end-expiration of each breath, followed by a chemical saturation pulse[67] and balanced SSFP readout.

All patients were imaged with the IFIR and VIPR-SSFP sequences on a 1.5 T scanner (Signa HDxt; GE Healthcare; Waukesha, WI) using an 8-channel phased-array cardiac coil (GE Healthcare). The volunteer was imaged using only the IFIR sequence. Scan parameters corresponding to sequence differed slightly between patients due to variations in each individual's size and local anatomy near the renal allograft. Typical scan parameters for the VIPR-SSFP sequence included: 30° flip angle, TR = 2.6 ms, TE₁ = 0.3 ms and TE₂ = 1.8 ms, FOV = 36 cm spherical, and BW = ±125 kHz with a 256³ matrix and 1.4 mm isotropic resolution (total scan time was approximately 5-6 minutes depending on respiratory rate). Typical scan parameters for the IFIR sequence included: 70° flip angle, TR=4 ms, TE=2 ms, TI=1200 ms, FOV=36 x 36 x 24 cm, and BW=±75 kHz with a 256x256 matrix for a true spatial resolution of 1.4 x 1.4 x 2 mm³ resolution interpolated through zero-filling to 0.7 x 0.7 x 1.0mm³ (total scan time was approximately 4 minutes depending on respiratory rate). The inversion time for the IFIR scans was always set to 1200 ms per manufacturer recommendation, which effectively nulls signal from venous blood.

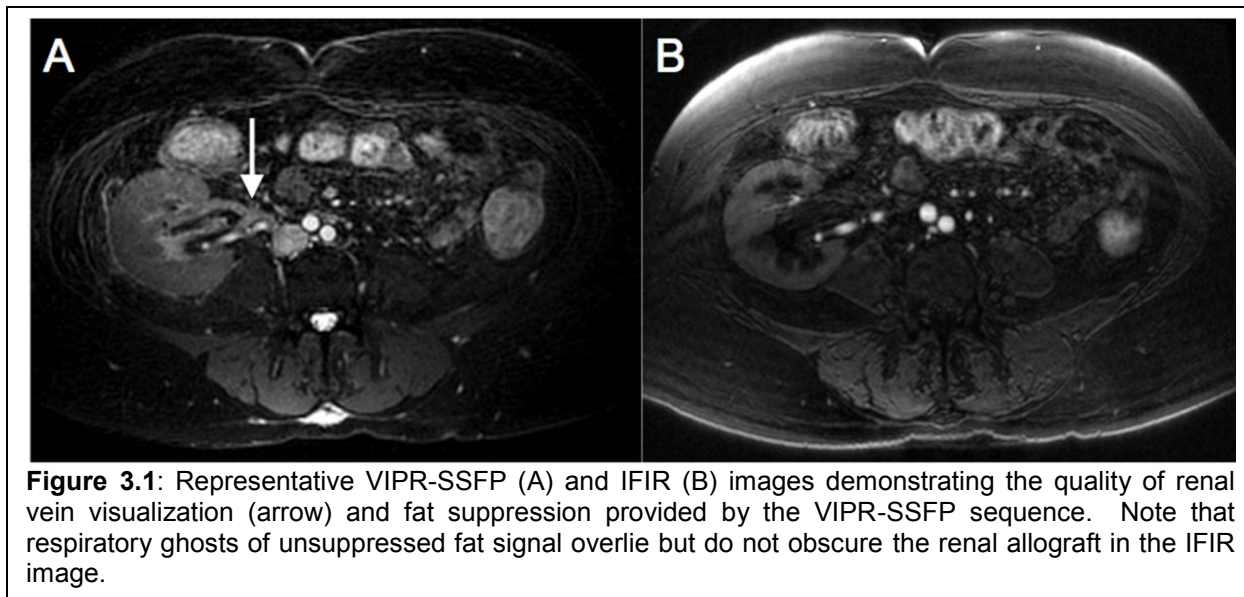
Data Analysis

Two experienced cardiovascular radiologists with 11 years and 28 years of experience, respectively, scored the IFIR and VIPR-SSFP images for each patient. Due to the obvious differences in appearance between Cartesian and radial acquisitions, it was not possible to blind the readers to the sequence associated with each image set.

The readers were instructed to assess four image quality criteria for each sequence on a 1-4 Likert scale (4 = excellent, 3 = good, 2 = poor, 1 = non-diagnostic). The criteria included overall image quality, quality of arterial visualization and quality of venous visualization (focusing on the ability to identify the vessel anastomoses as well as relevant pathologies, if present), and quality of fat suppression. Readers were instructed to score arterial and venous visualization quality at 2 or below if the vessel anastomosis or suspected vascular pathologies could not be visualized with confidence. Readers were also instructed to score fat suppression quality at 2 or below if unsuppressed fat signal was noted to obscure anatomy of interest due to respiratory ghosting.

Statistical Analysis

Results for each of the above criteria were analyzed using the Wilcoxon signed-rank test[68], a non-parametric statistical hypothesis test used to compare the relative quality of two different imaging methods. First, scores for the



VIPR-SSFP and IFIR sequences corresponding to the four criteria were first averaged between the two readers and across all patients. Next, Wilcoxon signed-rank tests were performed independently for each image quality metric, and p-values for each comparison were calculated. One of the two imaging methods was determined to be superior only if the difference in scores achieved statistical significance according to the Wilcoxon test.

3.3 Results

Sample images demonstrating the difference in venous contrast between VIPR-SSFP and IFIR can be seen in Figure 3.1. VIPR-SSFP was determined to be significantly superior to IFIR with regard to quality of venous visualization (Table 3.1). Neither reviewer scored any of the IFIR images as providing quality sufficient to evaluate the renal vein anastomosis, or to evaluate venous pathology if present.

However, the quality of arterial visualization provided by IFIR was statistically superior to that of VIPR-SSFP ($p=0.005$).

Because IFIR is designed to enhance signal only from arterial blood, it provides improved arterial visualization versus VIPR-SSFP;

nonetheless, the mean score for VIPR-SSFP arterial quality (2.97) remained significantly above the threshold of

diagnostic adequacy (2.0). A comparison of the arterial visualization quality of these two sequences can be seen in

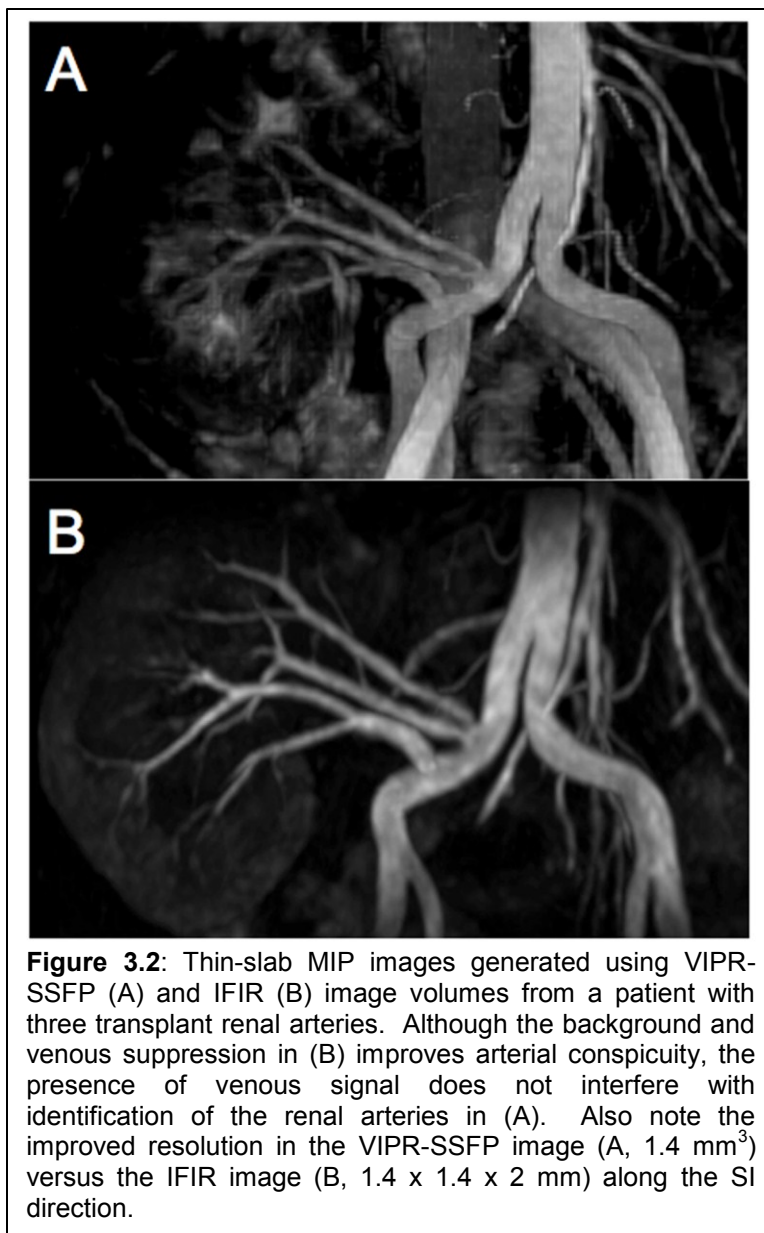


Figure 3.2, which shows IFIR and VIPR-SSFP thin-slab MIPs from a patient with three transplant renal arteries. Although enhancement of arterial signal is superior in the IFIR MIP (Fig. 3.2A), the presence of venous signal in the VIPR-SSFP image does not significantly impair visualization of the renal arteries (Fig. 3.2B). Although the IFIR sequence attained a slightly higher score in overall image quality, the difference between the two sequences was not statistically significant.

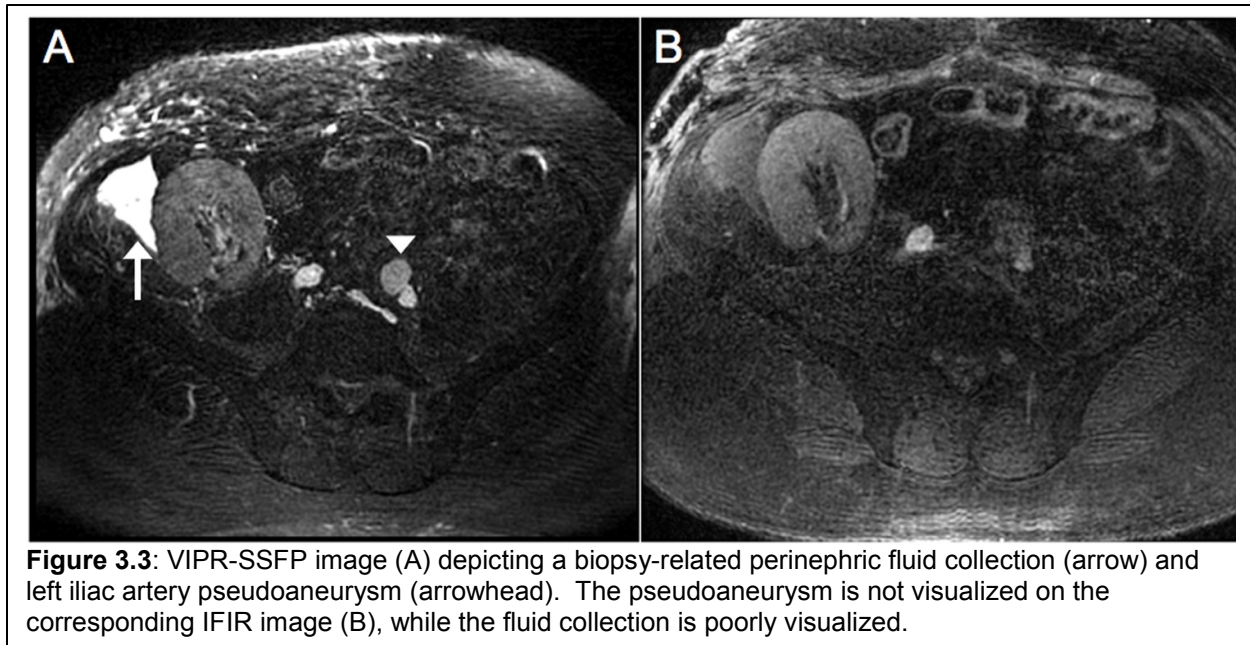
VIPR-SSFP
also provided
improved fat
suppression when
compared with IFIR,
and this difference

Mean Score by Criterion	IFIR	VIPR	p-value
Overall Image Quality	3.52	3.43	0.431
Quality of Fat Suppression	3.40	3.69	0.028*
Quality of Arterial Visualization	3.71	2.97	0.005*
Quality of Venous Visualization	1.00	3.13	0.00007*

Table 3.1: Scores for the four image quality criteria averaged across all patient images and between the two reviewers. VIPR-SSFP demonstrates statistically superior fat suppression and venous visualization, while IFIR provides superior arterial visualization. Note that no IFIR images were scored as being in the diagnostic range (≥ 3) with regard to quality of venous visualization.

was statistically significant ($p = 0.028$). While excellent (score = 4) fat suppression was not present in all VIPR-SSFP images – likely due to fat spins near areas of abdominal B_0 inhomogeneity falling outside the stopband of the spectral response – residual fat signal in these images typically had a less deleterious effect on diagnostic quality than that present in IFIR images. This can be seen in Figure 3.1, where residual fat signal due to B_0 inhomogeneity has a much more benign, distributed appearance in the VIPR-SSFP image (Figure 3.1B) relative to the coherent ghosting of fat in the phase-encoding direction with IFIR (Figure 3.1A).

The two study readers noted that the VIPR-SSFP images depicted several clinically relevant extrarenal findings that were not well visualized in the corresponding IFIR images. This is due to IFIR's use of an inversion pulse before its bSSFP readout, which nulls most signal from background tissue and any fluid collections present in the imaging volume. An example of such findings can be seen in Figure 3.3, where a biopsy-related perinephric fluid collection as well as a left iliac artery pseudoaneurysm are clearly visible in the VIPR-SSFP image (Fig. 3.3A) but are poorly visualized in the



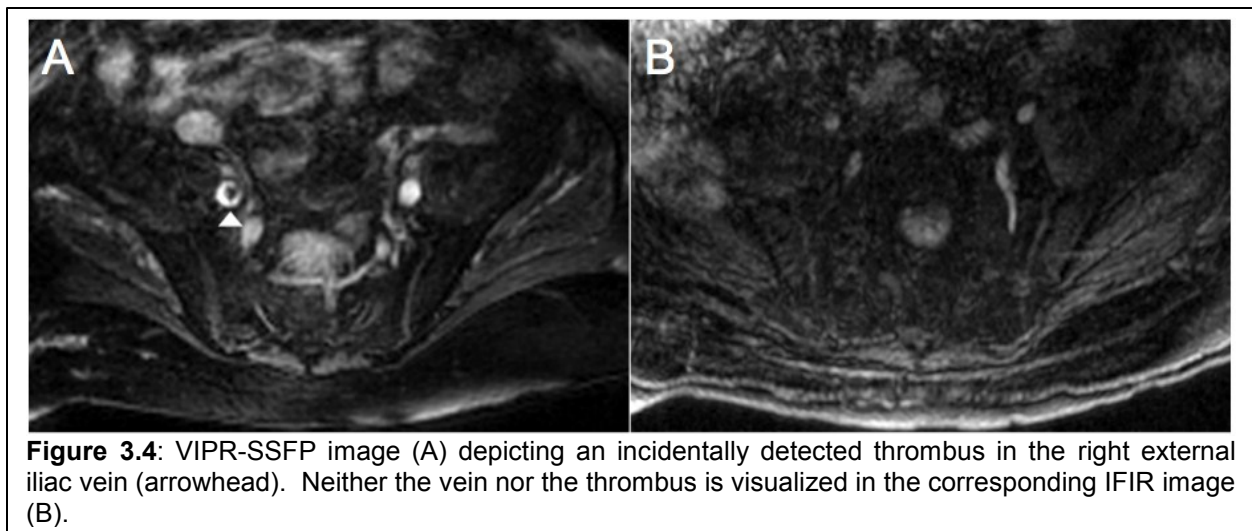
IFIR image (Fig. 3.3B). The pseudoaneurysm is not visible in the IFIR image because signal from slow flowing blood within this region was not sufficiently washed out with fresh spins during the 1.2-second TI. A second example can be seen in Figure 3.4A, which shows a thrombus in the right external iliac vein that can be seen using VIPR-SSFP image but is not depicted in IFIR image (Fig. 3.4B). Importantly, the inferior border of VIPR-SSFP's FOV (36 cm) extended significantly past that of IFIR's FOV (24 cm) in this patient, enabling visualization of the full extent of the thrombus. In addition to these extrarenal findings, VIPR-SSFP images frequently depicted transplant and native renal cysts that were not visualized in the corresponding IFIR images.

Figure 3.5 demonstrates the effect of disabling the IFIR inversion pulse on the arterial and venous visualization quality of this sequence. Figure 3.5A shows an IFIR thin-slab MIP depicting the renal arteries of a healthy volunteer; several segmental branches of the artery are clearly visible. In Figure 3.5B, with the inversion pulse

disabled, the segmental branches become difficult to distinguish from the renal veins. However, the IVC as well as the renal veins (arrows) are now visible. A renal cyst (arrowhead) can also be seen in Fig. 3.5B; the cyst appears as an area of low signal when the inversion pulse is enabled (Fig. 3.5A, arrowhead).

3.4 Discussion and Conclusions

We have demonstrated VIPR-SSFP to be an excellent NCE-MRA method for visualization of the transplant renal vein and renal artery. The VIPR-SSFP acquisition provided diagnostic-quality images of the renal vein over 80% of the time, while IFIR did not allow for assessment of this structure in any cases. However, IFIR provides improved visualization of the renal artery, likely due to its suppression of venous signal. Importantly, the average arterial quality score for VIPR-SSFP images was above the threshold for diagnostic adequacy – in fact, nearly 70% of the VIPR-SSFP exams were scored as providing high- or good-quality visualization of the renal artery. Diagnosis of



both RAS and venous stenosis was therefore possible in a majority of patients using VIPR-SSFP images alone.

VIPR-SSFP's linear combination method of fat suppression provided improved reduction of fat signal compared to the chemical saturation pulse used by IFIR. This is likely due to the sharp transition between the fat stopband and adjacent passband of VIPR-SSFP's spectral response. Due to the limited temporal duration of its chemical saturation pulse, IFIR's spectral response undergoes a relatively smooth transition between these regions compared to that of VIPR-SSFP; this results in preservation of a relatively larger amount of signal from off-resonance fat spins. Although VIPR-SSFP's linear combination fat saturation method could potentially be used with IFIR, Cartesian SSFP trajectories typically do not satisfy the short-TR constraint necessary to produce the spectral response required for fat suppression, and would therefore be incompatible.

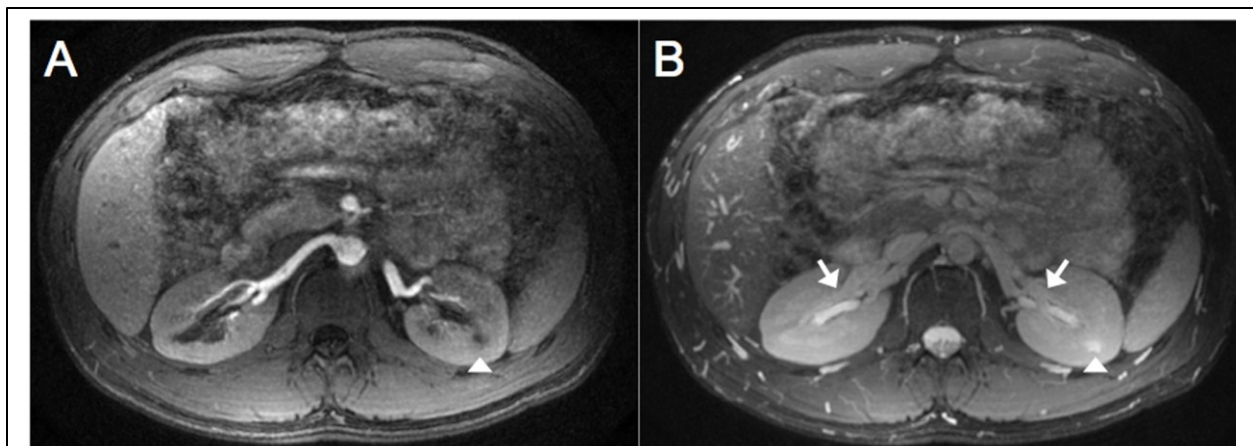


Figure 3.5: Thin-slab IFIR MIPs acquired with (A) and without (B) an inversion pulse depicting the renal vessels of a healthy volunteer. The renal arteries are clearly visible in (A), along with several segmental vessels of the right renal artery. In (B), the IVC as well as the renal veins (arrows) are visible, but the renal arteries have become more difficult to distinguish from surrounding renal veins and parenchyma. A renal cyst can also be seen in (B), which appears as an area of signal void in (A).

The two readers noted that the effect of residual subcutaneous fat signal on VIPR-SSFP image quality tended to be benign, while on IFIR images the presence of unsuppressed fat signal would frequently impair vessel visualization quality. This is because residual fat signal combined with uncompensated respiratory motion will generate ghost artifacts in the phase-encoding dimensions of Cartesian acquisitions such as IFIR. Radial acquisitions such as VIPR-SSFP, which lack a phase-encode dimension, are significantly less susceptible to motion-induced fat ghosting[69]. VIPR-SSFP's fat saturation method may thus be superior to the chemical saturation pulse used by IFIR when imaging individuals with significant subcutaneous adiposity.

VIPR-SSFP is clearly superior to IFIR in its ability to detect non-arterial and extrarenal vascular pathology due to the fact that it does not utilize an inversion pulse. Because VIPR-SSFP generates contrast in stationary tissue and fluid, it is useful for detection of transplant- and biopsy-related complications such as perinephric fluid collections, abscesses and pseudoaneurysms (Figure 3.3). When IFIR's inversion pulse is disabled, it also becomes capable of visualizing venous vessels and static fluid collections (Figure 3.5B, renal cyst). However, this comes at the expense of its arterial visualization quality – as seen in Fig. 3.5B, the segmental branches of the renal artery clearly visible in Fig. 3.5A are difficult to distinguish from the renal veins and surrounding renal parenchyma. It seems that while IFIR is capable of visualizing venous vessels and fluid collections when the inversion pulse is disabled, its arterial visualization quality – the sole metric where it was superior to VIPR-SSFP – must be sacrificed for it to do so.

A major limitation of this study is that none of the patients' VIPR-SSFP images depicted significant renal vein pathology. Although the readers were able to score the images based on their ability to visualize the transplant renal vein, in no case was a thrombus or stenosis noted. However, an incidental finding of external iliac vein thrombosis was made in one patient's VIPR-SSFP images (Figure 3.4), demonstrating the ability of this sequence to detect venous pathology. A second study limitation is that no patients were imaged within seven days following the transplant operation. It was therefore not possible to detect pathologies such as anastomotic pseudoaneurysm that tend to occur shortly after graft placement.

From a clinical standpoint, VIPR-SSFP appears to play a complementary role to existing NCE-MRA methods, due to its ability to generate contrast in both arterial and venous vessels as well as surrounding tissue. Inflow-based sequences such as Time-SLIP and IFIR will remain useful because in many cases, identification of RAS is the only indication for renal MRA, particularly in native kidneys. Although radiologists may prefer to use methods such as IFIR to generate high-quality MIP images of the renal artery, the diagnosis of RAS is always made from thin multiplanar reformatted (MPR) images where arterial-venous separation is less important. Grading of vascular stenosis should never be made from MIP images alone, as these are known to exaggerate the degree of stenosis significantly[70].

In conclusion, this study has demonstrated the VIPR-SSFP sequence to be efficacious in visualizing the renal transplant arterial and venous vessels. Given the benefits in venous visualization and fat suppression VIPR-SSFP provides over inflow-weighted Cartesian SSFP sequences, we expect it to be of considerable utility in our future NCE-MRA evaluations of renal transplant patients. However, at present it would seem to be prudent for transplant patients to be scanned with both inflow-weighted and non-inflow weighted NCE-MR sequences to achieve maximum arterial visualization quality with the former and to enable venous visualization with the latter. Future product NCE-MRA sequences would likely benefit from dual acquisitions (with and without an inversion pulse) to facilitate detection of the wide range of vascular pathologies that can occur in renal transplant patients.

Chapter 4: Dynamic Contrast-Enhanced MRI and Quantitative Perfusion Modeling in the Liver

4.1 Background I: Imaging-based measurement of tissue perfusion

4.1.1 Measurement of blood flow to the liver

Direct measurement of blood flow to the liver holds the potential to enhance understanding of normal hepatic physiology while also serving to elucidate the pathophysiology underlying many diseases that afflict this organ. The liver's vascular supply is distinct from most other organs in the body in that it receives about 20% of its blood from the hepatic artery and 80% of its blood from the portal vein. The absolute blood flow to the liver is highly variable, depending primarily upon whether an individual is in a fasting or post-prandial state – because the portal vein drains the majority of blood from the gut, blood flow to the liver increases substantially after consumption of a meal. In addition to physiological changes to flow, many disease states can alter both absolute flow and portal venous fractional flow (the fraction of blood received by a specific volume of liver tissue which derives from the portal vein versus the hepatic artery)[71]. These include chronic liver disease and cirrhosis, as well as many focal liver lesions such as hepatocellular carcinoma and colorectal cancer metastases[32, 72]. Understanding the normal range of hepatic perfusion, in addition to the ways in

which disease states may modify blood flow to this organ, is therefore of immense clinical importance.

4.1.2 Hepatic flow measurement using Doppler ultrasound

Historically, measurement of hepatic flow and perfusion using non-invasive medical imaging approaches has been quite difficult. Initial efforts have focused on measurement of flow through the hepatic artery and portal vein using Doppler ultrasound (US); results of such measurements have been reported numerous times in the literature[73]. However, volumetric flow rates measured with Doppler US are notoriously inaccurate – US makes measurements of blood **velocity**, not total blood flow, and its use in measuring flow suffers from significant operator dependence when determining the vessel cross-sectional area and vessel angle relative to the transducer[74, 75]. Moreover, Doppler US has limited tissue penetration depth, making it difficult to image the portal vein in patients with significant abdominal fat or ascites fluid. Finally, US is hampered by its inability to evaluate complex anatomic variations of the portal venous and hepatic arterial systems, which may occur both naturally and in disease (e.g. venous collaterals). As a result of these difficulties, the clinical use of US for evaluation of hepatic flow disturbances in disease is relatively limited. US is still used quite often for detection of focal hepatic masses, though interestingly its sensitivity for detection of cirrhosis is quite low (55%)[76].

4.1.3 Hepatic perfusion measurement using contrast-enhanced CT

Dynamic contrast-enhanced (DCE) CT imaging of the liver is often used clinically for detection and characterization of focal liver lesions. Upon injection of a contrast bolus into the antecubital vein, attenuation-enhancing contrast material will flow into the heart, and subsequently through the aorta to the hepatic artery and eventually the portal vein. This contrast-enhancement pattern – early enhancement of the hepatic artery followed by delayed enhancement of the portal vein – is used as the basis for diagnosis of focal liver lesions given the lesions' qualitative behavior compared to that of normal liver tissue during the first pass of contrast agent passage. Further, due to the direct (linear) relationship between CT signal and contrast concentration after subtraction of background signal, dynamic contrast-enhanced CT combined with pharmacokinetic modeling can also be used to quantitatively determine the amount of blood flow to the liver on a per-voxel basis.

Measurement of hepatic perfusion using quantitative DCE-CT imaging has been investigated thoroughly[77-79]. However, accurate and repeatable measurement of blood flow to the liver using DCE-CT has proven challenging for several reasons. Although multi-detector CT is capable of providing the volume coverage as well as high temporal and spatial resolution necessary to characterize the enhancement dynamics of focal liver lesions[79], the repeated scanning required to capture the first pass of contrast uptake exposes patients to a large amount of ionizing radiation. Additionally, liver motion during free breathing necessitates either manual registration of ROIs

between timeframes[80] or motion compensation, typically through serial breath holds[81]. As a result of these issues, quantitative hepatic DCE-CT imaging is infrequently performed clinically; in fact, even qualitative DCE-CT for diagnosis of liver lesions is rapidly being supplanted by radiation-free DCE-MR imaging. Nevertheless, because of the simple linear relationship between x-ray attenuation and contrast concentration in CT, a considerable amount of theoretical development has been pursued regarding the perfusion-related information that can be gleaned from time-attenuation curves during the first pass of contrast agent through the liver. Resultantly, hepatic perfusion measurement using DCE-CT imaging remains an active area of research.

4.1.4 Quantitative versus semiquantitative perfusion parameters

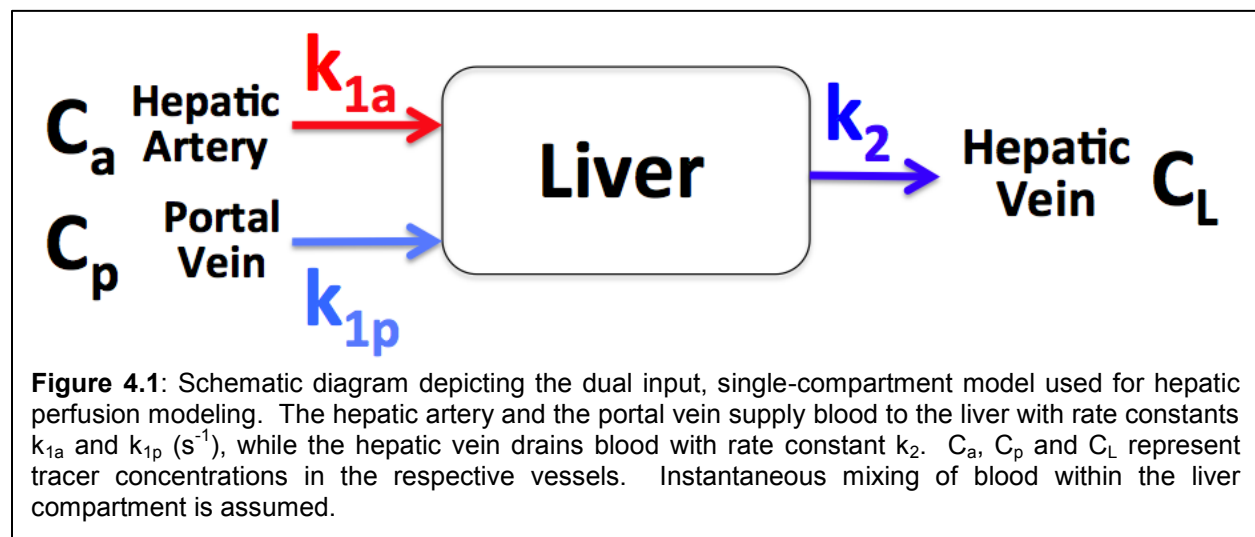
To date, two methods have been utilized to assess hepatic perfusion using dynamic contrast-enhanced CT imaging – the so-called semiquantitative method and the method of quantitative pharmacokinetic modeling. Briefly, semiquantitative methods rely on direct measurement of CT signal intensity both before and after contrast injection, and use the differences between these measurements to calculate several parameters representative of hepatic perfusion characteristics on a per-voxel basis[82, 83]. These parameters are referred to as semiquantitative because they provide only **relative** measures of blood flow and tissue perfusion, whereas pharmacokinetic modeling (indicator-dilution theory) purports to provide **exact** measures of these values; errors due to physiologic and stochastic noise notwithstanding. Characteristic examples of semiquantitative parameters are the contrast arrival time (i.e., the time at which the

contrast enhancement curve reaches its maximum slope) and the area under the contrast enhancement curve, which is a surrogate for the total blood flow to a voxel. Pharmacokinetic perfusion modeling uses the same time-attenuation data as semiquantitative methods, but employs a mathematical model that incorporates both the inputs to and output from the liver, as well as a transfer function describing the contrast agent's expected fate within the liver. From this model, mathematical parameters describing perfusion within the liver can be derived.

4.2 Background II: Pharmacokinetic modeling of hepatic contrast enhancement using indicator-dilution theory

4.2.1 The dual-input single-compartment model

Indicator-dilution theory[84], which describes the fate of small particles injected into the circulation, can be used to describe the behavior of CT and MR contrast agents as they enter and leave the liver. Although many different models for the liver have



been employed[85, 86], the most commonly used and thoroughly validated model[87] is the dual-input, single compartment model. This model assumes that there are two inputs to the liver – the hepatic artery and portal vein – as well as rapid, complete exchange (equilibration) of contrast agent between the hepatic sinusoids (vascular space) and the space of Disse (extravascular extracellular space, EES). The assumption of rapid exchange between vascular and extracellular compartments is essential to this model, as it allows the behavior of the hepatic tissue to be modeled using an impulse response function[88]. A visual depiction of this model can be seen in Figure 4.1 – the arterial and portal venous inputs to the liver are described by the rate constants k_{1a} and k_{1p} , respectively; while the venous outflow from the liver is described by the rate constant k_2 . The concentration of gadolinium contrast in these inputs is represented by the functions $C_a(t)$, $C_p(t)$ and $C_L(t)$. With knowledge of these rate constants as well as contrast concentrations, the total blood flow to the liver (or a region of interest within the liver) can be modeled with the differential equation:

$$\frac{dC_L(t)}{dt} = k_{1a}C_a(t - \tau_a) + k_{1p}C_p(t - \tau_p) - k_2C_L(t) \quad [4.1]$$

assuming transit times τ_a and τ_p of contrast agent between the hepatic artery / portal vein and the small branches of these vessels supplying hepatic parenchyma. This equation can be discretized solved exactly; its solution can be represented as a difference relation:

$$C_{n+1} = \frac{1}{k_2}(1 - e^{-k\Delta})[k_{1a}A_{n-\alpha} + k_{1p}P_{n-\beta}] + e^{-k\Delta}C_n \quad [4.2]$$

where A is the arterial concentration, P is the portal venous concentration, and Δ is the

sampling interval. Unfortunately, discretization of the solution is likely to represent the complex hemodynamics of the liver in an overly simplistic manner. The discrete solution implicitly assumes that the time constant of contrast exchange between the intravascular space and the EES is less than the sampling interval Δ . This interval is representative of the temporal footprint of the imaging modality used to acquire the liver perfusion data and is typically several seconds or more [38, 79]. However, it is quite possible that the exchange of contrast between intravascular and EES spaces takes place over several seconds or more; particularly in cirrhotic liver where collagen deposits may impair contrast molecule diffusion, and in tumors such as HCCs where contrast molecules may become trapped in disordered blood or lymphatic vessels. In order to more accurately represent the fate of contrast molecules during their passage through the liver, a more complex mathematical model is required.

If the solution to Equation 4.1 is recast as an integral equation:

$$C_L(t) = \int_0^t [k_{1a}C_a(t' - \tau_a) + k_{1p}C_p(t' - \tau_p)] R(t') dt' \quad [4.3]$$

a significant difference between this solution and the discrete solution becomes immediately apparent. The solution is now represented as a convolution between the arterial / portal venous inputs and a second function, $R(t)$. This function is known as the residue function, and describes the temporal behavior of contrast concentration within the liver as it passes through hepatic parenchyma. Importantly, the residue function can have arbitrary width in the temporal dimension, allowing for complex contrast uptake

behaviors to be modeled.

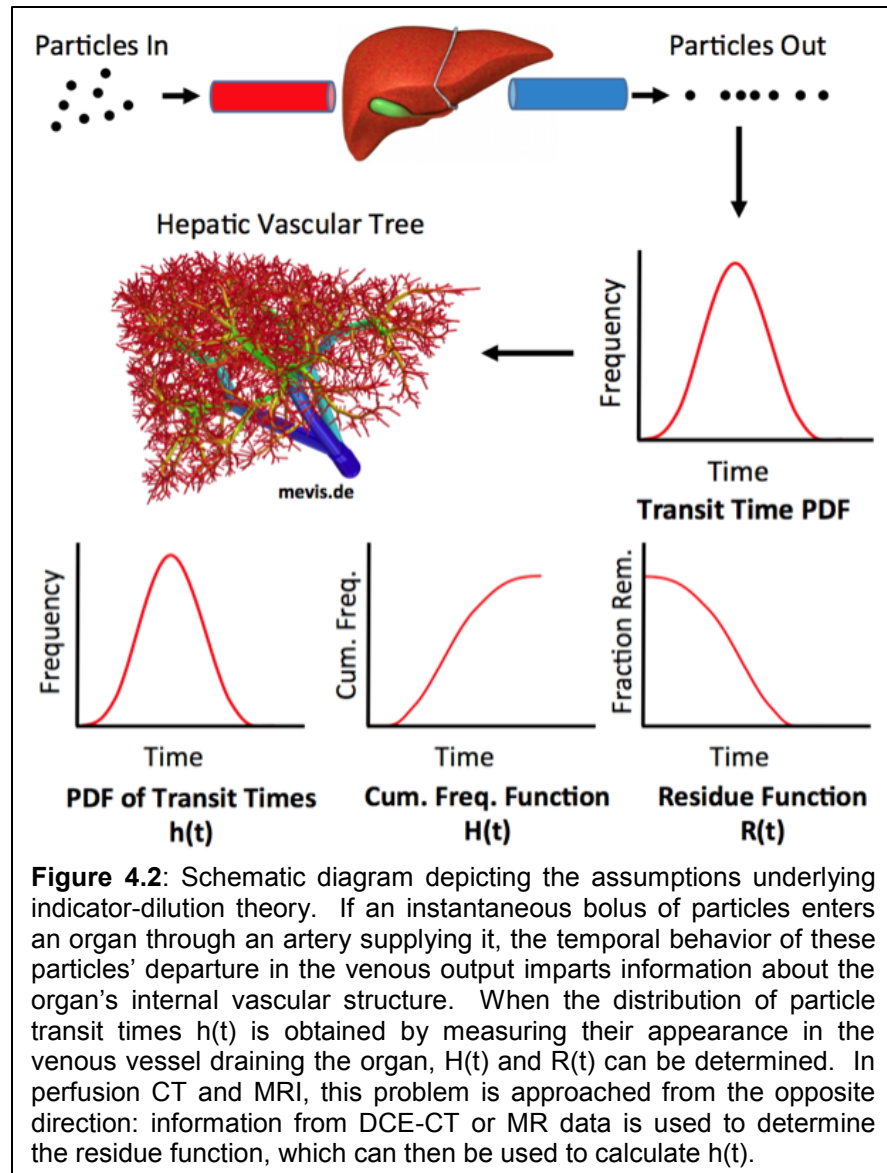
The concept of a residue function is based on the presumption that a contrast agent can be modeled as a series of particles traveling through a complex labyrinth of vessels within an organ. If the concentration of particles in an organ's vascular input is $C_{in}(t)$, then the concentration $C_{out}(t)$ at the vascular output of this organ can be mathematically represented as:

$$C_{out}(t) = C_{in}(t) \otimes h(t) \quad [4.4], \text{ or}$$

$$C_{out}(t) = \int_0^t C_{in}(\tau) \cdot h(t - \tau) d\tau \quad [4.5].$$

In these equations, $h(t)$ is a function describing the distribution of transit times of the particles through the tissue. Thus $h(t)$ is best thought of as a probability distribution function which defines the portion of an impulsive input (contrast) that will leave the organ between time t and $t + dt$. If C_{out} and C_{in} could be measured directly, then $h(t)$ would be relatively simple to determine through either deconvolution or a data-fitting procedure. Unfortunately, it is very difficult to measure the venous outflow of the liver due to instantaneous mixing of blood traveling through the inferior vena cava with hepatic venous output. Further, if perfusion analysis is performed on a voxelwise level, it becomes challenging to measure the venous output of tissue regions that are not obviously associated with major vessels. Thus, in order to determine the distribution of transit times $h(t)$ on either a voxelwise or whole-organ level, it is necessary to consider a different approach to this problem.

If the PDF $h(t)$ is integrated, its cumulative distribution function $H(t)$ is obtained. $H(t)$ is known as the cumulative frequency function, and describes the fraction of an impulsive input that has left a region of tissue by time t . $H(t)$ is also a quantity that cannot be observed through non-invasive imaging approaches.



However, the amount of contrast remaining within an organ or a region of tissue at time t is a quantity that can be measured by DCE-CT or DCE-MR approaches. This quantity – $1-H(t)$ – is defined as the residue function $R(t)$ of the tissue. Determination of this function is one of the main goals of quantitative pharmacokinetic modeling of tissue perfusion. The relationship between $h(t)$, $H(t)$ and $R(t)$ is depicted in Figure 4.2.

Although to this point quantitative perfusion modeling has been discussed from the perspective of determining whole-organ blood flow, one of the benefits of imaging-based perfusion methods is that the distribution of flow throughout the liver can be determined. Knowledge of regional blood flow within an organ is of considerably more clinical interest than simple measurement of total organ blood flow, as regions of increased perfusion (tumors) and regions of decreased perfusion (diseased/cirrhotic liver) can potentially be identified and associated with disease states. Thus, the above equations must be modified to reflect our interest in determining F_T , the blood flow through a unit volume of tissue (or tissular blood flow). The Stewart-Hamilton relation defines F_T as the ratio of the fractional dilution volume (the unit volume multiplied by the ratio $VD_T=V_D/V_T$, where V_D is the liver's volume of distribution available to the tracer and V_T is the organ's physical volume) to the mean transit time[89] of the unit tissue volume, or:

$$F_T = \frac{VD_T}{MTT}. \quad [4.6]$$

The mean transit time (MTT) is defined as the first moment of $h(t)$, and represents the average amount of time required by a contrast particle to transit the tissue. If V_D were known and were uniform over the entire organ, determination of the mean transit time at each voxel would be sufficient to calculate F_T . However, V_D is a quantity that can be variable throughout the liver's parenchyma, and may be significantly altered in disease states[90, 91].

If all relevant physiological variables are taken into account, the perfusion relationship in Eq. 4.1 can be rewritten as:

$$\frac{dC_T(t)}{dt} = E\rho(1 - Hct_{SV})[k_{1a}C_a(t - \tau_a) + k_{1p}C_p(t - \tau_p) - k_2 \frac{C_T(t)}{V_{D,T}}], \quad [4.7]$$

where the subscript T denotes that we are now considering a unit volume of liver tissue instead of the whole organ. E is defined as the extraction fraction of contrast from blood (usually assumed to be 100% [87]), ρ is the density of liver tissue (roughly 1 g/cm³), and Hct_{SV} is the small vessel hematocrit (roughly 0.25 in liver [92]). Using the concept of a residue function, and simplifying the arterial and portal venous inputs into the single input function $C_{in}(t)$, the solution to this equation can be written as:

$$C_{V_{D,T}}(t) = C_{in}(t) \otimes R_T(t), \quad [4.8]$$

where $C_{V_{D,T}}(t)$ is the contrast concentration within the volume of distribution of the unit tissue volume and $R_T(t)$ is the tissue residue function (TRF). If this quantity is rewritten with respect to $C_T(t)$, which is related to $C_{V_{D,T}}(t)$ as $C_T(t) = C_{V_{D,T}}(t) \cdot V_{D,T}$, the concentration of contrast within the tissue volume can be expressed as:

$$C_T(t) = C_{in}(t) \otimes R_T(t), \text{ where } R_T(t) = R(t) \cdot VD_T. \quad [4.9]$$

Once $R_T(t)$, the tissue residue function, has been determined, the distribution volume $V_{D,T}$ of the tracer can be calculated as the initial maximum value of $R_T(t)$, and the PDF of contrast particle transit times $h(t)$ can then be calculated as:

$$h(t) = -\frac{dR(t)}{dt}. \quad [4.10]$$

Using the assumption of the dual-input model that blood flow to a unit volume of liver tissue is derived from both the portal vein and the hepatic artery, the input function $C_{in}(t)$ (Eq. 4.9) is written as:

$$C_{in}(t) = \alpha C_{a(t)} + (1 - \alpha)C_p(t), \quad [4.11]$$

where α is defined as the hepatic arterial fraction of the input; $C_a(t)$ and $C_p(t)$ represent the hepatic arterial and portal venous inputs, respectively. The measured concentration-time curve for a unit tissue volume can now be simplified as:

$$C_T(t) = [\alpha C_{a(t)} + (1 - \alpha)C_p(t)] \otimes R_T(t). \quad [4.12]$$

Knowledge of $R_T(t)$ and α allows various perfusion parameters to be calculated for each unit tissue volume (i.e. each voxel), including the total hepatic blood flow, the hepatic perfusion index (portal venous fraction, $1-\alpha$), and the mean transit time of contrast agent through the tissue.

4.2.2 Determination of the tissue residue function

Although the mathematics underlying indicator-dilution theory is well defined, real-world implementation of this theory to determine perfusion parameters in the liver and other organs remains challenging. Because the measured parameter in DCE-CT imaging is $C_T(t)$, it is necessary to perform deconvolution in order to measure $R(t)$. Given the physiological noise (respiratory motion, cardiac motion, deformation of the liver) as well as the stochastic noise inherent to CT imaging, accurate determination of

the underlying tissular transfer function is nontrivial[93]. Additionally, as different regions of the liver may receive different fractions of hepatic arterial and portal venous input – especially in the case of focal liver lesions – an iterative approach to the deconvolution becomes necessary.

Many methods of deconvolution exist, but for the problem of perfusion imaging in the liver, it is important to consider constraints that can be placed upon the problem. Because the shape of $R(t)$ can be reasonably assumed to resemble a monotonically decreasing function, a family of functions with variable shape and time constants – the so-called Gamma variate functions – have often been used to approximate the tissue residue function[94]. Furthermore, it has been previously demonstrated that in the case of instantaneous mixing of contrast in a single compartment, the residue function takes the form of an exponential:

$$f(t) = a \cdot e^{-kt}. \quad [4.13]$$

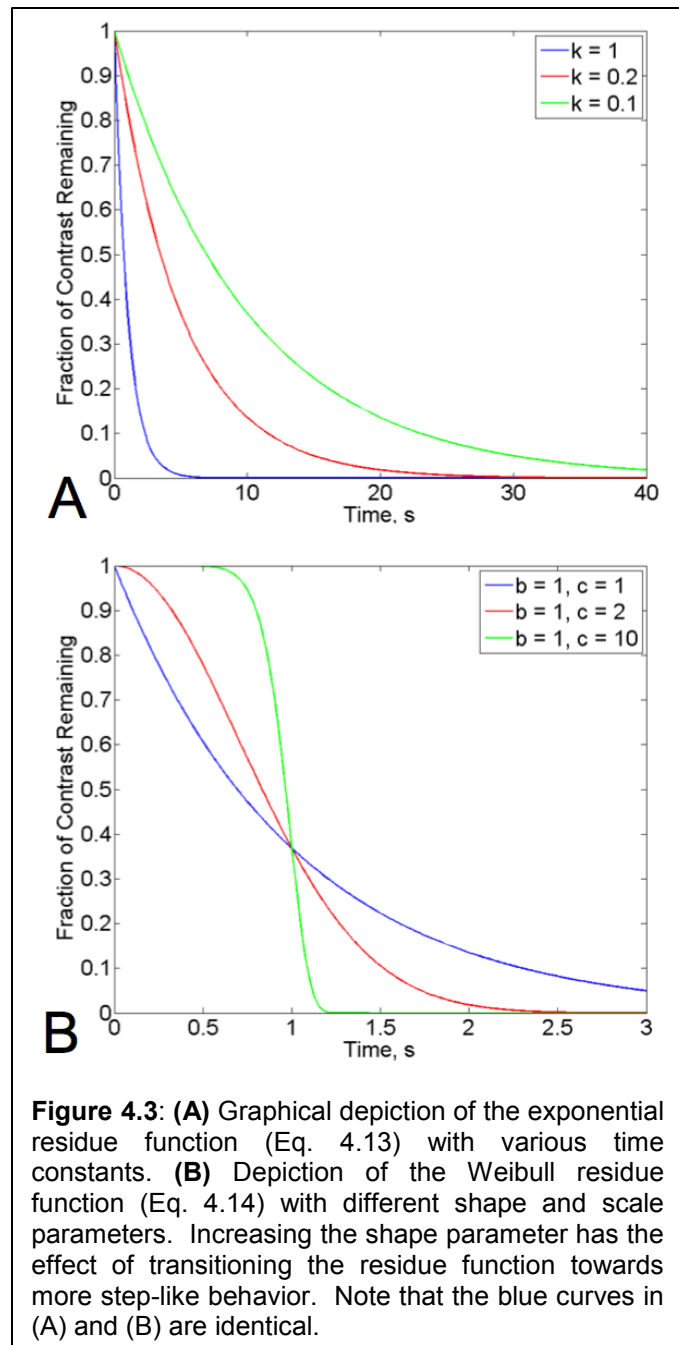
More recent work has utilized the family of Weibull functions to approximate $R(t)$ [88].

These functions take the form:

$$f(t) = a \cdot e^{-\left(\frac{t}{b}\right)^c}, \quad [4.14]$$

where a is a normalization constant, b is a scale parameter and c is a shape parameter. By adjusting the values of b and c , the Weibull function will take the form of a step function of varying width and smoothness (Figure 4.3).

By utilizing the exponential residue function in Eq. 4.13 or the Weibull residue function in Eq. 4.14, the deconvolution problem is reduced to a nonlinear fitting problem given knowledge of the hepatic arterial and portal venous input functions, which can typically be measured directly from CT or MR data. Direct determination of the residue function, though possible[93], would introduce several free parameters to the nonlinear fitting problem, which is already challenging in the context of physiologic noise as well as stochastic noise inherent to the imaging modality.



4.3 Background III: Hepatic perfusion measurement using contrast-enhanced MR imaging

4.3.1 Quantitative perfusion modeling using DCE-MRI: Challenges

Although indicator-dilution theory and pharmacokinetic modeling have been primarily applied to CT data for the purpose of determining hepatic perfusion parameters, these methods can also be employed using dynamic contrast-enhanced (DCE) MRI data to the same ends. MRI holds several advantages over CT, such as a lack of ionizing radiation and an ability to image over arbitrary volumes in arbitrary orientations. Initial experiences using gadolinium-based contrast agents in hepatic imaging demonstrated that their behavior was similar to that of CT contrast agents during their first pass through the liver[95, 96]. Further, these agents' behavior in focal liver lesions was also very similar to that of CT contrast agents given their restriction to the vascular and extravascular extracellular spaces. Thus, as MR technology has evolved and MR scanners have become available at greater numbers of hospitals, the use of T₁-weighted DCE-MRI for liver imaging has become increasingly common. However, liver DCE-MRI suffers from a number of issues which derive from fundamental limitations of MR technology itself.

First, the temporal resolution of MR imaging is fundamentally lower than that of CT imaging – whereas a CT scanner can in theory perfectly reconstruct an image

having acquired data from only a half-rotation of its gantry, an MR scanner must completely sample Fourier space to reconstruct an image with the desired matrix size. For detection of focal liver lesions, a matrix size of 1 cm or less is required; this often leads to scan times of 20s or more per frame even using modern imaging techniques[38]. As a result of this restriction on temporal resolution, many DCE-MRI acquisition protocols will restrict the field of view to a particular slab of the liver and acquire a small number of relatively thick slices[97]. Though this approach can provide the 3-4 sec temporal resolution necessary to visualize the temporal behavior of contrast passage through liver lesions, it negates one of MRI's major advantages over CT: the ability to acquire data volumes with isotropic resolution to enable whole-organ disease assessment and arbitrary image reformatting. Additionally, repeated imaging of thin slices will make the MR signal intensity susceptible to inflow effects[98], diminishing the utility of the data for perfusion quantification. Recent DCE-MRI protocols have begun to utilize 3D acquisitions with large excitation slabs for whole-liver perfusion assessment[91]; however, these acquisitions are still susceptible to inflow effects depending on the size and orientation of the excitation volume.

Although accelerated acquisitions with high spatial resolution and relatively small temporal footprints have been described in the literature[99,100], these acquisitions typically make use of parallel imaging methods to decrease data acquisition time, which compromises image SNR in accordance with the acceleration factor and the spatial arrangement of receiver coils (geometry factor[101]). Previous work by Materne, et al has demonstrated that quantitative perfusion parameters generated with the dual-input single-compartment model are very sensitive to noise, with signal measurement errors

on the order of 5% or greater resulting in poor estimation of these parameters in simulations[87]. Balancing the choice of acceleration factors to reduce temporal footprint with adequate spatial resolution to detect small lesions while retaining sufficient SNR to reliably estimate perfusion parameters is a challenging problem for hepatic DCE-MRI, as well as applications of pharmacokinetic modeling to other organ systems.

Second, the quantitative relationship between MR signal and gadolinium-based contrast agent contrast concentrations is complex. This relationship is typically reported as $\frac{1}{T_{1,eff}} = \frac{1}{T_{10}} + R_1[C]$, where R_1 denotes the relaxivity of the contrast agent used and C its blood concentration. In reality the relationship is typically dependent on parameters particular to each patient, scanner and pulse sequence; and may be nonlinear at high contrast concentrations (e.g. during the first pass of a contrast bolus through the aorta) due to T_2^* and susceptibility effects[102]. For SPGR-based (T_1 -weighted) sequences, the signal of each excitation is not entirely independent from the signal of the previous excitation unless a flip angle of 90° is used or radiofrequency spoiling is perfect[103]. In DCE-MRI, where the local T_1 changes quite rapidly with the passage of contrast agent, changes in the MR signal may therefore be delayed relative to changes in contrast concentration unless the TR of the imaging sequence is very short. Fortunately, most modern DCE-MR sequences use relatively short TRs, so this effect is typically not significant.

However, several more significant factors may confound the linear relationship of $[C]$ and T_1 . First, in areas of B_1 inhomogeneity such as the abdomen[104], different flip angles are experienced by different regions of tissue due to gradients in the dielectric

constant at air-tissue interfaces. This creates the potential to generate different signal values corresponding to identical contrast concentrations in different anatomic regions (e.g., near the dome of the liver vs. in the middle of the organ). Furthermore, because perfusion sequences typically utilize low flip angles to sensitivity to low contrast concentrations and to increase SNR, these sequences are relatively insensitive to high contrast concentrations[87]. As a result, accurate measurement of the contrast concentration during the bolus' first pass through the aorta and portal vein is difficult. Lastly, because it is difficult to perform true measurements of T_1 during the rapid first-pass of contrast agents, several methods have been developed to calibrate changes in MR signal to changes in T_1 [105, 106]. Unfortunately, these methods often make considerable assumptions regarding the behavior of contrast agents, and may be unreliable in the context of lesions that wash-in and wash-out very rapidly (such as HCCs). For the reasons cited above, it is very difficult to determine absolute contrast concentration in hepatic DCE-MRI using data based on either un-calibrated or calibrated MR signal. However, it is simple to determine relative contrast concentration in different regions of the liver using data from the same scan – hence why DCE-MR data have historically been used for qualitative radiological diagnosis of liver lesions [107] rather than quantitative perfusion modeling.

Finally, because MR image acquisition is inherently slower than CT, image quality degradation due to both respiratory and cardiac motion is a major problem. In a study of healthy volunteers, the liver demonstrated an SI translation range of 1.2 to 2.6 cm in accordance with diaphragmatic motion[108]. This work also noted that the liver

deforms non-rigidly during the respiratory cycle, with certain regions being displaced by up to 3 cm. Correction for respiratory motion using navigators[109] and attempts to minimize respiratory motion's effect on image quality using novel pulse sequences combined with view-ordered reconstructions [110] have been investigated previously. Unfortunately, hepatic motion correction using navigator-based approaches is limited by the single-point measurement of the liver-diaphragm interface that is acquired. Different points along this interface likely move different distances during the respiratory cycle due to non-rigid hepatic deformation. Moreover, the liver also moves in the A-P and L-R dimensions during free breathing, which are not corrected for using navigators. Motion correction through respiratory gating combined with view re-ordering initially seems promising; however, the temporal range in which views can be re-ordered is limited by the rapid contrast uptake of hepatic parenchyma and arterially-perfused lesions. Additionally, correction for residual motion that occurs during individual views remains difficult if not impossible. Several novel information-based registration methods[111] that can be used to register DCE-MR images have been described in the literature; however, these methods are relatively difficult to implement. Information-based non-rigid registration methods nevertheless remain an active topic of research. At present, the most successful motion compensation method has been the use of sequential breath holds during image acquisition[91]; however, this method requires manual identification of portal venous ROIs and some means of dealing with missing data during free-breathing if the DCE-MR data is to be used for quantitative perfusion modeling.

4.3.2 Semiquantitative perfusion modeling using DCE-MRI

Because of the challenges inherent to quantitative DCE-MRI, several investigators have attempted to utilize MR data to generate semiquantitative perfusion parameters similar to those described in Section 4.1.3. These include:

Contrast arrival time: Defined as the time at which the slope of the contrast uptake curve (i.e., the plot of MR signal versus time) is greatest.

Contrast peak time: The time at which the MR signal in an ROI reaches its maximum value.

Area under the curve: The integrated area under the contrast uptake curve for an ROI.

Although these parameters are relatively simple to calculate, they are also dependent on a number of variables including the delivery rate of the contrast bolus, the amount of contrast administered, patient heart rate, cardiac output, etc. The area under the curve parameter in particular is also dependent on the many variables that may affect MR signal. Nevertheless, these parameters are significantly simpler to calculate than the quantitative perfusion parameters, and are likely to be less dependent on SNR. Furthermore, these parameters are free from the assumptions inherent to quantitative perfusion modeling, including the shape of the tissue residue function. Whether these parameters are useful in differentiating between normal liver, diseased liver and focal liver lesions remains to be investigated.

4.3.3 Modern MR methods for measuring hepatic perfusion

The MR Labs at UW-Madison have recently developed a sequence called RT-VIPR that can be used for CE-MRI exams of the liver[39]. This sequence is based on VIPR-SPGR[112], but instead of acquiring one full echo per TR it acquires four half-echoes in order to maximize data collection efficiency. The utility of this sequence in providing contrast-enhanced, isotropic-resolution 3D radial acquisitions of the liver at 3T using a 32-channel phased-array coil has previously been demonstrated[113] – VIPR-ME was shown to significantly improve SNR performance versus Cartesian acquisitions while allowing for high spatial (1.6 mm^3) and temporal resolution (4 seconds, without view sharing between frames). However, 3D radial trajectories suffer from a number of issues that do not affect standard Cartesian sequences; for example, undersampling artifacts can significantly blur the anatomy of interest, while phase inconsistencies (which occur due to off-resonance effects) between the four echoes acquired during each TR can degrade image quality[37]. Fortunately, by controlling the degree of undersampling and by using gradient calibration methods[114] to ensure that signal from each radial line adds coherently, undersampling artifacts can be minimized. Additionally, phase inconsistencies between echoes can be reduced by weighting the data from the echoes, applying a point-by-point phase correction to the echoes, or by utilizing an iterative reconstruction[115].

In the next section, the utility of this high-resolution sequence in performing quantitative and semiquantitative perfusion MRI is investigated.

4.4 Quantitative and semiquantitative perfusion MRI in healthy volunteers and HCC patients

4.4.1 Background

Significant alterations in hepatic perfusion accompany the pathological changes of cirrhosis in addition to focal malignancies such as hepatocellular carcinoma (HCC) [32, 116]. In cirrhosis, repeated cycles of hepatocellular injury and scarring lead to progressive fibrosis of normal liver parenchyma. This increases resistance to hepatic perfusion, and results in a decreased ratio of portal venous to hepatic arterial flow[116]. Meanwhile, HCC are highly vascularized tumors that draw the majority of their blood supply from branches of the hepatic artery[5]. The neoangiogenic process characteristic to these lesions significantly reduces the fraction of blood flow received from the portal vein relative to normal liver.

Unfortunately, perfusion alterations in cirrhosis and HCC are difficult to assess using qualitative methods such as MR/CT imaging or liver biopsy. More accurate quantitative methods are needed to develop further insight into the relationship between hepatic perfusion changes and the spectrum of chronic liver disease from fibrosis to cirrhosis. Quantitative perfusion assessment has the potential to enable improved characterization of pre-malignant liver lesions such as hepatocellular dysplasia, and could also be used as a non-invasive biomarker to evaluate HCC treatment efficacy.

For example, multifocal and metastatic HCC are increasingly treated with sorafenib, an anti-angiogenic agent that has been shown to prolong overall survival in patients with advanced HCC[30]. Sorafenib is thought to act by disrupting neoangiogenesis of the arterial blood supply to these lesions. Unfortunately, quantification of sorafenib treatment response is challenging, since anti-angiogenic therapy may not cause tumor regression according to RECIST criteria[117]. Non-invasive quantification of blood flow to HCC holds promise as a means to evaluate sorafenib treatment response, and may enable targeting of therapy to those patients most likely to benefit.

Qualitative MRI methods – primarily multiphase dynamic contrast-enhanced MRI (DCE-MRI) – remain the most accurate means for detection and characterization of focal liver lesions including HCC[118]. Unfortunately, current implementations of multiphase DCE-MRI suffer from limited temporal resolution (12-20s / frame [119]) and an inability to consistently match acquisitions to the desired phases of enhancement. Recent advances in acquisition methods have resulted in several DCE-MRI sequences capable of acquiring whole liver volumes with high temporal and spatial fidelity[39, 99, 120]. These sequences provide sub-centimeter spatial resolution to aid the identification of nascent hypervascular masses, while reducing the per-frame temporal footprint to improve visualization of enhancement dynamics[121]. In addition to simplifying radiological diagnosis of HCC, the improved spatiotemporal resolution afforded by these sequences has direct application to hepatic perfusion modeling.

Perfusion modeling of hepatic DCE-MRI data has proven challenging due to high spatial and temporal resolution requirements as well as the need for high SNR[87]. Significant progress towards these requirements has been made in accordance with the acquisition methods described above, as well as novel approaches to image reconstruction[122]. However, artifacts from respiratory motion remain a major barrier to accurate determination of hepatic perfusion parameters. Correction for respiratory motion using navigators has been attempted[109]. Unfortunately, the liver undergoes non-rigid deformation during free-breathing[108]. For this reason, local measurement of diaphragm position is unreliable for whole-liver motion correction. Retrospective motion correction through view-ordering has also been previously investigated[110]. However, rapid wash-in and wash-out of contrast restricts the temporal range over which re-ordering is reliable. This limits the applicability of view-ordering methods in patients with hypervascular lesions such as HCC.

In this work, we formulate a novel approach to hepatic perfusion modeling designed to exclude motion-corrupted data acquired between sequential breath-holds. We subsequently utilize this method to determine whether an additional degree of freedom in the tissue residue function (TRF) improves fitting of the perfusion model to the raw data. Lastly, we perform a pilot study to evaluate the performance of resultant quantitative perfusion parameters – as well as two semi-quantitative measures of perfusion requiring less computational effort – for differentiating between normal liver, diseased (cirrhotic) liver and HCC.

4.4.2 Materials and Methods

Theory

For hepatic perfusion analysis, a dual-input single-compartment model of the liver was utilized[80]. This model accounts for the two vascular inputs to the liver (hepatic artery and portal vein). It assumes that contrast agent in the intravascular space (hepatic sinusoids) rapidly equilibrates with the extravascular extracellular space (EES, ie: Space of Disse). This model has previously been validated in animal studies acquired using radiolabeled microspheres[87]. Mathematically, the model is described by the equation:

$$\frac{dC_L(t)}{dt} = k_a[C_a(t - \tau_a)] + k_p[C_p(t - \tau_p)] - k_2C_L(t) \quad [4.15]$$

where $C_L(t)$, $C_a(t)$ and $C_p(t)$ represent contrast concentrations in a unit volume of liver parenchyma, hepatic artery and portal vein, respectively. k_a and k_p are the arterial and portal venous inflow rate constants (s^{-1}), while k_2 is the outflow rate constant from the liver compartment. τ_a and τ_p represent the transit times of contrast between the hepatic artery/portal vein and liver parenchyma.

Previous work has demonstrated that the values of τ_a of τ_p are small – typically 1-2s[86] – when ROIs are placed in the aorta and the portal vein near the liver hilum. This agrees with our observations that intrahepatic arterial and portal venous branches

enhance rapidly after contrast arrival. Fixed values for τ_a and τ_p were therefore utilized during modeling, which allows Eq. 4.15 to be simplified as:

$$\frac{dC_L(t)}{dt} = k_a C_{a-\tau_a}(t) + k_p C_{p-\tau_p}(t) - k_2 C_L(t) \quad [4.16].$$

Eq. 4.16 is typically rewritten as a convolution to account for the fact that the impulse response of the unit tissue volume (residue function) is not instantaneous, and cannot be modeled as delta function, ie:

$$C_L(t) = \left[k_a C_{a-\tau_a}(t) + k_p C_{p-\tau_p}(t) \right] \otimes R_L(t) \quad [4.17]$$

where $R_L(t)$ is the residue function of the unit volume, or tissue residue function (TRF). Previous theoretical work has demonstrated that $R_L(t)$ is well modeled as an exponential distribution ($e^{-k_2 t}$), provided that mixing between the vascular bed and EES compartment is rapid and complete [93]. This may be a reasonable approximation in a healthy liver that possesses wide endothelial fenestrae, allowing for rapid exchange of gadolinium contrast between the intravascular and EES compartments. However, the exponential model imposes significant constraint on the shape of the residue function. In diseased hepatic parenchyma, dysplastic lesions and HCC, the shape of the residue function likely deviates from an exponential distribution. By adding a single additional degree of freedom to the residue function and constraining it to the form of a Weibull distribution:

$$R(t) = e^{-\left(\frac{t}{a}\right)^b} \quad [4.18],$$

where a and b are scale and shape parameters, a variety of behaviors ranging from exponential decay to step-like decay can be modeled[88]. Permitting this range of shapes can be highly advantageous, as residue functions corresponding to diseased liver parenchyma and focal hepatic lesions are likely to differ significantly from normal liver.

Image Acquisition

All imaging was performed on a clinical 3.0T scanner (Discovery MR750, GE Healthcare; Waukesha, WI) using a 32-channel torso coil (Neocoil; Pewaukee, WI). A multi-echo 3D radial spoiled gradient-echo (SPGR) sequence was used to acquire data continuously for 3 minutes[39, 123]. A real-time display returned low-resolution images every second to permit breath-hold coordination with contrast arrival. Subjects were instructed to conduct a 10s pre-contrast breath-hold at mid-expiration, followed by intravenous injection of gadobenate dimeglumine (0.1mmol/kg at 2.0mL/s) followed by 30mL of saline chaser at the same injection rate. Subjects were subsequently instructed to perform three 20-25s breath-holds during the arterial, portal-venous and delayed phases of hepatic enhancement.

Specific scan parameters included: TR=2.7ms, TE=0.4/1.0/1.7ms, flip angle=12° to balance SNR performance with signal linearity[106], bandwidth=±250kHz, and a spherical 48cm FOV with 256³ matrix for 2.0mm³ isotropic true spatial resolution.

Images were reconstructed using an iterative SENSE algorithm[115] that reconstructed 180 timeframes every 1s with a 4s true temporal footprint. For scans performed after September 2011, two 3D-SPGR Cartesian acquisitions, one using the 32-channel and the other using the body coil were also performed to generate a coil sensitivity map. Scan parameters for the 3D-SPGR acquisitions included: TR/TE = 1.2/0.6 ms, flip angle=12°, BW = ±125 kHz, FOV = 48 x 48 x 40cm, and matrix = 256x256 with 1cm slice thickness. Scan time was 16s for each acquisition. Resultant coil sensitivity maps ($\frac{body}{coil}$) were interpolated onto coordinates of the radial acquisition.

For this IRB-approved HIPAA-compliant prospective study, 12 healthy volunteers and 9 subjects with hepatic cirrhosis and clinically confirmed history of HCC were imaged after obtaining informed consent between July 2009 and August 2012. One patient was scanned at three times points: one day before, and three days/two months after initiating sorafenib therapy. All subjects were instructed to fast for at least four hours before imaging per routine abdominal MRI protocol at our institution. This was also important to standardize and minimize the effects of meal related perfusion changes to the liver.

Post-processing

Breath-hold periods were retrospectively identified using data obtained from a respiratory bellows, or from the time-signal curve of the k -space origin[124] if bellows data were unavailable. It was assumed that hepatic motion was negligible during breath-hold periods[125]. To minimize the effect of shifts in liver position between

breath-holds, four time-averaged image volumes incorporating frames from pre-contrast, arterial, portal venous and delayed-phase breath-holds were generated and registered using the Insight Toolkit[126], implemented with rigid (affine) transformation and gradient descent using mutual information. The mutual information metric was chosen because of temporal changes in signal intensity resulting from the administration of contrast agent. Using the three transformation matrices obtained from these registrations, each frame from the arterial, portal venous and delayed phase breath-holds was subsequently registered to the initial (pre-contrast) breath-hold (Figure 4.4). Timeframes acquired during free-breathing were excluded from further analysis due to intra-frame motion corruption that could not be corrected through registration.

After registration, image volumes were weighted using the coil sensitivity map (available in 10 of 21 scans) to correct for non-uniform receiver sensitivity. To further reduce the effect of spatial signal inhomogeneity, signal values at each voxel were divided by their pre-contrast averages (S_0) to convert the data to enhancement ratios, ie: $\Delta S = \frac{S - S_0}{S_0} - 1$. For subsequent pharmacokinetic modeling, it was assumed that the relationship between enhancement ratio and contrast concentration was linear. This has been shown to be a reasonable approximation for the range of concentrations typically encountered in the liver[91].

Input Function Determination

To generate hepatic arterial and portal venous input functions, an aortic ROI roughly at the level of the celiac artery and a portal venous ROI at the liver hilum (each

1cm thick) were manually segmented using thresholding and morphologic erosion (Matlab; Mathworks, Natick, MA). The aortic ROI was positioned near the center of the excitation volume in order to minimize inflow effects. Time-signal curves for voxels in the aortic and PV ROIs were averaged to generate the arterial input function (AIF) and portal venous input function (PVIF). Because continuous input functions are required for pharmacokinetic modeling, the PVIF during free breathing periods was approximated using piecewise cubic interpolation. The aorta is retroperitoneal and does not move significantly during free breathing; motion corruption of the AIF was therefore negligible and interpolation was not required.

Perfusion Model Fitting

Using the series of registered image volumes, time-signal curves were generated for each voxel within the hepatic parenchyma after segmenting a large rectangular ROI containing the whole liver. Motion-corrupted data from free-breathing periods were excluded from further analysis, and only data acquired during breath-hold periods were used for perfusion model fitting.

Pharmacokinetic analysis using both exponential and Weibull tissue residue functions (TRFs) was performed for time-signal curves corresponding to voxels within the liver. Data were fitted to the perfusion model (Eq. 4.17) using a weighted iterative nonlinear least-squares minimization based on a trust-region reflective algorithm (lsqcurvefit; Matlab; Mathworks, Natick, MA). Weights were set so that only data

corresponding to breath-hold periods were utilized during fitting. No interpolation of time-signal curves in the tissue parenchyma was performed.

For each time-signal curve, the parameters k_a and k_p , as well as the shape/scale parameters a and b (Weibull TRF, Eq. 4.18) and the time constant k_2 (exponential TRF) were fit. To initiate the iterative calculation, values of k_a and k_p were first set to reflect the perfusion characteristics of normal liver (75% of perfusion from portal vein; 25% of perfusion from hepatic artery). The initial value of c was set to one so that the initial shape of both TRFs was identical.

Resultant best-fit values of k_a , k_p , a , b and k_2 were used to calculate four quantitative perfusion parameters:

1. total hepatic perfusion ($\frac{mL}{min \cdot 100 g}$, assuming a small vessel hematocrit of 0.25 [91, 92])
2. the arterial fraction = $k_a / (k_a + k_p)$
3. the contrast mean transit time (*MTT*)
4. the volume of distribution (V_D)

Voxel-wise parametric maps were generated for each exam to visualize the spatial distribution of these four parameters throughout the liver. Note that the portal venous fraction ($= k_p / (k_a + k_p) = 1 - \text{arterial fraction}$) can also be calculated, but for the sake of brevity will not be shown or discussed further.

Residue Function Comparison

To ascertain whether the Weibull TRF affords an improved fit to time-signal data compared to the exponential TRF, average time-signal curves from two 1cm^3 liver ROIs

(right and left lobes) and an HCC ROI (in tumor patients) were measured in all subjects. To assess the goodness-of-fit for each TRF, the total sum of squared residuals (SOS_{Res}) and the bias-corrected Akaike information criterion[127] (AIC) were calculated for both models. Lower values of SOS_{Res} and AIC indicate more accurate fitting.

Perfusion parameters corresponding to these ROIs were subsequently calculated for both models using the fitting procedure outlined above, and results from the right and left liver ROIs were averaged. Differences between the fitted parameters of each model corresponding to normal liver, cirrhotic liver and HCC were compared using Student's two-tailed t-test. Measurement errors for the ROI-averaged parameters were based on the variance of the distribution of voxel-wise parameters within the ROIs.

Semiquantitative Perfusion Parameters

Two semiquantitative perfusion parameters – contrast time-to-arrival (TTA) and arterial phase area under curve (AUC_{APh}) – were also calculated for voxels within the whole-liver ROI. These parameters are model-free relative indicators of tissue perfusion that may be less sensitive to noise than model-based quantitative perfusion parameters[128].

Time-to-arrival was defined as the time after aortic enhancement at which a voxel reaches 80% of its maximum signal. The aortic enhancement time was obtained by averaging TTAs within the aortic ROI. After calculating hepatic TTAs using this arrival criterion, voxels whose TTAs fell at the beginning or end of a breath-hold period were

identified. The time-signal data for each of these voxels were subsequently interpolated using cubic Hermite polynomials, and TTAs were re-calculated using the interpolated data.

Arterial-phase area-under-curve (AUC) was defined as the area under the time-signal curve during the arterial-phase breath-hold (AUC_{APh}). AUC_{APh} was determined by summing the signal at each voxel during the arterial phase breath-hold using the trapezoidal rule. By utilizing only timeframes from the arterial phase breath-hold when calculating AUCs, differences between normal liver and arterially perfused lesions are emphasized. Because of inter-patient variations in breath-hold length and cardiac output, AUC_{APh} values for each exam were normalized to the AUC of the aortic ROI averaged over the breath-hold period ($AUC_{APh} = AUC_{Voxel} / AUC_{Aorta}$).

Quantitative and Semiquantitative Perfusion Parameter Comparisons

Differences in quantitative and semi-quantitative perfusion parameters were investigated across the spectrum of hepatic disease represented in this study. Values of the quantitative perfusion parameters in ROIs corresponding to normal liver, cirrhotic liver and HCC were determined using both the exponential and Weibull TRF models. In the only patient with multifocal HCC lesions, perfusion parameters from three tumors of similar qualitative appearance were averaged to avoid biasing the study towards this patient. Resultant group-wise perfusion parameter estimates were then generated by averaging across all patients in the two study groups (healthy volunteers and cirrhotic patients) as well as all HCC lesions. Welch's test[129] was used to assess differences

in mean values of the perfusion parameters between the normal and cirrhotic groups; as well as between diseased liver and tumor within the cirrhotic group.

4.4.3 Results

Perfusion Modeling using Sequential Breath-Holds

The S-I translations required to register sequential 1s timeframes from the three post-injection breath-holds to the pre-contrast average (BH1_{AV}, Figure 4.4) in a normal volunteer are plotted in Figure 4.5. Within each breath-hold, variation in the magnitude of S-I translation required for registration is minor (sub-voxel). However, shifts of 2-3 voxels between breath-holds were typically required. These shifts are significant and were corrected with rigid registration. Significant translations (>1 voxel) in the A-P direction were also required for registration in some subjects. Corrections for translation in the L-R direction and rigid rotation were typically negligible, but could easily be corrected using this approach. Details of registration requirements within and between breath-holds have been described elsewhere[125].

In a small number of cases, rigid registration did not accurately align the portal venous ROI across the four sequential breath-holds. When this occurred, the transformation matrix was manually adjusted to ensure that the position of the portal vein was consistent with the location of the ROI.

Segmented aortic and portal venous ROIs from a healthy volunteer can be seen in Figures 4.6a and 4.6b, while Figure 4.6c shows the aortic and portal venous input

functions corresponding to these ROIs. This volunteer was instructed to conduct a single 60s breath-hold during the arterial and portal venous phases of enhancement, allowing a motion-free PVIF to be obtained over the entire interval. As can be seen in Fig. 4.6c, the AIF is a rapidly-changing function during the breath-hold interval which possesses an initial peak and a second peak corresponding to systemic re-circulation of contrast agent. However, as expected the PVIF changes more slowly and smoothly, reflecting contrast dilution and widening of the contrast bolus during transit through the capillary beds of the gut before arrival in the portal vein. An interpolated PVIF assuming 15s of missing data – roughly the duration of free breathing allowed between the arterial and portal venous phase breath-holds – can also be seen in Figure 4.6c. Because of the aforementioned characteristics of the PVIF, interpolation is shown to approximate the actual input function quite well over this interval.

Plots of the average time-signal curves of liver and HCC ROIs in a cirrhotic patient – as well as the result of fitting these data to the perfusion model in Eq. 4.17 – can be seen in Figure 4.7. Although there are gaps in the raw data due to free breathing, the fitted time-signal curves closely approximate these data during the breath-hold intervals. As expected, significant differences in liver and HCC ROI enhancement patterns exist during the arterial phase. Although the HCC ROI reaches peak signal (due to high arterial fraction) and starts to decline, the liver ROI only begins enhancing in the late arterial phase. The liver ROI presumably reaches peak signal between arterial and PV phase breath-holds, and starts to decline during the PV phase breath-hold.

Dual vs. Single Degree-of-Freedom Residue Functions

Figure 4.8 shows plots of the average time-signal curve corresponding to an HCC ROI in a second cirrhotic patient, with fitted time-signal curves generated using the exponential TRF (a) and Weibull TRF (b) overlaid. As can be seen in the plots, perfusion modeling using the Weibull TRF affords improved concordance between the fitted time-signal curve and the raw data. Quantitative quality-of-fit indicators including the bias-corrected Akaike information criterion (AIC) and sum-of-squares residuals (SOS_{Res}) are correspondingly improved. Figure 4.8c shows plots of the exponential and Weibull TRFs corresponding to the estimated time-signal curves in Figs. 4.8a/b. The shape of the residue functions is quite different: the Weibull TRF has adopted more step-like behavior compared to the exponential TRF. The extra degree of freedom available to the Weibull TRF has evidently resulted in a significantly different estimate of the underlying perfusion characteristics of the HCC ROI in this patient.

A comparison of quality-of-fit indicators and estimated perfusion parameters determined using exponential and Weibull TRFs in normal volunteers (healthy liver), patients (cirrhotic liver) and HCC can be seen in Table 4.1. The bias-corrected AIC, as well as the sum-of-squares residuals are considerably lower for the Weibull distribution compared to the exponential distribution in all groups. This indicates that perfusion modeling using the Weibull TRF affords improved correspondence to the raw data

despite the potential instability introduced by increasing the number of degrees-of-freedom.

With respect to perfusion parameter estimates, there is a statistically significant difference in the average mean transit time between the TRFs for healthy liver. This difference is marginally significant in cirrhotic liver and in HCC. There are also differences in total perfusion across the three groups, although significance is achieved only in healthy liver. Given these differences in addition to improved quality-of-fit indicators, it is possible that the Weibull TRF more accurately estimates quantitative perfusion parameters compared to the exponential TRF.

Quantitative and Semiquantitative Perfusion Modeling

Rapid changes during the time course of lesion enhancement in a patient with multifocal HCC are visualized in Figure 4.9. As can be seen in Fig. 4.9b, the HCC lesions quickly take up contrast, but become isointense with surrounding hepatic parenchyma at 15s (Fig. 4.9d) with subsequent washout during the portal venous phase (Fig. 4.9e).

Parametric maps of this patient's liver corresponding to perfusion, MTT, arterial fraction and V_D , as well as the two semiquantitative parametric maps of TTA and AUC_{APh} are shown in Figure 4.10. Both the quantitative perfusion and semiquantitative AUC_{APh} maps in Figs. 4.10a and 4.10b depict increased perfusion to regions coinciding with the tumors in Figs. 4.9b and 4.9c. The MTT and TTA maps in Figs. 4.10c and

4.10d also distinguish the tumors from surrounding normal parenchyma; the tumors are seen to have shorter MTTs and more rapid contrast times of arrival, respectively. The arterial fraction map in Fig. 4.10e demonstrates decreased portal flow to the HCC lesions, while the volume of distribution map in Fig. 4.10f does not depict significant differences in the V_D of lesions and normal liver.

Figures 4.11a-c show coronal reformats depicting the enhancement pattern of an HCC lesion in a second cirrhotic patient. At 35s after contrast injection, the lesion is visible as an enhancing region (arrowhead, Fig. 4.11a), which becomes isointense with surrounding liver parenchyma at 45s (Fig. 4.11b). However, during the portal venous phase the lesion exhibits washout and capsular enhancement (Fig. 4.11c), features known to be specific for HCC. Figures 4.11d-f show MTT, arterial fraction and TTA maps corresponding to the coronal reformats in Figs. 4.11a-c. The HCC lesion does not demonstrate significantly decreased MTT versus background liver, though the capsular rim shows increased MTT (Fig. 4.11d, black arrowhead). The arterial fraction of the HCC is significantly increased (Fig. 4.11e), and the TTA of this region is correspondingly reduced (Fig. 4.11f).

A comparison of quantitative and semiquantitative perfusion parameters between normal volunteers (healthy liver) and patients (cirrhotic liver) can be seen in Table 4.2a. Relative to volunteers, patients demonstrate decreased total perfusion, increased mean transit time, increased arterial fraction, and insignificant changes in volume of distribution. The increase in arterial fraction is marginally significant under both the

Weibull and exponential TRF models, while changes in perfusion and MTT are not significant. Nevertheless, there is considerable difference in the mean values of these parameters between the two groups, and these differences would likely achieve significance with a larger sample size. Of the semiquantitative parameters, TTA is significantly increased in the patients versus the healthy volunteers, while AUC_{APh} is not significantly different between the two groups.

Table 4.2b shows a comparison of estimated quantitative and semiquantitative perfusion parameters between cirrhotic liver and tumor (HCC) within the patient group. Average results from HCC in seven patients are reported due to difficulty in segmenting small satellite lesions in two patients whose primary lesions were treated with radiofrequency ablation. Statistically significant differences in MTT and arterial fraction are detected between cirrhotic liver and tumor using both the Weibull and exponential TRFs. These differences are consistent with tumors receiving primarily hepatic arterial perfusion. Large differences in total perfusion are also detected using both TRFs. These differences are marginally significant, due to considerable variance of the mean perfusion in the tumor group (possibly resulting from lesion heterogeneity). Both semiquantitative perfusion parameters demonstrate significant differences between cirrhotic liver and tumor, with more rapid arrival times and increased AUC_{APh} in the ROIs corresponding to tumors.

For the patient with metastatic HCC treated with sorafenib, plots depicting the effect of sorafenib on both semiquantitative and quantitative (Weibull TRF) perfusion

parameters corresponding to HCC are shown in Figure 4.12. In this patient, perfusion parameters of three HCC lesions were calculated and averaged for each scan (pre-drug; 3 days and 2 months post-drug). Figures 4.12a and 4.12b show the effect of therapy on total perfusion and AUC_{APh} . Sorafenib decreased perfusion in the lesions according to both the quantitative and semiquantitative indicators of blood flow. Figures 4.12c and 4.12d show the effect of sorafenib therapy on MTT and TTA; both the contrast arrival time and transit time of contrast through the HCC are increased. Figure 4.12e plots the arterial fraction, which decreased slightly after initiation of therapy; while Fig. 4.12f shows a plot of V_D , which is significantly decreased by sorafenib therapy.

4.4.4 Discussion and Conclusions

The purpose of this study was to formulate a method for hepatic perfusion modeling using interrupted data from sequential breath-holds, and to test its feasibility. Our results demonstrate that accurate modeling can be performed when data acquired during free-breathing is excluded from model fitting. By excluding this motion-corrupted data, quantitative perfusion parameters can be reliably estimated for sub-centimeter focal liver lesions such as HCC in addition to background liver parenchyma.

A second purpose of this work was to investigate whether the quantitative perfusion of normal and diseased liver can be more accurately modeled using a Weibull versus an exponential residue function. Our results show that in healthy liver, cirrhotic liver and tumor ROIs, the Weibull TRF provides a better fit of time-signal curves to the perfusion model. Our results also show that perfusion modeling using these TRFs

results in differing estimates of quantitative perfusion parameters, particularly the mean transit time. Importantly, these changes in perfusion parameter estimates are consistent with the Stewart-Hamilton relationship ($\text{flow} = V_D / \text{MTT}$). Given the improved fit to raw data afforded by the Weibull TRF, perfusion modeling using this residue function may generate estimates of hepatic perfusion parameters that are more accurate than those generated by the exponential TRF.

The final purpose of our work was to determine whether differences in quantitative perfusion parameters between healthy liver, diseased liver and HCC can be detected using this approach to perfusion modeling. Results from the comparison between volunteers and patients demonstrate that large differences in arterial fraction exist between normal and cirrhotic liver that approached statistical significance. This is consistent with the expected hepatic pathophysiology, as increased resistance to portal venous flow in cirrhotic liver is thought to increase the arterial fraction[130]. Results from the comparison between cirrhotic liver and HCC (Table 4.2b) show significant differences in MTT and arterial fraction, as well as a large mean difference in total perfusion that also approached significance. The decreased MTT and increased arterial fraction of these lesions are consistent with the known pathophysiology of HCC, whose blood supply is thought to consist primarily of parasitized hepatic arterial branches resulting from neoangiogenesis[131]. The difference in total perfusion did not achieve significance due to considerable tumor perfusion variation in different patients, possibly resulting from between-lesion heterogeneity.

Importantly, the semiquantitative perfusion parameters (TTA and AUC_{APh}) also demonstrated significant differences between diseased liver and HCC. The arrival time of contrast within HCC was more rapid compared to liver, as expected given their arterial blood supply. Moreover, AUC_{APh} was greater in HCC, indicating that the tumors received more perfusion than surrounding hepatic parenchyma during the arterial phase breath-hold. Although differences in AUC_{APh} between liver and HCC may be useful for identifying hypervascular lesions, it is likely this parameter is only useful as an indicator of relative perfusion within individual patients. Because AUC_{APh} can vary greatly depending on cardiac output, the transit time of contrast through the gut, and the length of the arterial phase breath-hold, it is not specific to intra-hepatic perfusion changes. This makes between-subject comparisons of AUC_{APh} challenging. TTA may be more useful for between-subjects comparisons as it has been normalized to the contrast arrival time in the aorta. However, because the TTA of liver is likely to vary with PV flow rate, this parameter may also be highly dependent on individual physiology.

Both quantitative and semiquantitative perfusion parameters demonstrated considerable changes in the patient undergoing treatment with sorafenib. Although the quantitative perfusion parameters exhibited alterations consistent with anti-angiogenic therapy (decreased perfusion, increased MTT) after three days, V_D was the only parameter to change considerably between the three-day and two-month time points. This is likely due to induction of necrosis within HCC lesions[117]. Interestingly, the semiquantitative perfusion parameters TTA and AUC_{APh} demonstrated large changes at both the three-day and two-month time points post-treatment. These parameters may

therefore be useful for detecting relative changes in HCC blood flow within patients shortly after initiation of anti-angiogenic therapy.

The use of a real-time acquisition was extremely helpful to ensure that arterial and portal venous input functions could be generated for the full duration of scanning. In addition, we discovered during post-processing that the effect of respiratory motion on the aorta's input function was negligible. This is due to a relative lack of motion in this vessel resulting from its location in the retroperitoneum. Further, the aorta also did not suffer from phase-ghosting caused by respiratory motion, likely due to our use of a 3D radial acquisition[69]. Thus, the AIF can be determined directly from DCE-MRI data without the need for interpolation.

However, the PVIF must be approximated during motion-corrupted gaps in the data. We found that it was possible to interpolate gaps in the PVIF because the PV uptake curve is very smooth and well-behaved. However, the accuracy of the PVIF estimate relies on capturing the peak of PV enhancement during the arterial phase breath-hold. If the peak is not acquired, interpolation will incorrectly approximate the PVIF during the intervening free-breathing period, resulting in significant error in estimated perfusion parameters. In this study, breath-hold coaching was initiated with the arrival of contrast in the right heart as visualized on a real-time low-resolution display. This allowed for the enhancement peaks of both the aorta and portal vein to be captured within breath-holds as short as 20s in all subjects.

The comparison performed in this study to assess the feasibility of detecting differences in perfusion parameters of normal liver, cirrhotic liver and HCC was limited by sample size. Nevertheless, statistically significant differences were detected between cirrhotic liver and HCC with respect to MTT and arterial fraction. Importantly, values of the quantitative perfusion parameters reported in this study generally agree with those previously reported in the literature[90, 91].

Further, the accuracy of the perfusion parameters may be limited by several factors. The most significant of these is the use of signal enhancement ratios for perfusion modeling versus direct measurement of T_1 values. This is necessary due to the difficulty of performing rapid, high-resolution T_1 mapping in the abdomen. Although it is possible to acquire high-resolution full-liver T_1 maps during a single breath-hold using advanced relaxometry methods[132], pre-contrast T_1 mapping alone is insufficient to calibrate the MR signal to the dynamic T_1 values which occur during contrast passage[133]. While bookend methods[105] may be a feasible means of improving T_1 calibration, the contrast uptake behavior of HCC lesions – which reach peak signal shortly after contrast injection – greatly limits their applicability, as arterial-phase signal in HCC would fall outside the bookend calibration range.

Several additional factors are likely to have influenced quantitative perfusion parameter accuracy. First, the MR signal saturates at high contrast concentrations – such as those occurring in the aorta during the first pass of a contrast bolus – when using fast, low flip angle T_1 -weighted sequences[87]. However, due to T_2^* and

susceptibility effects resulting from these high concentrations, it is unlikely that the signal-to- T_1 relationship of first-pass aortic blood would be linear even if a higher flip angle were used[102, 134]. Additionally, the reported measures of total hepatic perfusion are heavily dependent on the value of the small vessel hematocrit employed. This value determines the effective plasma fraction within the vascular compartments of the liver. Although the liver's small vessel hematocrit has been estimated previously[92], there may be variation between individuals. Moreover, because it has been shown that spins within RBCs can exchange with spins in plasma[135], the effective volume of the plasma compartment may be underestimated by the small vessel hematocrit, even if it is known exactly.

Lastly, our study is limited by the use of mutual information-based rigid registration. Although most of the shifts (translations) between breath-holds were corrected with registration, in 4/21 subjects the transformation matrices had to be manually adjusted to ensure that the PV ROI was appropriately situated over the vessel. Additionally, we did not account for non-rigid deformation of the liver during the respiratory cycle[108]. Small lesions in different regions of the liver may undergo motion during free-breathing that cannot be corrected through rigid registration methods. Fortunately, cirrhotic livers are very stiff, reducing hepatic deformation in comparison to normal liver. It is possible that non-rigid approaches to registration[111] may result in more accurate alignment of heterogeneously distributed HCC, but such approaches were not explored in this work.

Future work will focus on adding fat saturation to the acquisition by exploiting the different TEs of the four half-echoes to perform multipoint fat-water separation[136]. Additionally, the relationship between SNR and perfusion parameter accuracy will be investigated to determine the minimum uncertainty of parameter estimates that can be achieved at a given spatial and temporal resolution. This will allow for optimization of scan parameters for hepatic perfusion MRI, balancing spatiotemporal resolution requirements with SNR.

In conclusion, this study has demonstrated the feasibility of perfusion modeling using interrupted data from sequential breath-holds. We have also shown that modeling the tissue residue function using a Weibull distribution improves fitting of raw data and permits more accurate estimation of hepatic perfusion parameters. Finally, we have shown that our perfusion quantification method is sensitive to differences in blood flow between normal liver, cirrhotic liver and HCC. Our results are encouraging, and demonstrate that perfusion modeling may have clinical utility for measuring anti-angiogenic treatment response in HCC. This approach to perfusion modeling should be applicable to other MR or computed tomography (CT) acquisitions that utilize interrupted data in multiple sequential breath-holds. This approach may also be useful for characterizing other focal hepatic lesions including metastatic disease. Whether decreased perfusion after anti-angiogenic therapy correlates with improved survival in patients with HCC or other malignant lesions remains an important but unanswered question that warrants further investigation.

Table 4.1: Comparison of quality-of-fit indicators and quantitative perfusion parameters corresponding to Weibull and exponential residue functions.

	Volunteers (n = 12)			Patients (n = 9)			HCC (n = 7)		
	Exponential	Weibull	p	Exponential	Weibull	p	Exponential	Weibull	p
AIC	-303.38	-319.63		-267.17	-271.58		-203.39	-222.66	
SOS_{Res}	0.573	0.388		0.766	0.674		2.103	1.461	
Perfusion¹	213 ± 20	175 ± 53	0.02	165 ± 28	140 ± 51	0.32	473 ± 44	383 ± 62	0.13
MTT	12.3 ± 0.9 s	15.5 ± 4.2 s	0.01	14.8 ± 2.0 s	20.6 ± 4.1 s	0.07	7.8 ± 1.6 s	9.8 ± 3.5 s	0.09
Art. Frac.	14 ± 8%	15 ± 14%	0.56	37 ± 16%	39 ± 23%	0.33	77 ± 17%	73 ± 12%	0.16
V_D	30 ± 4%	31 ± 13%	0.63	29 ± 6%	31 ± 8%	0.46	27 ± 13%	28 ± 13%	0.28

¹ mL / min / 100 g

Table 4.2: (a) Comparison of quantitative perfusion parameters corresponding to hepatic parenchyma between healthy volunteers and cirrhotic patients. Results using both exponential and Weibull TRFs are shown. **(b)** Comparison of quantitative perfusion parameters between background (cirrhotic) hepatic parenchyma and HCC.

a

	Exponential TRF			Weibull TRF		
	Volunteers	Patients	p	Volunteers	Patients	p
Perfusion ¹	213 ± 20	165 ± 28	0.23	175 ± 53	140 ± 51	0.35
MTT	12.3 ± 0.9 s	14.8 ± 2.0 s	0.22	15.5 ± 4.2 s	20.6 ± 4.1 s	0.16
Art. Frac.	14 ± 8%	37 ± 16%	0.08	15 ± 14%	39 ± 23%	0.07
V _D	30 ± 4%	29 ± 6%	0.79	31 ± 13%	31 ± 8%	0.98
TTA	25.6 ± 4.2 s	37.7 ± 11.2 s	0.01			
AUC	0.13 ± 0.04	0.12 ± 0.05	0.90			

¹ mL / min / 100 g

b

	Exponential TRF			Weibull TRF		
	Liver	HCC	p	Liver	HCC	p
Perfusion ¹	165 ± 28	473 ± 44	0.08	140 ± 51	383 ± 62	0.09
MTT	14.8 ± 2.0 s	7.8 ± 1.6 s	0.01	20.6 ± 4.1 s	9.8 ± 3.5 s	0.01
Art. Frac.	37 ± 16%	77 ± 17%	0.03	39 ± 23%	73 ± 12%	0.04
V _D	29 ± 6%	27 ± 13%	0.80	31 ± 8%	28 ± 13%	0.71
TTA	37.7 ± 11.2 s	15.5 ± 6.1 s	<0.01			
AUC	0.12 ± 0.05	0.29 ± 0.11	0.02			

¹ mL / min / 100 g

Figure 4.4: Schematic representation of the acquisition and post-processing of DCE-MRI data for perfusion modeling. After contrast injection, a real-time display on the scanner console is used to coordinate breath-hold coaching with contrast arrival in the right heart. After scan completion, breath-holds are retrospectively identified, and average image volumes corresponding to arterial, PV and delayed phase breath-holds are generated. These breath-hold-averaged images are registered to the pre-contrast mask ($BH1_{Av}$), and the three resultant transformation matrices are used to register timeframes within each breath-hold to $BH1_{Av}$.

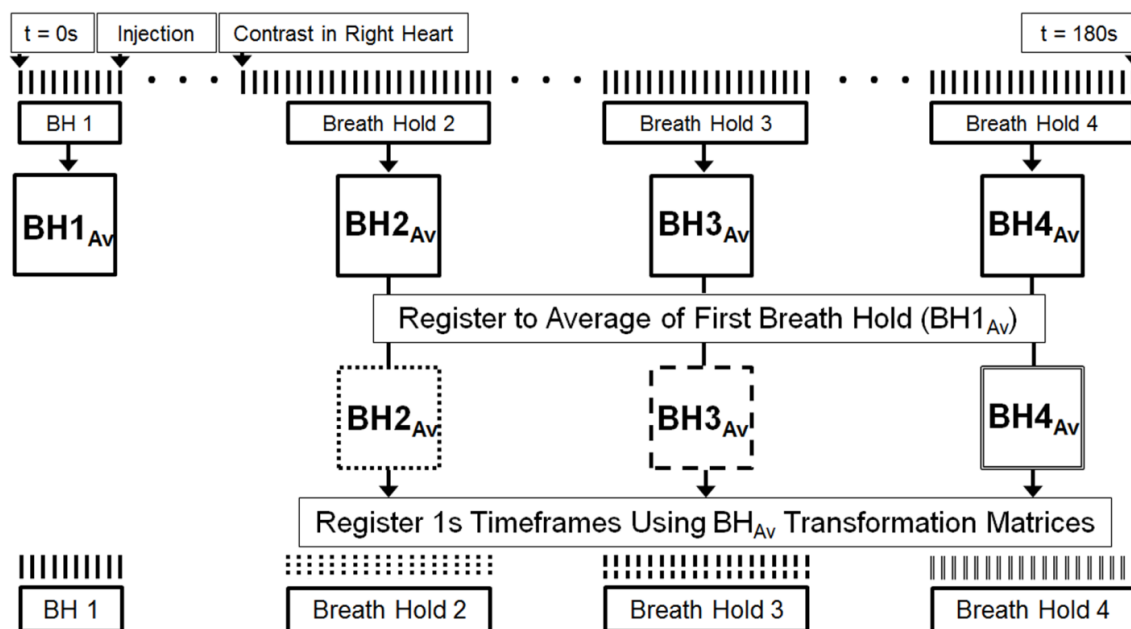


Figure 4.5: Rigid registration-derived correction in S-I translation during a breath-hold is insignificant (sub-voxel), while translations between breath-holds are significant and must be corrected. After registering each 1s frame from the three post-contrast breath-holds to the pre-contrast average, S-I translation magnitudes were determined and plotted for each frame. As seen in the plot, variations in S-I translation correction *within* a breath-hold are negligible, but *between* breath-holds are 2-3 voxels in magnitude. Shifts of 5 voxels (1cm) between breath-holds occurred in some patients.

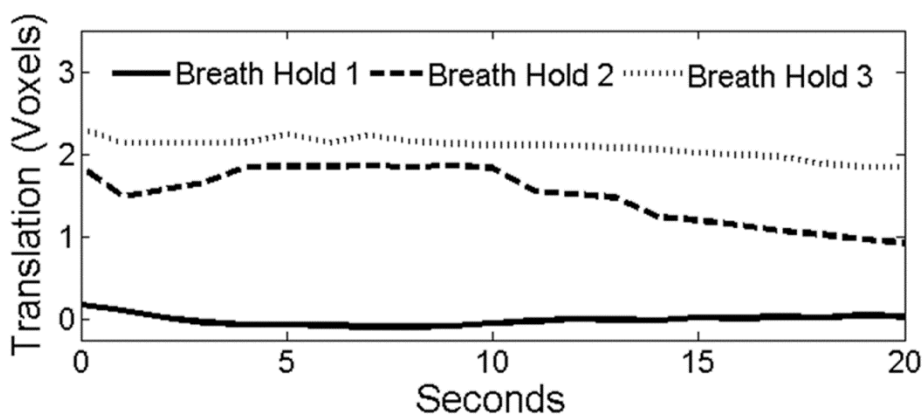


Figure 4.6: Interpolation of the PVIF during free-breathing accurately reproduces the input function during motion-corrupted gaps in DCE-MRI data. **(a and b)** Arterial-phase axial and sagittal images of a healthy volunteer show aortic and portal venous ROIs (dotted lines) appropriately situated in the respective vessels (arrowheads). **(c, left)** Time-signal curves corresponding to the aortic and portal venous ROIs in a volunteer who conducted a 55s breath-hold during the arterial and PV phases of hepatic enhancement. The PVIF is interpolated between the end of this breath-hold and the beginning of the subsequent breath-hold at 105s. **(c, right)** Time-signal curves of the actual PVIF and the interpolated PVIF calculated over a simulated free-breathing period (generated by excluding 15s of data between presumed arterial and PV phase breath-holds) are shown.

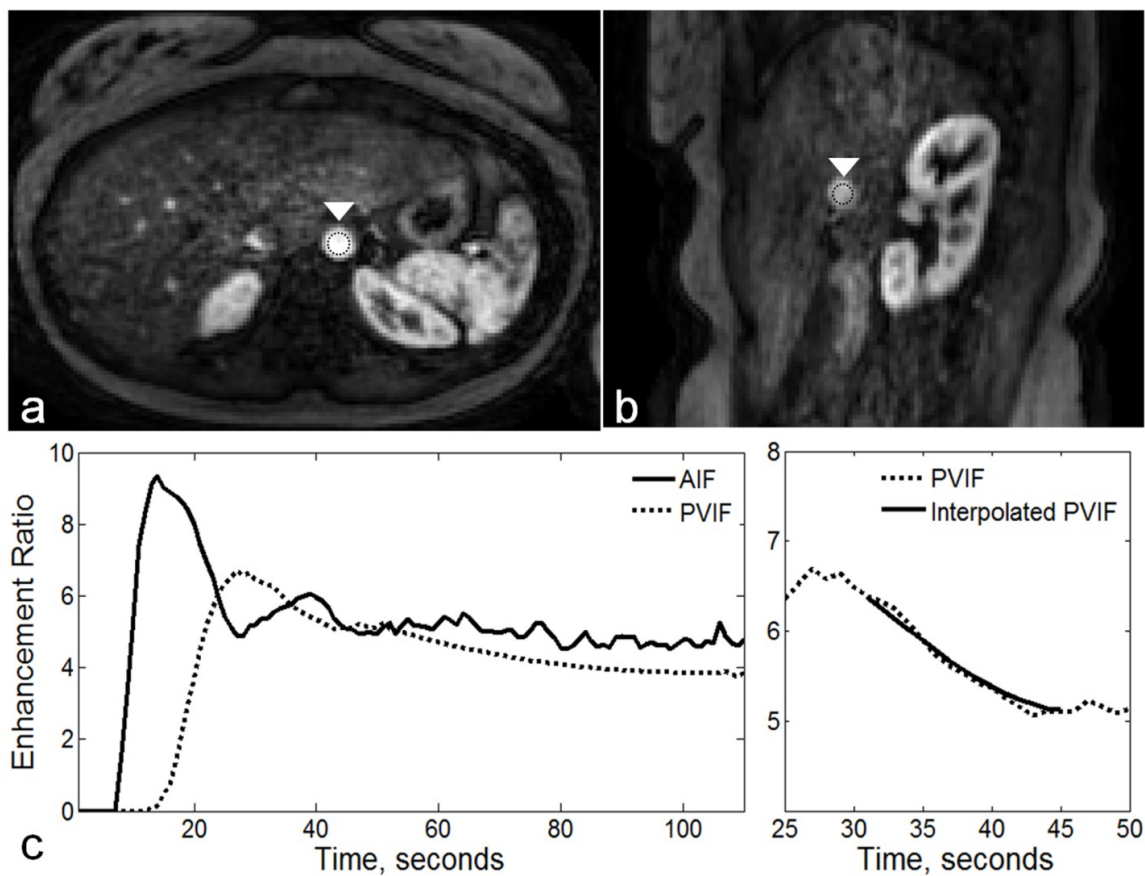


Figure 4.7: Excellent fitting of the quantitative perfusion model to raw data can be achieved even with gaps in the data during periods of free-breathing. An averaged time-signal curve in a liver ROI (points) is shown with fitted time-signal curve using the Weibull TRF overlaid. An average time-signal curve for an HCC ROI (triangles; fitted curve also overlaid) is shown for comparison. Note the early arrival of contrast in an HCC compared to adjacent liver parenchyma, as well as the relationship of these curves to the AIF (dashed line) and PVIF (dotted line). Also note that the PVIF reaches its peak before the end of the arterial phase breath-hold.

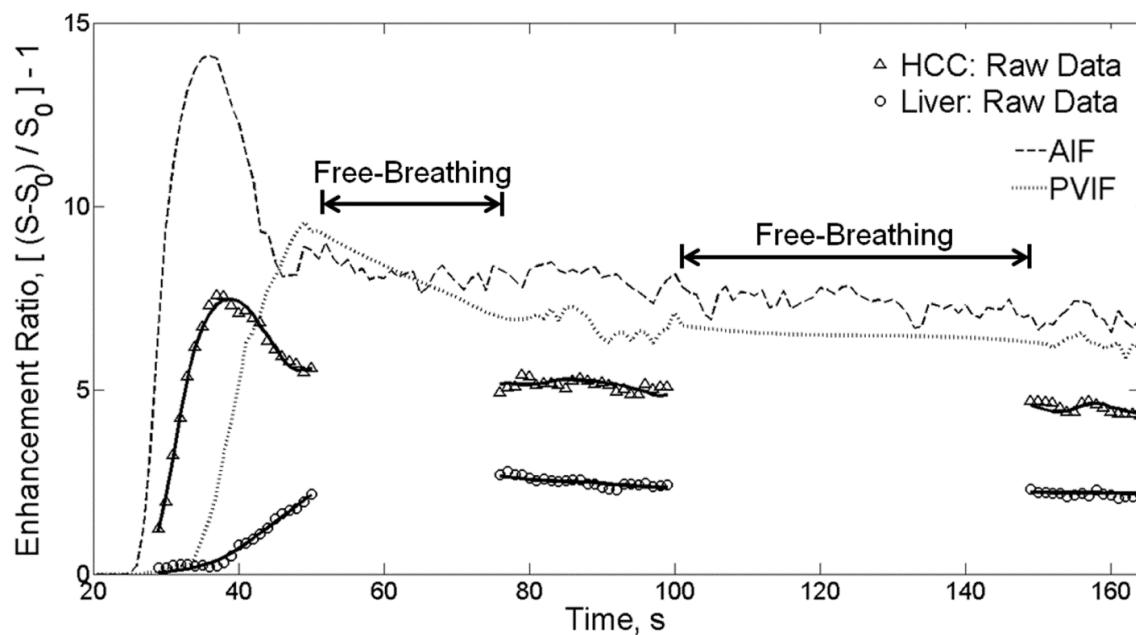


Figure 4.8: The Weibull TRF affords improved fit of the perfusion model to the raw data versus the exponential TRF. Fitted time-signal curves generated using **(a)** exponential and **(b)** Weibull TRFs overlaid on raw data demonstrate significant differences, with the Weibull model more closely approximating data on visual inspection. Quality-of-fit indicators AIC and SOS_{Res} are improved for the Weibull versus the exponential residue function. **(c)** Plots of the fitted Weibull and exponential residue functions. The Weibull TRF takes on a significantly different shape, and is more step-like in appearance.

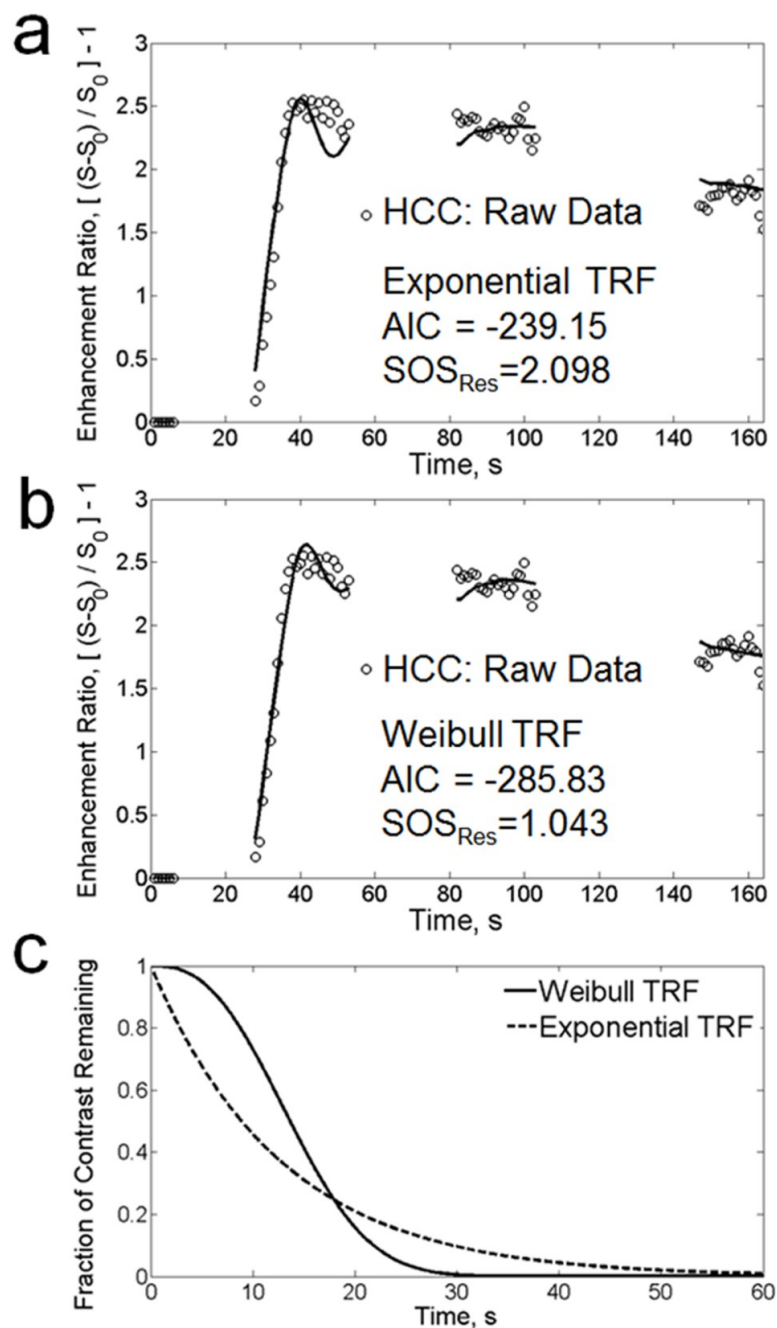


Figure 4.9: Temporal behavior of HCC lesions relative to normal liver during a DCE-MRI scan. Innumerable HCC lesions are not evident on the pre-contrast mask (a), but begin to enhance during the early arterial phase (b, **white arrow**). The lesions demonstrate obvious enhancement a few seconds later (c), but become difficult to distinguish from normal liver at the end of the arterial phase breath-hold (d). The lesions show washout during the portal venous phase breath-hold (e). Note that the arrow points to a single lesion on both axial and coronal reformats, demonstrating the isotropic spatial resolution of the radial acquisition.

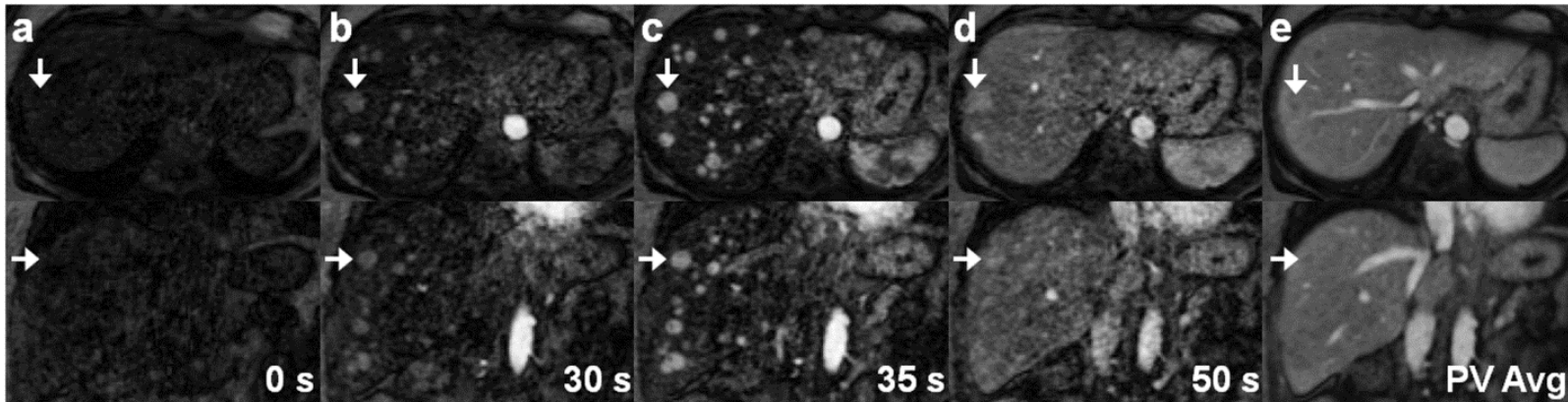


Figure 4.10: Whole-liver maps of quantitative and semiquantitative perfusion parameters depict significant differences between HCC and hepatic parenchyma. **(a and b)** Perfusion and AUC_{APh} maps show increased blood flow to HCC relative to normal liver. **(c and d)** MTT and TTA maps show decreased transit times and more rapid arrival times of contrast to HCC lesions, respectively. **(e)** An arterial fraction map shows significantly increased arterial perfusion within HCC. **(f)** The volume of distribution of HCC is not significantly different from that of surrounding liver tissue.

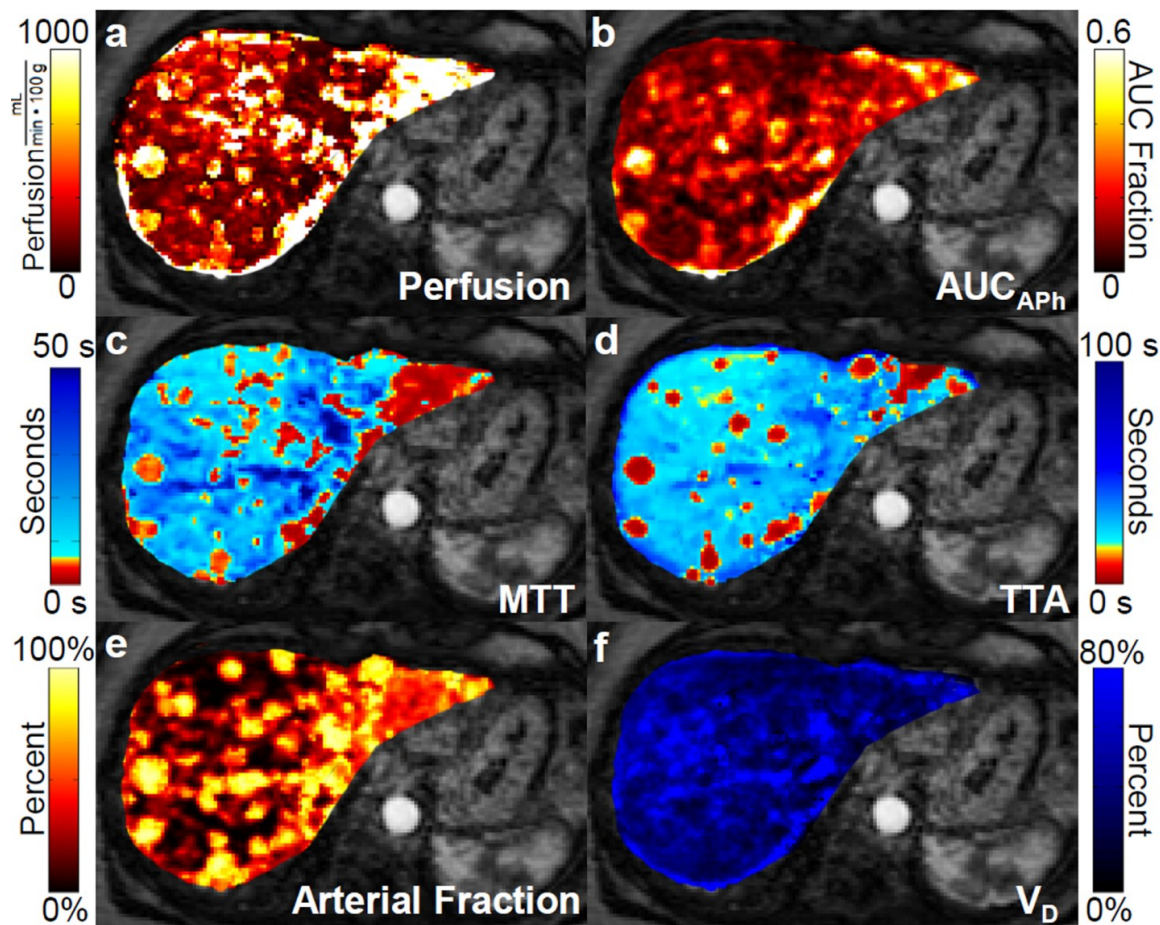


Figure 4.11: **(a-c)** Coronal reformats depicting progressive enhancement of an HCC lesion (arrowhead). The hepatic artery **(a)** and portal vein **(b)** can be seen (arrows). In **(c)**, washout and capsular enhancement are noted, features very specific for HCC. **(d-f)** Coronal reformats with overlaid MTT, arterial fraction and TTA parametric maps. The HCC does not show decreased MTT in this patient, but the tumor capsule shows slightly increased MTT relative to background liver **(d, arrowhead)**. The HCC does demonstrate increased arterial fraction **(e)** and decreased TTA **(f)**.

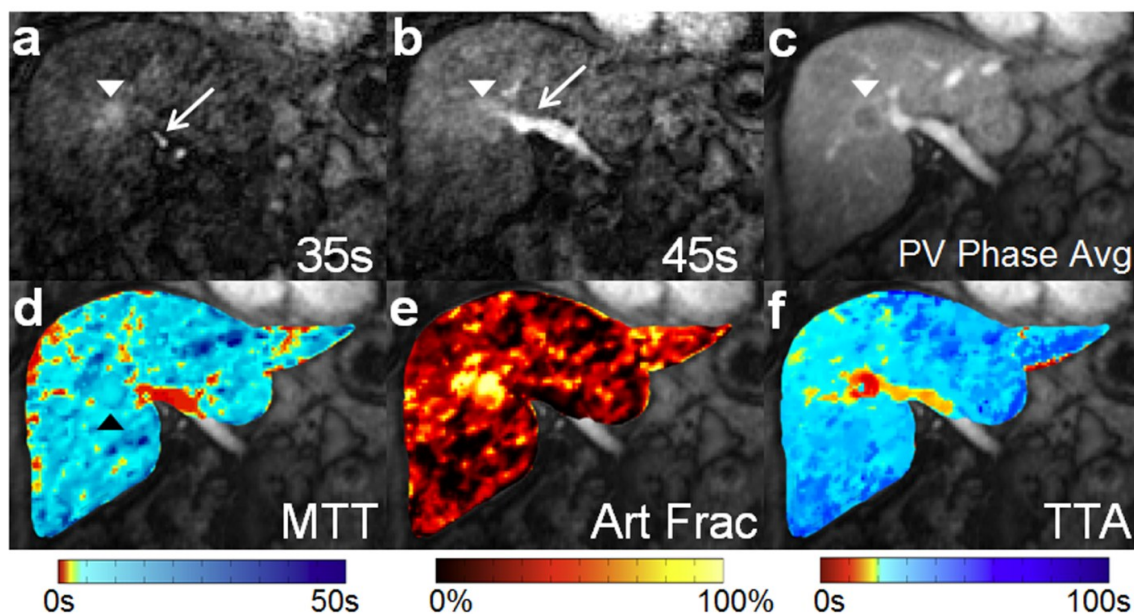
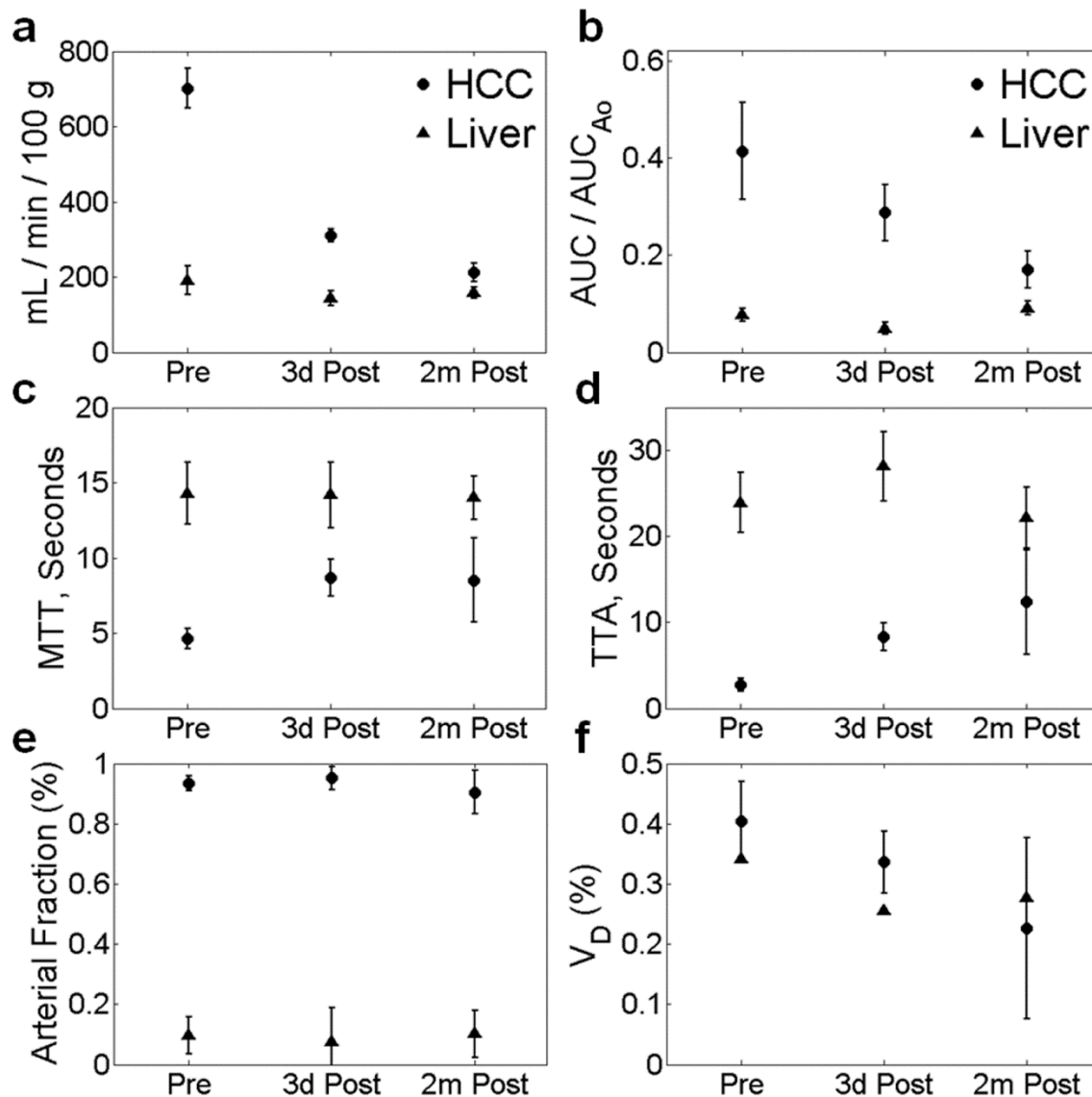


Figure 4.12: Quantitative and semiquantitative perfusion parameters corresponding to HCC lesions change in response to sorafenib therapy. **(a and b)** Plots of total perfusion and $AUC_{A_{Ph}}$ averaged over three HCC lesions in a patient before, three days after and two months after sorafenib treatment. Both the quantitative and semiquantitative parameters show decreased total perfusion. Normal liver is shown for comparison. **(c and d)** Plots of mean transit time and time-to-arrival show increased MTT and TTA in HCC lesions after sorafenib therapy. **(e)** HCC show somewhat increased arterial fraction and **(f)** significantly decreased V_D in response to sorafenib therapy. Error bars for the liver ROI are suppressed in (f).



Chapter 5: Summary and Future Work

5.1 Summary

The contribution of this dissertation may be summarized as follows:

Detection of Ethiodized Oil after TACE Treatment with IDEAL Imaging

Four patients were imaged after TACE-based treatment of focal hepatic lesions. These patients were imaged with IDEAL after completion of TACE therapy. Because the chemotherapeutic agents used during TACE are emulsified in ethiodized oil, it was plausible that the ethiodol distribution within the liver could be visualized using IDEAL imaging. Unfortunately, we have shown that this is not the case in all patients. Further experimentation focused on IDEAL imaging in a porcine model immediately after injection of an ethiodol bolus followed by embolizing microspheres. The purpose of this work was to determine whether ethiodol can be visualized in the short-term (15 minutes) after injection when its concentration is highest. Although a small amount of ethiodol could be seen on the IDEAL fat-only image, a significant amount of the substance was seen on CT. Evidently, IDEAL is not as sensitive as CT to the low concentrations of ethiodol which occur in the liver after injection of 10-20 mL of the substance during TACE. Despite the conflicting results of this work, it has been published as an ISMRM abstract[137].

Visualization of renal transplant vessels using VIPR-SSFP and Cartesian SSFP (IFIR)

Imaging of 21 renal transplant patients using the VIPR-SSFP sequence with comparison to a clinical gold standard method of NCE-MRA (IFIR) demonstrated that VIPR-SSFP affords significantly improved visualization of venous vessels as well as improved fat saturation. However, IFIR still provides better visualization of arterial vessels due to its use of an inversion pulse to null signal from static tissue. When IFIR's inversion pulse is disabled, it gains contrast in venous vessels and fluid collections similar to VIPR-SSFP, but the latter's improved fat-sat and robustness to motion make it an improved alternative to this variant of the IFIR sequence. This work has demonstrated that it is likely necessary to image renal transplant patients with both inflow-weighted (IFIR) and non-weighted (VIPR-SSFP) methods so that several important vascular pathologies can be visualized. A manuscript of this work has been prepared and is process of being re-submitted. This work has also been published as an ISMRM abstract[138].

Dynamic Contrast-Enhanced MRI and Quantitative Perfusion Modeling in the Liver

Dynamic contrast-enhanced MR imaging scans were performed in 12 healthy volunteers and 10 HCC patients using RT-VIPR. A method was developed to perform quantitative perfusion modeling using only DCE-MRI data acquired during sequential breath holds. Subsequent application of this method demonstrated that differences in quantitative and semiquantitative perfusion parameters exist between normal and

diseased liver; as well as between diseased liver and tumor. A manuscript of this work is currently in preparation. It has also been partially published as an ISMRM abstract[125].

5.2 Future Work

Detection of Ethiodized Oil after TACE Treatment with IDEAL Imaging

Although it was difficult to detect residual ethiodol after TACE treatment in several patients approximately 24h after the procedure was completed, small amounts of ethiodol were detected on IDEAL imaging in a porcine model immediately after ethiodol injection. It is possible that the IDEAL sequence is insensitive to the fat proton resonances of ethiodol because the IDEAL model is calibrated to detect subcutaneous fat. This hypothesis is corroborated by the work of Yin, et al. [53] who show that lipiodol can be detected in the liver of a rodent model using chemical shift-based fat-water imaging after calibrating this method to the ^1H NMR spectrum of the lipiodol. Future work in this area should focus on making similar modifications to IDEAL after measurement of the ^1H NMR spectrum of ethiodol. Unfortunately, because ethiodol has been discontinued by its manufacturer, further experiments utilizing this substance will be difficult to perform until its manufacturing is resumed.

Visualization of renal transplant vessels using VIPR-SSFP and Cartesian SSFP (IFIR)

Although VIPR-SSFP was demonstrated to be superior to IFIR with respect to venous visualization quality and quality of fat suppression, IFIR still afforded higher arterial visualization quality. The work presented in this thesis therefore indicates that comprehensive NCE-MRA exams of kidney transplant patients should involve use of both sequences so that a range of arterial and venous vascular pathology can be detected. Future work should focus on pursuing the clinical application of both of these methods for routine renal NCE-MRA; as well as the possible inclusion of a non-inflow-weighted variant of IFIR in the clinical protocol.

Dynamic Contrast-Enhanced MRI and Quantitative Perfusion Modeling in the Liver

The work presented in this dissertation has demonstrated the feasibility of quantitative perfusion modeling using data from hepatic DCE-MRI with gaps due to free-breathing. However, there are several potential avenues of advancement remaining in this field.

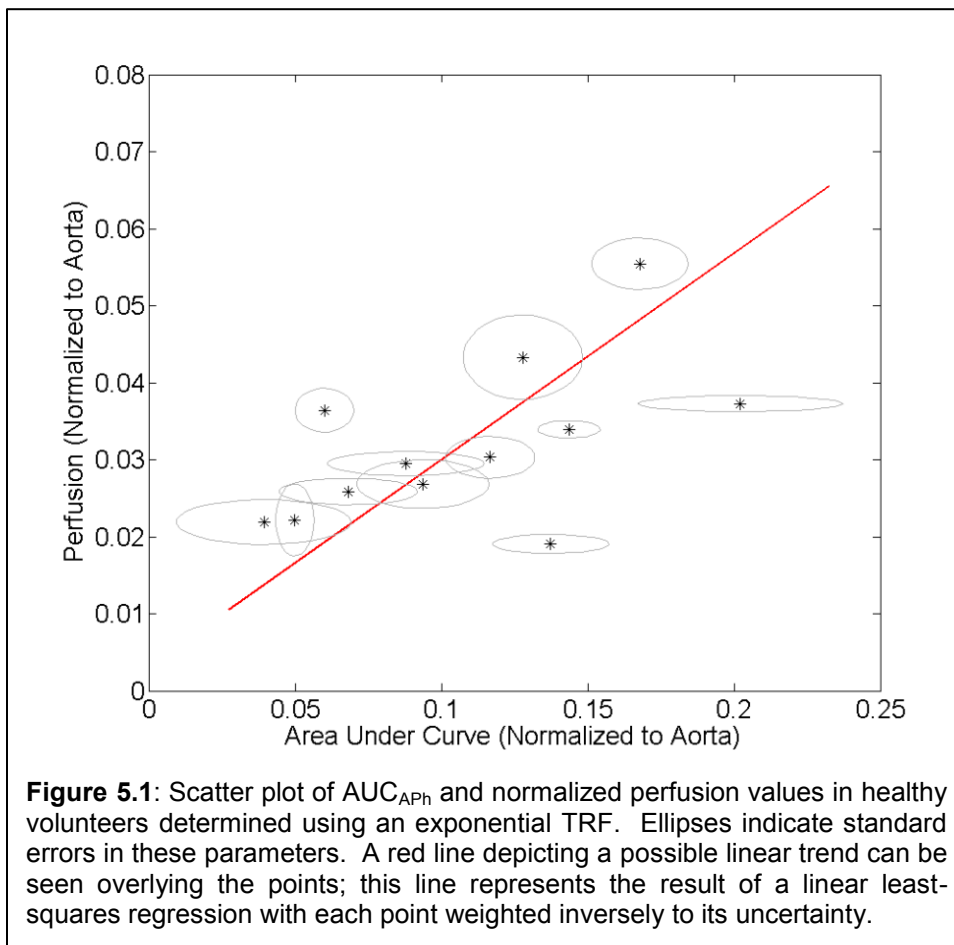
First, the rigid-body mutual-information-based registration method failed in several cases when registering image volumes from sequential breath holds. This required manual alignment of the image volumes to ensure that the portal venous ROI was consistent in all timeframes. It is possible that the MI-based registration failed because non-suppressed fat signal was heavily weighted in the registration process.

Additionally, because the liver deforms non-rigidly, application of a rigid registration process to hepatic DCE-MRI data is suboptimal. Future work should investigate the utility of non-rigid, information-based registration methods for registration of breath hold image volumes.

Next, the potential application of T_1 calibration methods and AIF correction methods to the RT-VIPR sequence should be investigated. If the spatial resolution of the acquisition is decreased, it may become possible to perform volumetric T_1 acquisitions before and after completion of the RT-VIPR scan; this would allow for application of the bookend method to effect T_1 calibration. Although signal within hypervascular lesions such as HCCs might fall outside of the bookend calibration range, this method will likely serve to generate a more linear relationship between MR signal and contrast concentration than that which exists for enhancement ratio-based data.

Finally, it may be valuable to perform rigorous investigation of the SNR properties of the RT-VIPR acquisition and the relationship of these properties to the confidence intervals of quantitative perfusion parameters. Additionally, determination of the Cramer-Rao bound for estimates of these parameters would serve to provide some indication of whether the parameters have the potential to become clinically valuable quantitative biomarkers given the magnitude of differences expected to exist between healthy and diseased liver.

Although relationships between the quantitative and semiquantitative parameters may exist – particularly AUC_{APh} and perfusion – these relationships are likely complex and may be dependent on each patient’s physiology as well as the timing of breath-holds during a particular exam. For example, if the arterial phase BH is delayed in one exam relative to another while all other parameters remain identical, the AUC_{APh} would increase due to measurement of later timeframes where contrast has entered the liver through the portal vein. Nevertheless, it is possible that simple relationships may exist if certain measures of standardization are taken (e.g., BH timing made is consistent between exams). An example depicting a possible linear relationship between AUC_{APh} and perfusion can be seen in Figure 5.1.



References

1. Kim WR, Brown RS, Terrault NA, El-Serag H: **Burden of liver disease in the United States: summary of a workshop.** In *Hepatology*. 2002, **36**:227–242.
2. Kochanek KD, Murphy SL, Anderson RN, Scott C: **Deaths: final data for 2002.** *Natl Vital Stat Rep* 2004, **53**:1–115.
3. Mathers CD, Lopez AD, Murray C: **The burden of disease and mortality by condition: data, methods, and results for 2001.** In *Global burden of disease and risk factors*. Oxford University Press and the World Bank; 2006:45–93.
4. Murray CJ, Lopez AD: **Alternative projections of mortality and disability by cause 1990-2020: Global Burden of Disease Study.** *Lancet* 1997, **349**:1498–1504.
5. Farazi PA, DePinho RA: **Hepatocellular carcinoma pathogenesis: from genes to environment.** *Nat Rev Cancer* 2006, **6**:674–687.
6. Davis GL, Albright JE, Cook SF, Rosenberg DM: **Projecting future complications of chronic hepatitis C in the United States.** *Liver Transpl.* 2003, **9**:331–338.
7. Francque SMA, Verrijken A, Mertens I, Hubens G, Van Marck E, Pelckmans P, Michielsen P, Van Gaal L: **Noninvasive assessment of nonalcoholic Fatty liver disease in obese or overweight patients.** *Clin. Gastroenterol. Hepatol.* 2012, **10**:1162–1168.
8. Yin M, Talwalkar JA, Glaser KJ, Manduca A, Grimm RC, Rossman PJ, Fidler JL, Ehman RL: **Assessment of Hepatic Fibrosis With Magnetic Resonance Elastography.** *Clinical Gastroenterology and Hepatology* 2007, **5**:1207–1213.e2.
9. Yin M, Woollard J, Wang X, Torres VE, Harris PC, Ward CJ, Glaser KJ, Manduca A, Ehman RL: **Quantitative assessment of hepatic fibrosis in an animal model with magnetic resonance elastography.** *Magn Reson Med* 2007, **58**:346–353.
10. Talwalkar JA: **Antifibrotic therapies—emerging biomarkers as treatment end points.** *Nat Rev Gastroenterol Hepatol* 2010, **7**:59–61.
11. Albanis E, Friedman SL: **Antifibrotic agents for liver disease.** *American Journal of transplantation* 2005.
12. Bataller R, Brenner DA: **Liver fibrosis.** *J. Clin. Invest.* 2005, **115**:209–218.
13. Bhathal PS, Grossman HJ: **Reduction of the increased portal vascular resistance of the isolated perfused cirrhotic rat liver by vasodilators.** *J. Hepatol.* 1985, **1**:325–337.
14. Schiff ER, Sorrell MF, Maddrey WC: **Portal Hypertension and Nonsurgical**

- Management.** In *Schiff's Diseases of the Liver*. 10th edition. Lippincott Williams and Wilkins; 2006, 1:419–483.
15. Boyer TD, Wright TL, Manns MP: **Hepatic fibrosis and cirrhosis.** In *Zakim and Boyer's Hepatology: A Textbook of Liver Disease*. 5th edition. Elsevier; 2006, 1:87–109.
16. Zipprich A, Steudel N, Behrmann C, Meiss F, Sziegoleit U, Fleig WE, Kleber G: **Functional significance of hepatic arterial flow reserve in patients with cirrhosis.** *Hepatology* 2003, **37**:385–392.
17. Silva MF, Wigg AJ: **Current controversies surrounding liver transplantation for hepatocellular carcinoma.** *J. Gastroenterol. Hepatol.* 2010, **25**:1217–1226.
18. Angeli P, Merkel C: **Pathogenesis and management of hepatorenal syndrome in patients with cirrhosis.** *J. Hepatol.* 2008, **48**:S93–S103.
19. Paramesh AS, Roayaie S, Doan Y, Schwartz ME, Emre S, Fishbein T, Florman S, Gondolesi GE, Krieger N, Ames S, Bromberg JS, Akalin E: **Post-liver transplant acute renal failure: factors predicting development of end-stage renal disease.** *Clin Transplant* 2004, **18**:94–99.
20. El-Serag HB: **Hepatocellular carcinoma.** *N. Engl. J. Med.* 2011, **365**:1118–1127.
21. Bartolomeo N, Trerotoli P, Serio G: **Progression of liver cirrhosis to HCC: an application of hidden Markov model.** *BMC Med Res Methodol* 2011, **11**:38.
22. Katyal SS, Oliver JHJ, Peterson MSM, Ferris JVJ, Carr BSB, Baron RLR: **Extrahepatic metastases of hepatocellular carcinoma.** *Radiology* 2000, **216**:698–703.
23. Bruix J, Sherman M, American Association for the Study of Liver Diseases: **Management of hepatocellular carcinoma: an update.** *Hepatology* 2011, **53**:1020–1022.
24. Colli A, Fraquelli M, Casazza G, Massironi S, Colucci A, Conte D, Duca P: **Accuracy of ultrasonography, spiral CT, magnetic resonance, and alpha-fetoprotein in diagnosing hepatocellular carcinoma: a systematic review.** *Am. J. Gastroenterol.* 2006, **101**:513–523.
25. Kamath PS, Wiesner RH, Malinchoc M, Kremers W, Therneau TM, Kosberg CL, D'Amico G, Dickson ER, Kim WR: **A model to predict survival in patients with end-stage liver disease.** *Hepatology* 2001, **33**:464–470.
26. de Lope CR, Tremosini S, Forner A, Reig M, Bruix J: **Management of HCC.** *J. Hepatol.* 2012, **56 Suppl 1**:S75–87.
27. Livraghi T, Meloni F, Di Stasi M, Rolle E, Solbiati L, Tinelli C, Rossi S: **Sustained complete response and complications rates after radiofrequency ablation of very**

- early hepatocellular carcinoma in cirrhosis: Is resection still the treatment of choice?** *Hepatology* 2008, **47**:82–89.
28. Lin DY, Liaw YF, Lee TY, Lai CM: **Hepatic arterial embolization in patients with unresectable hepatocellular carcinoma--a randomized controlled trial.** *Gastroenterology* 1988, **94**:453–456.
29. Llovet JM, Bruix J: **Systematic review of randomized trials for unresectable hepatocellular carcinoma: Chemoembolization improves survival.** *Hepatology* 2003, **37**:429–442.
30. Llovet JM, Ricci S, Mazzaferro V, Hilgard P, Gane E, Blanc J-F, de Oliveira AC, Santoro A, Raoul J-L, Forner A, Schwartz M, Porta C, Zeuzem S, Bolondi L, Greten TF, Galle PR, Seitz J-F, Borbath I, Häussinger D, Giannaris T, Shan M, Moscovici M, Voliotis D, Bruix J, SHARP Investigators Study Group: **Sorafenib in advanced hepatocellular carcinoma.** *N. Engl. J. Med.* 2008, **359**:378–390.
31. Xie B, Wang DH, Spechler SJ: **Sorafenib for treatment of hepatocellular carcinoma: a systematic review.** *Dig. Dis. Sci.* 2012, **57**:1122–1129.
32. Willatt JM, Hussain HK, Adusumilli S, Marrero JA: **MR Imaging of hepatocellular carcinoma in the cirrhotic liver: challenges and controversies.** *Radiology* 2008, **247**:311–330.
33. Choi BY, Nguyen MH: **The diagnosis and management of benign hepatic tumors.** *J. Clin. Gastroenterol.* 2005, **39**:401–412.
34. Lopez RR, Pan SH, Lois JF, McMonigle ME, Hoffman AL, Sher LS, Lugo D, Makowka L: **Transarterial chemoembolization is a safe treatment for unresectable hepatic malignancies.** *Am Surg* 1997, **63**:923–926.
35. Mazhar SM, Shieh-morteza M, Kohl CA, Middleton MS, Sirlin CB: **Nephrogenic systemic fibrosis in liver disease: a systematic review.** *J. Magn. Reson. Imaging* 2009, **30**:1313–1322.
36. Platt J, Ellis J, Rubin J: **Intrarenal arterial Doppler sonography in the detection of renal vein thrombosis of the native kidney.** *American Journal of Roentgenology* 1994, **162**:1367.
37. Klaers J, Jashnani Y, Jung Y, Brodsky E, Jacobson J, Kijowski R, Block WF: **Dual half-echo phase correction for implementation of 3D radial SSFP at 3.0 T.** *Magn Reson Med* 2010, **63**:282–289.
38. Goshima S, Kanematsu M, Kondo H, Shiratori Y, Onozuka M, Moriyama N, Bae KT: **Optimal Acquisition Delay for Dynamic Contrast-Enhanced MRI of Hypervascular Hepatocellular Carcinoma.** *American Journal of Roentgenology* 2009, **192**:686–692.
39. Brodsky E, Isaacs D, Grist TM, Block WF: **3D fluoroscopy with real-time 3D non-**

cartesian phased-array contrast-enhanced MRA. *Magn Reson Med* 2006, **56**:247–254.

40. Vogl TJ, Balzer JO, Mack MG, Bett G, Oppelt A: **Hybrid MR interventional imaging system: combined MR and angiography suites with single interactive table. Feasibility study in vascular liver tumor procedures.** *Eur Radiol* 2002, **12**:1394–1400.

41. Reeder SB, Wen Z, Yu H, Pineda AR, Gold GE, Markl M, Pelc NJ: **Multicoil Dixon chemical species separation with an iterative least-squares estimation method.** *Magn Reson Med* 2004, **51**:35–45.

42. Yu H, McKenzie CA, Shimakawa A, Vu AT, Brau ACS, J BP, Pineda AR, Brittain JH, Reeder SB: **Multiecho reconstruction for simultaneous water-fat decomposition and T2* estimation.** *J. Magn. Reson. Imaging* 2007, **26**:1153–1161.

43. Liu C-Y, McKenzie CA, Yu H, Brittain JH, Reeder SB: **Fat quantification with IDEAL gradient echo imaging: correction of bias from T(1) and noise.** *Magn Reson Med* 2007, **58**:354–364.

44. Ramsey DE, Kernagis LY, Soulen MC, Geschwind J-FH: **Chemoembolization of Hepatocellular Carcinoma.** *Journal of Vascular and Interventional Radiology* 2002, **13**:S211–S221.

45. Kónya A, Stephens LC, Wright KC: **Pure ethiodized oil as a capillary embolic agent with and without ethanol-ethiodol mixture in the rabbit kidney: embolic efficacy and temporal histopathologic findings.** *J Vasc Interv Radiol* 2010, **21**:1091–1099.

46. Reeder SB, McKenzie CA, Pineda AR, Yu H, Shimakawa A, Brau AC, Hargreaves BA, Gold GE, Brittain JH: **Water-fat separation with IDEAL gradient-echo imaging.** *J. Magn. Reson. Imaging* 2007, **25**:644–652.

47. Beatty P, Brau AC, Chang S, Joshi SM, Michelich CR, Bayram E, Nelson TE, Herfkens RJ, Brittain JH: **A Method for Autocalibrating 2-D Accelerated Volumetric Parallel Imaging with Clinically Practical Reconstruction Times.** In *Proceedings of the 15th Annual Meeting of ISMRM.* 2007.

48. Yu H, Reeder SB, Shimakawa A, Brittain JH, Pelc NJ: **Field map estimation with a region growing scheme for iterative 3-point water-fat decomposition.** *Magn Reson Med* 2005, **54**:1032–1039.

49. Prasad SR, Wang H, Rosas H, Menias CO, Narra VR, Middleton WD, Heiken JP: **Fat-containing lesions of the liver: radiologic-pathologic correlation.** *Radiographics* 2005, **25**:321–331.

50. Clavien P, Breitenstein S: *Malignant Liver Tumors: Current and Emerging Therapies.* John Wiley and Sons; 2009.

51. Ivancev K, Lunderquist A, Isaksson A, Hochbergs P, Wretlind A: **Clinical trials with a new iodinated lipid emulsion for computed tomography of the liver.** *Acta Radiol* 1989, **30**:449–457.
52. Shimamura Y, Gunvèn P, Takenaka Y, Shimizu H, Shima Y, Akimoto H, Arima K, Takahashi A, Kitaya T, Matsuyama T: **Combined peripheral and central chemoembolization of liver tumors. Experience with lipiodol-doxorubicin and gelatin sponge (L-TAE).** *Cancer* 1988, **61**:238–242.
53. Yin X, Guo Y, Li W, Huo E, Zhang Z, Nicolai J, Kleps RA, Hernando D, Katsaggelos AK, Omary RA, Larson AC: **Chemical shift MR imaging methods for the quantification of transcatheter lipiodol delivery to the liver: preclinical feasibility studies in a rodent model.** *Radiology* 2012, **263**:714–722.
54. Zhang H, Maki JH, Prince MR: **3D contrast-enhanced MR angiography.** *J. Magn. Reson. Imaging* 2007, **25**:13–25.
55. Jain R, Sawhney S: **Contrast-enhanced MR angiography (CE-MRA) in the evaluation of vascular complications of renal transplantation.** *Clinical Radiology* 2005, **60**:1171–1181.
56. Vasbinder GBC, Nelemans PJ, Kessels AGH, Kroon AA, de Leeuw PW, van Engelsehoven JMA: **Diagnostic Tests for Renal Artery Stenosis in Patients Suspected of Having Renovascular Hypertension.** *Annals of Internal Medicine* 2001, **135**:401–411.
57. Sadowski EA, Bennett LK, Chan MR, Wentland AL, Garrett AL, Garrett RW, Djamali A: **Nephrogenic Systemic Fibrosis: Risk Factors and Incidence Estimation.** *Radiology* 2007, **243**:148–157.
58. Utsunomiya D, Miyazaki M, Nomitsu Y, Komeda Y, Okigawa T, Urata J, Yamashita Y: **Clinical Role of Non-Contrast Magnetic Resonance Angiography for Evaluation of Renal Artery Stenosis.** *Circ J* 2008, **72**:1627–1630.
59. Leung D, Hagspiel K, Angle J, Spinosa D, Matsumoto A, Butty S: **MR angiography of the renal arteries.** *Radiologic Clinics of North America* 2002, **40**:847–865.
60. Kijowski R, Lu A, Block W, Grist T: **Evaluation of the articular cartilage of the knee joint with vastly undersampled isotropic projection reconstruction steady-state free precession imaging.** *J. Magn. Reson. Imaging* 2006, **24**:168–175.
61. Vasanawala SS, Pauly JM, Nishimura DG: **Linear combination steady-state free precession MRI.** *Magn Reson Med* 2000, **43**:82–90.
62. Moran CJ, Kelcz F, Jung Y, Brodsky EK, Fain SB, Block WF: **Pilot study of improved lesion characterization in breast MRI using a 3D radial balanced SSFP technique with isotropic resolution and efficient fat-water separation.** *J. Magn. Reson. Imaging* 2009, **30**:135–144.

63. Kijowski R, Blankenbaker DG, Klaers JL, Shinki K, De Smet AA, F BW: **Vastly Undersampled Isotropic Projection Steady-State Free Precession Imaging of the Knee: Diagnostic Performance Compared with Conventional MR1.** *Radiology* 2009, **251**:185–194.
64. Braendli M, Bongartz G: **Combining Two Single-Shot Imaging Techniques with Slice-Selective and Non-Slice-Selective Inversion Recovery Pulses: New Strategy for Native MR Angiography Based on the Long T1 Relaxation Time and Inflow Properties of Blood.** *American Journal of Roentgenology* 2003, **180**:725.
65. King KF, Angelos L: **SENSE with Partial Fourier Homodyne Reconstruction.** In *Proceedings of the 8th Annual Meeting of ISMRM.* Denver, CO: 2000:153.
66. Johnson K, Lum D, Francois C, Reeder S, Busse R, Grist T, Wieben O: **Non-Contrast Enhanced Renal MR Angiography with PC VIPR.** In *Proceedings of the 16th Annual Meeting of ISMRM.* Toronto, ON, Canada: 2008:733.
67. Ghosh S, Majumdar S: **Application of spectro-spatial pulses for contrast in cartilage imaging.** In *Proceedings of the 9th Annual Meeting of ISMRM.* Glasgow, Scotland: 2001:916.
68. Woolson RF: *Wilcoxon Signed-Rank Test.* *Wiley Encyclopedia of Clinical Trials.* Hoboken, NJ, USA: John Wiley & Sons, Inc; 2007:1–3.
69. Glover GH, Pauly JM: **Projection Reconstruction Techniques for Reduction of Motion Effects in MRI.** *Magn Reson Med* 1992, **28**:275–289.
70. Baskaran V, Pereles FS, Nemcek AA, Carr JC, Miller FH, Ly J, Krupinski E, Finn JP: **Gadolinium-Enhanced 3D MR Angiography of Renal Artery Stenosis: A Pilot Comparison of Maximum Intensity Projection, Multiplanar Reformatting, and 3D Volume-Rendering Postprocessing Algorithms.** *Academic Radiology* 2002, **9**:50–59.
71. Bahirwani R, Reddy KR: **Review article: the evaluation of solitary liver masses.** *Aliment. Pharmacol. Ther.* 2008, **28**:953–965.
72. Namasivayam S, Martin DR, Saini S: **Imaging of liver metastases: MRI.** *Cancer Imaging* 2007, **7**:2–9.
73. Robinson KA, Middleton WD, Al-Sukaiti R, Teefey SA, Dahiya N: **Doppler sonography of portal hypertension.** *Ultrasound Q* 2009, **25**:3–13.
74. Applegate GR, Thaete FL, Meyers SP, Davis PL, Talagala SL, Recht M, Wozney P, Kanal E: **Blood flow in the portal vein: velocity quantitation with phase-contrast MR angiography.** *Radiology* 1993, **187**:253–256.
75. Hoskins PR: **Measurement of arterial blood flow by Doppler ultrasound.** *Clin Phys Physiol Meas* 1990, **11**:1–26.

76. Weickert U, Buttman A, Jakobs R, Schilling D, Eickhoff A, Riemann JF: **Diagnosis of liver cirrhosis: a comparison of modified ultrasound and laparoscopy in 100 consecutive patients.** *J. Clin. Gastroenterol.* 2005, **39**:529–532.
77. Miles KA, Hayball MP, Dixon AK: **Functional images of hepatic perfusion obtained with dynamic CT.** *Radiology* 1993, **188**:405–411.
78. Van Beers BE, Leconte I, Materne R, Smith AM, Jamart J, Horsmans Y: **Hepatic perfusion parameters in chronic liver disease: dynamic CT measurements correlated with disease severity.** *AJR Am J Roentgenol* 2001, **176**:667–673.
79. Miyazaki S, Murase K, Yoshikawa T, Morimoto S, Ohno Y, Sugimura K: **A quantitative method for estimating hepatic blood flow using a dual-input single-compartment model.** *Br J Radiol* 2008, **81**:790–800.
80. Materne R, Van Beers BE, Smith AM, Leconte I, Jamart J, Dehoux JP, Keyeux A, Horsmans Y: **Non-invasive quantification of liver perfusion with dynamic computed tomography and a dual-input one-compartmental model.** *Clin. Sci.* 2000, **99**:517–525.
81. Nakashige A, Horiguchi J, Tamura A, Asahara T, Shimamoto F, Ito K: **Quantitative measurement of hepatic portal perfusion by multidetector row CT with compensation for respiratory misregistration.** *Br J Radiol* 2004, **77**:728–734.
82. Bader TR, Herneth AM, Blaicher W, Steininger R, Mühlbacher F, Lechner G, Grabenwöger F: **Hepatic perfusion after liver transplantation: noninvasive measurement with dynamic single-section CT.** *Radiology* 1998, **209**:129–134.
83. Blomley MJ, Coulden R, Dawson P, Korman M, Donlan P, Bufkin C, Lipton MJ: **Liver perfusion studied with ultrafast CT.** *Journal of Computer Assisted Tomography* 1995, **19**:424–433.
84. Meier P, Zierler KL: **On the theory of the indicator-dilution method for measurement of blood flow and volume.** *J Appl Physiol* 1954, **6**:731–744.
85. Thng CH, Koh TS, Collins DJ, Koh DM: **Perfusion magnetic resonance imaging of the liver.** *World J. Gastroenterol.* 2010, **16**:1598–1609.
86. Cao Y, Alspaugh J, Shen Z, Balter JM, Lawrence TS, Haken Ten RK: **A practical approach for quantitative estimates of voxel-by-voxel liver perfusion using DCE imaging and a compartmental model.** *Med Phys* 2006, **33**:3057–3062.
87. Materne R, Smith AM, Peeters F, Dehoux JP, Keyeux A, Horsmans Y, Van Beers BE: **Assessment of hepatic perfusion parameters with dynamic MRI.** *Magn Reson Med* 2001, **47**:135–142.
88. Cuenod CA, Leconte I, Siauve N, Frouin F, Dromain C, Clément O, Frija G: **Deconvolution technique for measuring tissue perfusion by dynamic CT:**

application to normal and metastatic liver. *Academic Radiology* 2002, **9 Suppl 1**:S205–11.

89. Axel L: **Tissue mean transit time from dynamic computed tomography by a simple deconvolution technique.** *Invest Radiol* 1983, **18**:94–99.

90. Baxter S, Wang ZJ, Joe BN, Qayyum A, Taouli B, Yeh BM: **Timing bolus dynamic contrast-enhanced (DCE) MRI assessment of hepatic perfusion: Initial experience.** *J. Magn. Reson. Imaging* 2009, **29**:1317–1322.

91. Hagiwara M, Rusinek H, Lee VS, Losada M, Bannan MA, Krinsky GA, Taouli B: **Advanced Liver Fibrosis: Diagnosis with 3D Whole-Liver Perfusion MR Imaging-- Initial Experience.** *Radiology* 2008, **246**:926–934.

92. Gibson JG, Seligman AM: **The distribution of red cells and plasma in large and minute vessels of the normal dog, determined by radioactive isotopes of iron and iodine.** *J. Clin. Invest.* 1946, **25**:848–857.

93. Ostergaard L, Weisskoff RM, Chesler DA, Gyldensted C, Rosen BR: **High resolution measurement of cerebral blood flow using intravascular tracer bolus passages. Part I: Mathematical approach and statistical analysis.** *Magn Reson Med* 1996, **36**:715–725.

94. Thompson HK, Starmer CF, Whalen RE, McIntosh HD: **Indicator transit time considered as a gamma variate.** *Circ. Res.* 1964, **14**:502–515.

95. Carr DH, Graif M, Niendorf HP, Brown J, Steiner RE, Blumgart LH, Young IR: **Gadolinium-DTPA in the assessment of liver tumours by magnetic resonance imaging.** *Clinical Radiology* 1986, **37**:347–353.

96. Reimer P, Rummeny EJ, Daldrup HE, Hesse T, Balzer T, Tombach B, Peters PE: **Enhancement characteristics of liver metastases, hepatocellular carcinomas, and hemangiomas with Gd-EOB-DTPA: preliminary results with dynamic MR imaging.** *Eur Radiol* 1997, **7**:275–280.

97. Abdullah SS, Pialat JB, Wiart M, Duboeuf F, Mabrut J-Y, Bancel B, Rode A, Ducerf C, Baulieux J, Berthezene Y: **Characterization of hepatocellular carcinoma and colorectal liver metastasis by means of perfusion MRI.** *J. Magn. Reson. Imaging* 2008, **28**:390–395.

98. Peeters F, Annet L, Hermoye L, Van Beers BE: **Inflow correction of hepatic perfusion measurements using T1-weighted, fast gradient-echo, contrast-enhanced MRI.** *Magn Reson Med* 2004, **51**:710–717.

99. Wang K, Busse RF, Holmes JH, J BP, Brittain JH, Francois CJ, Reeder SB, Du J, Korosec FR: **Interleaved variable density sampling with a constrained parallel imaging reconstruction for dynamic contrast-enhanced MR angiography.** *Magn Reson Med* 2011, **66**:428–436.

100. Rettmann D, Saranathan M, Glockner J: **Differential Subsampling with Cartesian Ordering (DISCO): a novel k-space ordering scheme for dynamic MRI.** In *Proceedings of the 18th Annual Meeting of ISMRM*. Stockholm, Sweden: 2010:3044.
101. Glockner JF, Hu HH, Stanley DW, Angelos L, King K: **Parallel MR imaging: a user's guide.** *Radiographics* 2005, **25**:1279–1297.
102. Wang H, Cao Y: **Correction of arterial input function in dynamic contrast-enhanced MRI of the liver.** *J. Magn. Reson. Imaging* 2012, **36**:411–421.
103. Shapiro MG, Atanasijevic T, Faas H, Westmeyer GG, Jasanoff A: **Dynamic imaging with MRI contrast agents: quantitative considerations.** *Magnetic Resonance Imaging* 2006, **24**:449–462.
104. Franklin KM, Dale BM, Merkle EM: **Improvement in B1-inhomogeneity artifacts in the abdomen at 3T MR imaging using a radiofrequency cushion.** *J. Magn. Reson. Imaging* 2008, **27**:1443–1447.
105. Cron GO, Santyr G, Kelcz F: **Accurate and rapid quantitative dynamic contrast-enhanced breast MR imaging using spoiled gradient-recalled echoes and bookend T(1) measurements.** *Magn Reson Med* 1999, **42**:746–753.
106. Bokacheva L, Rusinek H, Chen Q, Oesingmann N, Prince C, Kaur M, Kramer E, Lee VS: **Quantitative determination of Gd-DTPA concentration in T1-weighted MR renography studies.** *Magn Reson Med* 2007, **57**:1012–1018.
107. Do RKG, Rusinek H, Taouli B: **Dynamic Contrast-Enhanced MR Imaging of the Liver: Current Status and Future Directions.** *Magnetic Resonance Imaging Clinics of North America* 2009, **17**:339–349.
108. Rohlfing T, Maurer CR, O'Dell WG, Zhong J: **Modeling liver motion and deformation during the respiratory cycle using intensity-based nonrigid registration of gated MR images.** *Med Phys* 2004, **31**:427.
109. Vasanawala SS, Iwadate Y, Church DG, Herfkens RJ, Brau AC: **Navigated abdominal T1-W MRI permits free-breathing image acquisition with less motion artifact.** *Pediatr Radiol* 2010, **40**:340–344.
110. Lin W, Guo J, Rosen MA, Song HK: **Respiratory motion-compensated radial dynamic contrast-enhanced (DCE)-MRI of chest and abdominal lesions.** *Magn Reson Med* 2008, **60**:1135–1146.
111. Melbourne A, Atkinson D, White MJ, Collins D, Leach M, Hawkes D: **Registration of dynamic contrast-enhanced MRI using a progressive principal component registration (PPCR).** *Phys Med Biol* 2007, **52**:5147–5156.
112. Barger AV, Block WF, Toropov Y, Grist TM, Mistretta CA: **Time-resolved contrast-enhanced imaging with isotropic resolution and broad coverage using**

an undersampled 3D projection trajectory. *Magn Reson Med* 2002, **48**:297–305.

113. Brodsky EK, Isaacs DL, Block WF, Reeder SB: **Multiple-phase CE-MRA of the liver using time-resolved 3DPR.** In *Proceedings of the 16th Annual Meeting of ISMRM*. Toronto, Ontario, Canada: 2008.

114. Duyn JH, Yang Y, Frank JA, van der Veen JW: **Simple correction method for k-space trajectory deviations in MRI.** *J. Magn. Reson.* 1998, **132**:150–153.

115. Johnson KM, Brodsky E, Samsonov A, F BW, Wieben O, Reeder S: **Rapid Angiography and Perfusion with Multi-Echo 3D Radials and an Echo Weighted Constrained Reconstruction.** In *MR Angio Club*. Seoul, South Korea: 2010.

116. Richter S, Mücke I, Menger MD, Vollmar B: **Impact of intrinsic blood flow regulation in cirrhosis: maintenance of hepatic arterial buffer response.** *Am J Physiol Gastrointest Liver Physiol* 2000, **279**:G454–G462.

117. Abou-Alfa GK, Schwartz L, Ricci S, Amadori D, Santoro A, Figer A, De Greve J, Douillard J-Y, Lathia C, Schwartz B, Taylor I, Moscovici M, Saltz LB: **Phase II Study of Sorafenib in Patients With Advanced Hepatocellular Carcinoma.** *Journal of Clinical Oncology* 2006, **24**:4293-300.

118. van den Bos IC, Hussain SM, Dwarkasing RS, Hop WCJ, Zondervan PE, de Man RA, IJzermans JNM, Walker CW, Krestin GP: **MR imaging of hepatocellular carcinoma: Relationship between lesion size and imaging findings, including signal intensity and dynamic enhancement patterns.** *J. Magn. Reson. Imaging* 2007, **26**:1548–1555.

119. Collins DJ, Padhani AR: **Dynamic magnetic resonance imaging of tumor perfusion.** *IEEE Eng. Med. Biol. Mag.* 2004, **23**:65–83.

120. Saranathan M, Rettmann D, Brau AS, Hargreaves BA, Vasanawala SS: **Ultra high spatio-temporal resolution liver imaging using a new view ordering scheme and a 2-point Dixon acquisition.** In *Proceedings of the 19th Annual Meeting of ISMRM*. Montreal, Quebec, Canada: 2011.

121. Pandharipande PV, Krinsky GA, Rusinek H, Lee VS: **Perfusion Imaging of the Liver: Current Challenges and Future Goals.** *Radiology* 2005, **234**:661–673.

122. Xu B, Spincemille P, Chen G, Agrawal M, Nguyen TD, Prince MR, Wang Y: **Fast 3D contrast enhanced MRI of the liver using temporal resolution acceleration with constrained evolution reconstruction.** *Magn Reson Med* 2012.

123. Brodsky EK, Bultman E, Schelman WR, Johnson KM, Horng D, Block WF, Reeder SB: **High Spatial and High Temporal Resolution Dynamic Contrast-Enhanced Perfusion Imaging of the Liver with Time-Resolved 3D-Radial MRI.** *Awaiting resubmission to MRM with minor revisions.*

124. Horng D, Brodsky EK, Reeder S: **Validation of DC Self-Navigation for Breath-hold Period Identification in Contrast-Enhanced 3D Radial Liver Perfusion Imaging.** *Proceedings of the 19th Annual Meeting of ISMRM 2011.*
125. Bultman E, Horng D, Brodsky EK, Johnson KM, F BW, Reeder S: **Simple Motion Correction for Hepatic DCE-MRI: Registration of Sequential Breath Holds in 3D Radial Time-Resolved Scans.** In *Proceedings of the 20th Annual Meeting of ISMRM.* Melbourne, Australia: 2012.
126. Yoo TS, Ackerman MJ, Lorensen WE, Schroeder W, Chalana V, Aylward S, Metaxas D, Whitaker R: **Engineering and algorithm design for an image processing Api: a technical report on ITK--the Insight Toolkit.** *Stud Health Technol Inform 2002, 85:586–592.*
127. Akaike H: **A new look at the statistical model identification.** *Automatic Control 1974 19:716-23.*
128. Lassau N, Koscielny S, Chami L, Chebil M, Benatsou B, Roche A, Ducreux M, Malka D, Boige V: **Advanced hepatocellular carcinoma: early evaluation of response to bevacizumab therapy at dynamic contrast-enhanced US with quantification--preliminary results.** *Radiology 2011, 258:291–300.*
129. Welch BL: **The Generalization of Student's Problem when Several Different Population Variances are Involved.** *Biometrika 1947, 34:28–35.*
130. Gülberg V, Haag K, Rössle M, Gerbes AL: **Hepatic arterial buffer response in patients with advanced cirrhosis.** *Hepatology 2002, 35:630–634.*
131. Tajima T, Honda H, Taguchi K, Asayama Y, Kuroiwa T, Yoshimitsu K, Irie H, Aibe H, Shimada M, Masuda K: **Sequential hemodynamic change in hepatocellular carcinoma and dysplastic nodules: CT angiography and pathologic correlation.** *Am J Roentgenol 2002, 178:885–897.*
132. Heye T, Yang S-R, Bock M, Brost S, Weigand K, Longerich T, Kauczor H-U, Hosch W: **MR relaxometry of the liver: significant elevation of T1 relaxation time in patients with liver cirrhosis.** *Eur Radiol 2012, 22:1224–1232.*
133. Cron GO, Kelcz F, Santyr GE: **Improvement in breast lesion characterization with dynamic contrast-enhanced MRI using pharmacokinetic modeling and bookend T1 measurements.** *Magnetic Resonance in Medicine 2004.*
134. Judd RM, Reeder SB, Atalar E, McVeigh ER, Zerhouni EA: **A magnetization-driven gradient echo pulse sequence for the study of myocardial perfusion.** *Magn Reson Med 1995, 34:276–282.*
135. Dharmakumar R, Hong J, Brittain JH, Plewes DB, Wright GA: **Oxygen-sensitive contrast in blood for steady-state free precession imaging.** *Magn Reson Med 2005, 53:574–583.*

136. Brodsky EK, Reeder S, Yu H, F BW: **Water-Fat Separation at 3T with IDEAL and 3DPR**. In *Proceedings of the 14th Annual Meeting of ISMRM*. Seattle, Washington, USA: 2006.

137. Bultman E, Hines CDG, Block WF, Reeder SB: **MR validation and quantification of TACE treatment through direct visualization of Ethiodol with Chemical Shift Based Water-Fat Imaging**. In *Proceedings of the 17th Annual Meeting of ISMRM*. Honolulu, HI, USA: 2009.

138. Bultman E, Klaers J, Francois CJ, Schiebler ML, Reeder SB, Block WF: **Non Contrast Enhanced (NCE)-MRA of the Renal Transplant Vessels: A comparison between IFIR and VIPR-SSFP**. In *Proceedings of the 19th Annual Meeting of ISMRM*. Montreal, Quebec, Canada: 2011.